Influenza A infections in the Host: Modeling and Control Approaches

A dissertation submitted for the degree of
Doctor of Philosophy

At the Faculty of Biological Sciences (FB 15) of the
Johann Wolfgang Goethe-University in Frankfurt am Main

submitted by
Gustavo Hernandez Mejia
from Guadalajara (Mexico)

Frankfurt am Main, 2023

Vom Fachbereich Biowissenschaften (FB 15) der
Johann Wolfgang Goethe-Universität als Dissertation angenommen

Dekan: Prof. Dr. Sven Klimpel
Gutachter: Prof. Dr. Franziska Matthäus
Betreuer: Dr. Esteban Abelardo Hernandez Vargas

Datum der Disputation: 18.12.2023

This thesis was conducted at the
Frankfurt Institute for Advanced Studies (FIAS),
Frankfurt am Main, Federal Republic of Germany.

Contents

Abstract

Influenza is a contagious respiratory disease caused by influenza A and influenza B viruses. The World Health Organisation (WHO) reports that annual influenza epidemics result in approximately 1 billion infections, 3 to 5 million severe cases, and 300 to 650 thousand deaths. Understanding hidden mechanisms that lead to optimal vaccine efficacy and improvement antiviral treatment strategies remain continuous and central tasks. First, regarding the immune response to vaccines and natural infections, the antibody response echoes the dynamics of diverse immune elements such as B-cells, and plasma cells. Also, responses reflect the processes for B-cells to gain and adapt affinity for the virus. Antibodies (Abs) that respond to the virus surface proteins, particularly to the hemagglutinin (HA), have been identified to protect against infection. The Abs responses binding to HA can be broadly protective as this protein is considerably accessible on the virion. When following sequential infections with similar influenza strains, i.e. two infections with different strains of a subtype, an enhanced breadth and magnitude of Abs response is developed, mainly after the second infection. The effect of being effective to new strains is called Abs cross-reaction.

On the other hand, as for antiviral treatment, the WHO currently approves the use of neuraminidase inhibitors (NIs) such as zanamivir and oseltamivir. Diverse research areas such as system biology, learning-based methods, control theory, and systems pharmacology have guided the development of modern treatment schemes. To do so, mathematical models are used to describe a wide range of phenomena such as viral pathogenesis, immune responses, and the drug's dynamics in the body. Drug dynamics are usually expressed in two phases, pharmacokinetics (PK) and pharmacodynamics (PD) - the PK/PD approach. These schemes leverage pre-clinical and clinical data through modeling and simulation of infection and drug effects at diverse levels. Under such a framework, control-based scheduling systems seek to tailor optimal antiviral treatment for infectious diseases. Thus, influenza treatment can be theoretically studied as a control-based optimization duty (about systems stability, bounded inputs, and optimality). Finally, towards real-world implementation, learning-based methods such as neural networks (NNs) can guide solving issues on the control-based performance. Using NNs as identifiers provide a setting to deal with infrequent measures and uncertain parameters for the control systems.

This thesis theoretically explores central mechanisms in influenza infection via modeling and control approaches. In the first project, we explore how and to what extent antibody-antigen affinity flexibility could guide the Abs cross-reaction in two sequential infections using a hypothetical family of antigens. The set of antigens generally represent strains of influenza, such as those of a subtype. Each antigen is composed of a variable and a conserved area, generically representing the structures of the HA, head, and stalk, respectively. We test diverse scenarios of affinity thresholds in the conserved and variable areas of the antigens. For each scenario, we analyse the characteristics that might lead to enhanced breadth and magnitude of Abs responses. The Abs response reaches a high magnitude when using equivalent affinity thresholds in the conserved and variable areas during the first infection. However, improved cross-reaction is developed when slightly increasing the affinity threshold of the variable area for the second infection. Key mutations via affinity maturation is a feature that, together with affinity flexibility between infections, guides Abs cross-reaction in the model outcome. These results could correlate with observations in experimental and theoretical settings. Such studies point out that broad responses might be dependent on reaching specific mutations for getting affinity to a newly presented antigen while broadly reaching related antigens. The general platform may serve as a proof-of-concept for exploring fundamental mechanisms that favor the Abs cross-reaction.

In a second project, theoretical schemes are developed to combine impulsive and inverse optimal control strategies to address antiviral treatment scheduling. We present results regarding stability, passivity, bounded inputs, and optimality using impulsive action. The study is founded on mathematical models of the influenza virus (target-cell limited model) adjusted to data from clinical trials. In these studies, participants were experimentally infected with influenza H1N1 and treated with NIs. Results show that control-based strategies could tailor dosage and reduce the amount of medication by up to 44%. Also, control-based treatment reaches the efficacy (98%) of the current treatment recommendations by the WHO. Monte Carlo simulations (MCS) disclose the robustness of the proposed control-based techniques. Using MCS, we also explore the applicability to the individualized treatment of infectious diseases through virtual clinical trials. Furthermore, bounded control strategies are applied directly in drug dose estimation accounting for overdose prevention. Finally, due to the limitations of the available technology intended for clinical practice, we emphasize the necessity of developing system identifiers and observers for real-world applications.

In the third project, the problem of data scarcity and infrequent measures in the real world is handled by means of learning-based methods. System identification is derived using a Recurrent High Order Neural Network (RHONN) trained with the Extended Kalman filter (EKF). Lessons learned from impulsive control frameworks are taken to develop a neural inverse optimal impulsive control –neurocontrol. This control policy is constructed by combining the inverse optimal control and the RHONN system. The control action is applied to both the RHONN and the mathematical model of influenza. The host model considers the influenza virus and CD8+ T cells dynamics. The drug dynamics are integrated via the PK/PD phases of NIs. The neurocontrol is thus applied to dose tailoring in the treatment of influenza. Neurocontrol efficacy is tested for early (one day post-infection) and late (2 to 3 days post-infection) treatment initiation. The neurocontrol reaches an efficacy of up to 95% while saving almost 40% of the total drug in the early treatment. Robustness is tested via virtual clinical trials using MCS.

Lastly, taking all together, the schemes developed in this thesis for modeling the Abs cross-reaction and control-based treatment tailoring can be extended and adapted to explore similar phenomena in different respiratory pathogens, such as SARS-CoV-2.

Zusammenfassung

Influenza ist eine ansteckende Atemwegserkrankung, die durch Influenza-A- und Influenza-B-Viren verursacht wird. Die Weltgesundheitsorganisation (WHO) berichtet, dass jährliche Grippeepidemien zu etwa 1 Milliarde Infektionen, 3 bis 5 Millionen schweren Fällen und 300 bis 650 Tausend Todesfällen führen [1]. Impfungen gehören zu den besten verfügbaren Gegenmaßnahmen gegen die Infektion. Ihre Wirksamkeit ist jedoch nach wie vor begrenzt. Die durch Influenzaimpfstoffe induzierte Antikörperreaktion (Abs) ist im Vergleich zur Abs-Antwort bei einer natürlichen Infektion schmaler und kurzlebiger [2, 3]. Neben den Impfstoffen spielen antivirale Medikamente eine zentrale Rolle bei der Vorbeugung und Behandlung von Influenza-Infektionen und -Krankheiten. Virostatika werden vor allem zur Behandlung von schwer erkrankten Patienten eingesetzt. Sie werden auch zur Verhütung von Infektionen bei Personen eingesetzt, die einer Infektion ausgesetzt waren [4]. Ihr Einsatz und ihre Verfügbarkeit sind jedoch nach wie vor eingeschränkt [1]. Vor diesem Hintergrund bleibt das Verständnis von Mechanismen, die zu einer höheren Impfstoffwirksamkeit über breite Abs-Antworten und optimale antivirale Behandlungsstrategien führen, eine kontinuierliche und zentrale Aufgabe. In dieser Doktorarbeit werden solche Systeme bei Influenza-Infektionen mit Hilfe von Modellierungs- und Kontrollansätzen theoretisch untersucht.

Die Abs-Antwort spiegelt die Dynamik verschiedener Immunelemente wie B-Zellen und Plasmazellen wider [2, 3]. Die Abs-Antworten spiegeln auch die Prozesse wider, denen B-Zellen folgen, um die Affinität für das Virus zu gewinnen und anzupassen. Dieser Prozess wird als Affinitätsreifung bezeichnet. Der strukturelle Teil des Virus spielt ebenfalls eine zentrale Rolle bei der Entwicklung der Affinität. Die Abs reagieren auf die Virusoberflächenproteine, insbesondere auf das Hämagglutinin (HA). Es wurde festgestellt, dass diese Art der Reaktion vor einer Infektion schützt [2]. Diese Reaktionen können weitgehend schützend sein, da dieses Protein auf der Virionenoberfläche gut zugänglich ist. Nach aufeinanderfolgenden Infektionen mit ähnlichen Influenzastämmen, d. h. nach zwei Infektionen mit verschiedenen Stämmen eines Subtyps, wird eine breitere und stärkere Abs-Antwort entwickelt. Dies geschieht vor allem nach der zweiten Infektion [5]. Der Effekt, dass Abs gegen verschiedene Stämme wirksam sind, wird als Abs-Kreuzreaktion bezeichnet. Die Breite und das Ausmaß der Abs-Kreuzreaktion wurden bisher mit Hilfe von Modellierungsschemata erforscht, meist für einzelne Infektionsschemata. Es gibt Arbeiten, die sich mit den Auswirkungen antigener Unterschiede auf breite Reaktionen befassen [6]. Die Antigene repräsentieren beispielsweise die Eigenschaften verschiedener Grippestämme. Auch die Modellierungseinstellungen für die B-Zell-Antigen-Bindungsaffinität und die Affinitätsreifung wurden umfassend bewertet [7, 8]. Die Mechanismen, die zu einer erhöhten Breite und Stärke von Abs bei sequenziellen Infektionen führen, sind jedoch noch unerforscht. In dieser

Arbeit modellieren wir Szenarien der B-Zell-Antigen-Affinitätsflexibilität, um Bedingungen zu identifizieren, die die Kreuzreaktion von Abs bei sequenziellen Infektionen begünstigen.

Was die antivirale Therapie betrifft, so genehmigt die WHO derzeit die Verwendung von Neuraminidase-Inhibitoren (NIs) wie Zanamivir und Oseltamivir [1]. Verschiedene Forschungsbereiche wie Systembiologie, lernbasierte Methoden, Kontrolltheorie und Pharmakologie haben die Entwicklung moderner Behandlungsverfahren vorangetrieben. Dabei werden mathematische Modelle verwendet, um eine Vielzahl von Phänomenen wie die virale Pathogenese, Immunreaktionen und die Dynamik des Medikaments im Körper zu beschreiben. Die Dynamik von Arzneimitteln wird in der Regel in zwei Phasen ausgedrückt, der Pharmakokinetik (PK) und der Pharmakodynamik (PD) - der PK/PD-Ansatz [9]. In einem solchen Rahmen können kontrollbasierte Planungssysteme verwendet werden, um eine optimale Behandlung für Infektionskrankheiten zu entwickeln. In diesem Sinne kann die Grippe-Behandlung theoretisch als eine kontrollbasierte Optimierungsaufgabe (in Bezug auf Systemstabilität, begrenzte Eingaben und Optimalität) untersucht werden. Wir integrieren mathematische Modelle auf der Wirtsebene, um einen Rahmen für die Dynamik von Viren (und anderen Immunelementen) zu schaffen [10]. Die PK/PD leitet das Verhalten des Medikaments. Wir nutzen frühere Studien zur inversen optimalen und impulsiven Kontrolle. Für die kontrollbasierte Technik wird die inverse optimale Kontrolle angepasst, um die Dosismenge zu berechnen [11]. Die impulsive Steuerung ist eine Technik zur Darstellung der Dosiseinnahmezeit [12, 13]. Gemeinsam passt die kontrollbasierte Behandlung die Dosis an die Entwicklung des Wirtsmodells an. Schließlich können lernbasierte Methoden wie neuronale Netze (NNs) bei der Lösung von Problemen im Zusammenhang mit der steuerungsbasierten Leistung in der Praxis helfen [14]. Wir führen NNs als Identifikatoren ein, um mit seltenen Maßnahmen und unsicheren Parametern für die Kontrollsysteme umzugehen. Die Hauptprojekte dieser Doktorarbeit werden in drei Kapiteln (Kapiteln 3 - 5) entwickelt.

Kapitel 3 stellt ein theoretisches Schema für die Abs-Kreuzreaktion bei sequentiellen Infektionen vor. Die Hauptmotivation ist die Breite und das Ausmaß der Abs-Antwort, die in Experimenten mit Tiermodellen und natürlichen Influenza-Infektionen beim Menschen beobachtet wurde [5]. Es ist bekannt, dass die Abs-Antwort eine große Anzahl von Ereignissen widerspiegelt. Antikörper erlangen eine hohe Affinität durch somatische Hypermutation in B-Zellen über Affinitätsreifung [15]. Antigen-induzierte B-Zell-Aktivierung und -Differenzierung in sekundären lymphatischen Geweben führen zur Keimzentrumsreaktion (GC) [16]. In GCs werden B-Zellen auf der Grundlage der Fähigkeit ihrer mutierten Abs, Antigene zu binden, selektiert. Diese Selektion führt zu einer erhöhten Fitness der Abs-Population [17, 18, 19].

In dieser Modellierungsstudie beziehen wir bereits erforschte Grundmechanismen für Abs-Reaktionen ein. Wir integrieren Aspekte der Form-Raum-Modellierung für Influenza [20, 21]. In Anlehnung an das Shape-Space-Schema berücksichtigen wir den antigenen Abstand zwischen den Antigenen der Infektion. Antigene werden durch Zeichenketten dargestellt, die sich am binären Alphabet orientieren. Der antigene Abstand wird durch die Hamming-Distanz bestimmt [6, 22]. Antigene weisen einen variablen und einen konservierten Bereich auf. Diese stehen allgemein für die strukturellen HA-Merkmale, den Kopf und den Stiel. Darüber hinaus integrieren wir Schemata für die B-Zell-Antigen-Bindungsaffinität, die Fitness von B-Zellen und ein dynamisches Affinitätskonzept. Für die Bindungsaffinität integrieren wir das Konzept des längsten gemeinsamen Teilstrings zwischen den konservierten und variablen

Teilen der Bindungsbereiche [7]. Im Modell sind Mutationen vorgesehen, die Schlüsselmutationen in den Teilstrings erlauben [8]. Bei den derzeitigen Ansätzen wird die Möglichkeit, dass sich die dynamische Bindungsaffinität auf die Wirksamkeit von Abs-Reaktionen auswirken kann, kaum untersucht. Eine strenge Affinitätsregulierung wird schnell zu einer durchschnittlichen Affinitätspopulation führen, was auf Kosten der Vielfalt geht. Andererseits wird eine lockere Regulierung zu einer hohen Diversität führen, aber die Affinität wird langsam ansteigen [17]. Bei sequentiellen Infektionen können sich jedoch hochaffine Abs nach der zweiten Infektion breit entwickeln [5]. Wir untersuchen die Flexibilität der Affinitätsschwellen zwischen sequenziellen Infektionen. Ziel ist es, Unterschiede zwischen Szenarien mit fester und variabler Affinität zu identifizieren, die eine angemessene Darstellung der Breite und des Ausmaßes der Abs-Reaktion ermöglichen.

Es wurden verschiedene Schwellenwertkombinationen für die konservierten und variablen Bereiche getestet. Wenn Änderungen an den Affinitätsschwellenwerten vorgenommen wurden, wurden diese von der ersten auf die zweite Infektion angewendet. Dies geschah vor allem, um die größere Breite und das größere Ausmaß zu erforschen, die normalerweise nach einer zweiten Infektion auftreten. Die Abs-Kreuzreaktion wurde für sechs verschiedene Antigene getestet. Wir entwickelten vier Explorationsfälle mit jeweils 3 bis 5 Szenarien von Affinitätsschwellenwerten. Es wurde festgestellt, dass eine Änderung der Affinitätsschwelle im variablen Bereich die Abs-Kreuzreaktionsphänomene bei sequenziellen Infektionen darstellen könnte. Außerdem wird ein fester Schwellenwert im konservierten Bereich für beide Infektionen beibehalten. Wir haben außerdem die Auswirkungen der Affinitätsflexibilität auf verschiedene antigene Abstände getestet. Der antigene Unterschied spielt sicherlich eine wichtige Rolle bei den breiten Reaktionen bei einer ersten Infektion. Bei der zweiten Infektion ermöglicht die Affinitätsflexibilität breitere Reaktionen. Außerdem testen wir die Auswirkung der Zeit zwischen den Infektionen (10 Tage, 20 Tage, 42 Tage, und 84 Tage) auf die Abs-Kreuzreaktion. Breite Reaktionen werden für beide Infektionen mit bis zu 42 Tagen zwischen den Infektionen erreicht. Schließlich testen wir die Auswirkungen der Reihenfolge der Infektion (A + B oder B + A) auf die Abs-Kreuzreaktion. Wir glauben jedoch, dass dieses Szenario-Experiment weitere evolutionäre Mechanismen entwickeln muss [23].

Änderungen der Affinität können mit Mutationen zusammenhängen, die schwer zu erreichen sind, wenn das zweite Antigen präsentiert wird. Einige dieser Schlüsselmutationen könnten sich vorteilhaft auf die Breite auswirken, da sie die Kontakte mit dem bereits bekannten Teil des Antigens, dem konservierten Bereich, verbessern [24]. Im Modell ist ein solcher Mechanismus nur durch Mutationen in der Mitte der Kette eines jeden Antigenbereichs gegeben. Diese Art von einmaligem Umklappen eines binären Zeichens führt zu größeren Veränderungen der Affinität. Dies könnte mit Studien übereinstimmen, die darauf hindeuten, dass geringfügige Mutationen die Breite und Wirksamkeit erhöhen könnten, indem sie für eine größere Flexibilität bei der Antigenbindung sorgen [23, 24]. In diesem Kapitel wird die Notwendigkeit der Flexibilität der Affinitätsschwellen zwischen den Infektionen hervorgehoben, wenn man die Untersuchungen zusammen betrachtet. In diesem ersten Ansatz wurde die Einführung von Affinitätsänderungen auf eine eher willkürliche Art und Weise vorgenommen, indem bestimmte Szenarien von Schwellenwertänderungen verfolgt wurden. Die Modellierungsschemata in dieser Plattform sollten jedoch entwickelt werden, um evolutionäre Übergänge in der Affinität zu testen [23]. In dieser Richtung dient die Plattform als Proof-of-Concept, das auf verschiedene Merkmale wie die Aktivierungs- und

Überlebenssignale für B-Zellen erweitert werden kann. Das Modell sollte in der Lage sein, Phänomene der dunklen (für Recycling und Mutation) und hellen (für Selektion) Zonen in Keimzentren zu integrieren [16].

Kapitel 4 stellt theoretische Schemata von kontrollbasierten Behandlungssystemen zur optimalen Dosisanpassung vor. Wir verwenden das Fallbeispiel der Influenza-Behandlung. Die klinischen Ziele werden im Hinblick auf die Wirksamkeit der Behandlung untersucht [25]. Impulsive Steuerung und inverse optimale Steuerungsansätze werden kombiniert, um den Rahmen für die Dosisplanung zu entwickeln. Es wurden mathematische Modelle für Infektionskrankheiten entwickelt, die unterschiedlich detailliert sind. Einige Modelle versuchen, quantitative Einblicke in die Virusdynamik innerhalb des Wirtes zu geben, z. B. zur Quantifizierung des Influenzavirus-Infektionsgrades. Pioniermodelle beschreiben die Influenzadynamik in experimentell infizierten Mäusen [26]. Bei der Integration von Daten über Influenzainfektionen beim Menschen verwenden einige Systeme das zielzellenbegrenzte Modell [10]. Auf der anderen Seite gibt es Strategien, die sich auf die Immunantwort des Wirtes konzentrieren. In einigen Studien wird versucht, ein umfassendes Bild der Wirtsantwort zu erstellen [27, 28]. Spezifischere Ansätze untersuchen die Kontrolle der Influenzavirusinfektion durch CD8+ T-Zellen [29, 30, 31].

Wie bei pharmakologischen Schemata wird die Modellierung verwendet, um Quellen der Variabilität in der Dosis-Konzentrations-Wirkungs-Beziehung eines Arzneimittels zu ermitteln. Dies ist im Wesentlichen das Ziel der PK/PD-Schemata [32, 33]. PK steht für Kompartimente, die das Konzentrations-Zeit-Dynamik eines Arzneimittels darstellen. Dabei werden beispielsweise Faktoren wie die Halbwertszeit und die maximale Konzentration des Arzneimittels berücksichtigt. Im Falle der PD geben Werte wie EC_{50} in der Regel die Konzentration an, die 50% der maximalen Wirkung (Potenz) erzeugt [9]. Zusammengenommen steht das PK/PD-Schema für die Wirkung-Zeit-Relation eines Arzneimittels. Das PK/PD-Schema wird daher für die Erforschung therapeutischer Endpunkte verwendet [34].

Die Regelungstheorie ist ein Rahmen für die Steuerung eines dynamischen Systems, damit es sich in einer gewünschten stabilen Weise verhält. Dies geschieht durch die Berechnung einer Systemeingabe, die in der Regel einige Optimalitätskriterien erfüllt [35]. Eines der gebräuchlichsten Steuerungskonzepte ist die Regelungstechnik. Sie wird auch als Rückkopplungssteuerung bezeichnet und verwendet mathematische und rechnerische Elemente, um den Systemeingang in Richtung eines gewünschten Sollwerts zu regeln. Dies geschieht auf der Grundlage eines Rückkopplungssignals von der Regelstrecke [11]. Beispiele für dieses Verfahren sind einfache Systeme wie die Regelung der Wassertemperatur eines Heizkessels. Auch komplexe Systeme können einer Rückkopplungssteuerung folgen, wie die Tragflächen eines Flugzeugs oder der Blutzuckerspiegel eines Diabetikers mit Hilfe elektronischer Geräte. Rückkopplungsregelungssysteme bestehen klassischerweise aus vier Elementen: dem System; dem Rückkopplungssignal, das von einem Sensor stammen kann; dem Sollwert und der Steuerung. [11]. Im Allgemeinen ist das System im Fall dieser Studie der mit dem Influenzavirus infizierte Körper. Der Sollwert besteht darin, die Viruslast auf ein nicht nachweisbares Niveau zu bringen. Der Controller ist ein System, das die Medikamentendosis in Abhängigkeit von der viralen Dynamik berechnet. Sensoren melden die Viruslast sowie das Zell- und Immunverhalten. Derzeit muss die Technologie der Rückkopplungssensoren noch entwickelt werden. Mathematische Rahmenwerke können jedoch den Weg für die Darstellung solcher Kontrollmechanismen ebnen.

Wir integrieren Kenntnisse aus der Theorie der inversen optimalen Steuerung, der Passivität von Systemen und der Stabilität. Die impulsive Steuerung ist eine Strategie zur sofortigen Änderung des Zustandswertes eines Systems [12], dabei steht die impulsive Aktion für die Dosisaufnahmezeit. Die entsprechenden Grundlagen mit mathematischen Beweisen werden vorgestellt. Wir testen die vorgeschlagene kontrollbasierte Behandlung anhand von Daten von Patienten, die mit NIs, Zanamivir und Oseltamivir behandelt wurden. Wir vergleichen die Wirksamkeit und die Gesamtdosis der kontrollbasierten Behandlung mit den aktuellen Festdosisempfehlungen. Dabei orientieren wir uns an den Dosierungsrichtlinien der WHO. Die Behandlungsstrategien werden auf individueller und auf Bevölkerungsebene mittels Monte-Carlo-Simulationen (MCS) getestet. Bei der kontrollbasierten Behandlung wird die Dosis zu jedem Einnahmezeitpunkt auf der Grundlage der viralen Wirtsdynamik berechnet. Bei der Festdosisbehandlung wird für jede Einnahme eine bestimmte Medikamentenmenge angegeben, z. B. 100 mg im Falle von Oseltamivir. Beide Schemata werden für einen frühen (1 Tag nach der Infektion) und einen verzögerten (2 Tage nach der Infektion) Behandlungsbeginn getestet. Das kontrollbasierte Schema erreicht bei der Verwendung von Oseltamivir eine vergleichbare Wirksamkeit (98%) wie die WHO-Empfehlungen. Darüber hinaus ist die Gesamtmenge des Medikaments (Oseltamivir) bei der kontrollbasierten Behandlung um bis zu 44% reduziert. Die Prävention von Überdosierungen wird durch begrenzte Kontrollstrategien gewährleistet. Dieses Schema wird direkt in das Verfahren zur Dosisabschätzung mit automatischen Grenzwerten für die Dosiseingabe eingeführt. Schließlich analysieren wir die Grenzen der derzeitigen Technologieanwendung in der klinischen Praxis. Die am häufigsten verwendeten Quantifizierungsmethoden sind zum Beispiel die Titration mittels Plaque-Assay und der TCID_{50}-Schätzversuch. Beide Methoden sind jedoch zeitaufwändig, und es kann einige Tage dauern, bis die Ergebnisse vorliegen [36]. Daher betonen wir die Notwendigkeit der Entwicklung von Systemidentifikatoren (mit messbaren Zustandsvariablen) und Beobachtern für zukünftige Studien. Ein Beobachter ist ein System, das nicht messbare Zustandsvariablen aus bekannten Eingangs- und Ausgangsvariablen (messbaren Variablen) eines beobachteten Referenzsystems rekonstruiert. Die Zustandsgrößen sollten mit dem Referenzsystem vergleichbar sein. Ein erster Schritt zur Systemidentifikation wird im nächsten Kapitel untersucht.

Kapitel 5 verwendet lernbasierte Methoden, um die Entwicklung von steuerungsbasierten Systemen zu fördern. Die in Kapitel 4 aus der impulsiven Steuerung gezogenen Lehren werden für eine neuronale inverse optimale Steuerung – Neurocontrol – genutzt. In realen Szenarien kann es vorkommen, dass ein auf einem Systemmodell basierender Regler aufgrund verschiedener Probleme nicht wie gewünscht funktioniert. Beispiele hierfür sind interne und externe Störungen, unsichere Parameter und nicht modellierte Dynamik [37]. Darüber hinaus können Datenknappheit und seltene Messungen in der klinischen Praxis zu einer suboptimalen Leistung des Reglers führen [36]. Alle genannten Probleme können zusätzliche Modellierungsspezifikationen erfordern, deren Erfüllung kompliziert werden kann. Als Alternative zu umfangreichen Modellierungsschemata können rekurrente neuronale Netze hoher Ordnung (RHONN) verwendet werden, um das gewünschte dynamische System darzustellen [38]. RHONNs zeichnen sich durch Eigenschaften wie einfache Implementierung, relativ einfache Struktur und Robustheit gegenüber Störungen aus. Außerdem können die Parameter des Netzes online angepasst werden. Darüber hinaus ist es möglich, bereits bekannte Informationen über die Systemstruktur in das RHONN zu integrieren [38, 39]. Neuronale

Netze bestehen aus mehreren miteinander verbundenen Verarbeitungselementen, den Neuronen. Wie die Neuronen miteinander verbunden sind, bestimmt ihre Architektur. Bei Anwendungen zur Systemidentifizierung und -steuerung kommen in der Regel rekurrente Netzarchitekturen zum Einsatz [40]. In der rekurrenten Struktur sind die Ausgänge eines Neurons eine Rückkopplung zu demselben Neuron oder denselben Neuronen in den vorangegangenen Schichten. Dadurch können sie genau vorhersagen, was in Kürze kommt [14]. Somit ermöglicht die rekurrente Struktur ein tieferes Verständnis der Zeitreihendynamik bei der Systemidentifikation [41, 42].

Für das Training des Netzes verwenden wir den erweiterten Kalman-Filter (EKF). Der EKF findet die minimale Fehlerschätzung des Zustands unter Verwendung der beobachteten Daten und der vorherigen Schätzung. In diesem Fall sind die RHONN-Gewichte der Zustand, der angepasst werden muss. Der EKF ermöglicht ein Training, bei dem die Epochengröße für jeden Schritt des Filterungsprozesses reduziert wird [44, 45]. Diese Eigenschaft macht die EKF rechnerisch effizienter, da Schätzungen aus den gesamten vergangenen Beobachtungen nicht erforderlich sind [46, 44]. Anhand des RHONN- und EKF-Trainings ermitteln wir die Modelle für den Influenza-Wirt und das Medikament (PK/PD-Schema). Das kontrollbasierte System berechnet die Dosis entsprechend der Neurokontrolle. Ähnlich wie bei der Strategie in Kapitel 4 liefert die Neurosteuerung die Dosierung sowohl für das Influenzamodell als auch für das neuronale Modell. Das neuronale Modell gibt dem Kontrollsystem Rückmeldung.

Das Zielzellenmodell würde die Dynamik der Grippeinfektion darstellen. Frühere Arbeiten, in denen dieses Modellierungsschema verwendet wurde, warfen jedoch Probleme mit der Identifizierbarkeit der Parameter auf. Die Studien weisen darauf hin, dass die Parameterwerte mit Vorsicht verwendet werden sollten. Die Werte können nicht eindeutig aus den jeweiligen experimentellen Daten geschätzt werden [10, 47, 48]. Aufgrund dieser Art von Einschränkungen bei der Identifizierbarkeit im Zielzellenmodell hat Boianelli *et al.* [49] ein vereinfachtes Schema vorgeschlagen, das die Dynamik von Influenzavirus und CD8+ T-Zellen beschreibt. Das Modell besteht aus der Dynamik des Virus und der CD8+ T-Zellen auf Wirtsebene, wobei die Arzneimitteldynamik über die PK/PD-Phasen der NIs integriert werden kann. Dieses Schema wird verwendet, um die Dosisplanung mithilfe von Neurocontrol anzupassen. Die vollständige theoretische Grundlage für das Neurokontrollschema wird für die zeitdiskrete impulsive Kontrolle beschrieben. In Übereinstimmung mit Kapitel 4 wird die Robustheit des impulsiven Neurocontrollers durch MCS untersucht. Bei der Anpassung der Grippetherapie erreicht die Neurosteuerung in den MCS-Tests eine ähnliche Wirksamkeit wie die Festdosis (über 90%). Die Gesamtdosis des Medikaments wird bei einer frühen Behandlung, beginnend bei 1 Tag nach der Infektion, um fast 40% reduziert. Künftige Systeme für Beobachter können lernbasierte Methoden wie maschinelles Lernen einbeziehen. Mithilfe dieser Grundlagen können minimalinvasiv erfasste hämatologische Parameter verwendet werden, um auf die Viruslast in der Lunge von Mäusen zu schließen [50]. Andere Akteure wie Leukozyten und Zytokine wurden in der letzten Studie ebenfalls abgeleitet. Diese Arten von minimal-invasiven Instrumenten sollten in der Lage sein, Beobachtern und Neurokontrollstrategien Informationen über den Krankheitsverlauf zu liefern.

Chapter 1

Introduction

Influenza is an infectious respiratory disease caused by the influenza virus, there are four types of viruses, A, B, C and D. Influenza A and B viruses spread and cause seasonal epidemics. The symptoms related to influenza infection vary from mild to severe, covering cough, sore throat, runny nose, headache, fever, fatigue, and muscle pain. The strength of the symptoms is usually associated with the strength of the infection, going from a moderate respiratory disease in the upper respiratory tract to severe and occasionally lethal pneumonia due to influenza virus or secondary bacterial infection of the lower respiratory tract. Influenza virus-related diseases are more severe among high-risk groups such as toddlers under 59 months, pregnant women, seniors over 65 years old, immunocompromised individuals, and people with chronic medical conditions [1]. Seasonal epidemics are distinguished by regular annual events, however, sporadic pandemic outbreaks also appear involving zoonotic origin influenza strains, showing high rates of global level morbidity and mortality. Characterized by the severity of the infection and increased mortality, a central player in influenza pandemics is the introduction of an antigenically different influenza strain that features surface glycoproteins, haemagglutinin (HA), and neuraminidase (NA), to which the human immune system is relatively naive with lack of antibody-based population immunity [1, 2]. Cases reflecting these phenomena in influenza A are, the 1918 pandemic, where the majority of the population seemed to be naive for both the H1 HA and the N1 NA, and in 1957, when there was little population immunity to both H2 and N2 [51, 52]. More recently, in 2009, a seasonal H1N1 virus was circulating in humans, but the incoming pandemic H1N1 virus had antigenically distinct H1 and N1 surface glycoproteins [53].

Since the first report describing the isolation of the influenza virus in 1933, the antibody responses to the influenza virus surface glycoproteins, particularly to HA, have been identified to give protection against influenza virus infection [54, 55]. The immune responses of antibodies that bind to HA and NA can be broadly protective since these proteins are gladly accessible to antibodies on the virion and infected cells [5]. The study of the magnitude and breadth of antibody responses to divergent influenza strains in sequential infections is central to uncover insights on the effectiveness of vaccination strategies and to understand how immunity induced by one strain is effective against another –the so-called antibody cross-reaction. Cross-reactive antibodies (Abs) are of great importance for protection from infection with drifted (seasonal) and shifted (pandemic) influenza viruses. Besides, antibody responses to natural infections are usually broader and longer-lived than antibody responses induced by vaccination, however, the mechanisms describing the Abs prevalence, functionality, and further mechanisms of these responses remain largely unclear [5, 56, 57]. Therefore, extensive studies regarding Abs cross-reaction development along with data from infections are needed to guide understanding of influenza infection and vaccine design.

On the other hand, antiviral drugs are a fundamental part of the treatment of influenza infection and disease. For regular influenza seasons, antiviral drugs are primarily used for treating severely affected patients, in particular those with compromised immune systems. Besides, for pandemic influenza, especially in the period before a vaccine is available, antiviral drugs are essential for treating infected patients and preventing infection in individuals who have been exposed [4]. Neuraminidase inhibitors (NIs) such as zanamivir and oseltamivir are currently approved antivirals for influenza. These can block the enzymatic activity of the NA protein. Oseltamivir became the most commonly used drug due to its oral delivery compared to the inhaled zanamivir, serving for the treatment of uncomplicated seasonal influenza and severely infected patients [58, 59]. However, recent studies highlight the limitations of NIs at host and population levels that should be overcome in future drug and treatment design [60]. Novel strategies for antiviral scheduling, drug development, and dosing can play an important role to combat influenza infections. A better understanding of the mechanisms of drug delivery and response, as well as its interactions with the virus and the immune response, is a key part of treatment development. As a guiding framework, the pharmacologic disciplines, pharmacokinetics (PK) and pharmacodynamics (PD), known as the PK/PD approach, leverage different kinds of preclinical and clinical data through mathematical models, assisting decision-making through modeling and simulation [9]. Furthermore, treatment tailoring can be supported, since PK/PD-based models and parameters for influenza therapies are usually available [61]. Based on mathematical models of biological systems and the PK/PD approach, recent theoretical control engineering strategies have been integrated into the design of individual treatment, for instance, in diabetes [62] and infectious diseases such as HIV [35, 63] and influenza [64, 65].

The herein thesis attempts to uncover hidden mechanisms in modeling and control-based approaches for influenza infection. First, the Abs cross-reaction mechanisms to sequential influenza infections are explored through a stochastic model. In a theoretical framework, accounting for level of difference between antigens of infection, the model is challenged to represent the breadth and magnitude of Abs response generally observed in mice experiments. We integrate previous modeling schemes to represent the affinity maturation process and the dynamics that affinity thresholds might undergo for the development of breadth responses together with high Abs magnitude within a set of antigens. Through diverse model scenarios and parameter tuning, the computational simulations highlight that changes in time of infection and the B-cells population are relevant, however, the affinity threshold of B-cells between sequential infections is a necessary condition for the successful Abs cross-reaction. On the other hand, regarding control-based treatment, theoretical techniques are developed adapting impulsive and inverse optimal control strategies. The framework integrates the mathematical models of PK/PD phases and host-level influenza dynamics to estimate optimal drug quantities tailored to host response. Various concepts from a rather classical control approach, such as passivity, stability, and bounded input, are further adapted to the problem of treatment tailoring. Theorems and corollaries are presented with the corresponding mathematical foundations. In addition, the problem of data scarcity and infrequent measures is addressed by means of learning-based methods for system identification, through neural networks. The neural methods are also combined with the impulsive control framework to form a neurocontrol strategy. This machinery allows for exploring related control frameworks with implications for observers in biological systems with potential use for antiviral treatment development.

1.1 Overview and contributions

Chapter 2 presents from a rather biological viewpoint an overview of influenza infection characteristics in the host as well as the global threat in the last years. The chapter addresses influenza epidemics and pandemics, a general view of the virus components, the pathogenesis of influenza infection exploring diverse players and their role in both sides, virus and host response, focusing on B–cell and Abs responses. From the last, the Abs breadth and magnitude of response are introduced accounting for Abs cross-reaction in animal experiments. On the other hand, the chapter presents part of the current options of antiviral treatment, focussing on the treatment tailoring framework. For this approach, a novel concept of control-based treatment tailoring is introduced incorporating the PK/PD phases of NIs and influenza mathematical models for antiviral scheduling.

Chapter 3 presents a theoretical modeling scheme for the Abs cross-reaction in sequential infections with related antigens, motivated by observed phenomena in experiments using sequential infections with influenza virus [5]. The framework is formulated to represent the broad Abs dynamics to a given set of antigens. Affinity maturation processes and binding flexibility are explored for testing the breadth and magnitude of Abs responses. The contributions of this chapter are the following:

- Integration of modeling schemes for the antigenic difference and the affinity dynamics of the antigen-antibody pair.

- The model shed light on B-cells affinity threshold dynamics between sequential infections, pointing it as a critical setting for rendering cross-reaction phenomena.

- Flexibility in affinity between infections allows for exploring the echo of the first infection to the second infection. Some examples are the antigen-specific behavior, the rather slight effects of the antigenic difference, and the lasting of Abs from the first to the second infection. High Abs magnitude is developed in the complete set of antigens after the second infection.

- Modeling schemes highlight the necessity for exploring evolutionary affinity schemes that autoregulate the Abs cross-reaction dynamics accounting for immune elements, such as memory B-cells and diverse germinal centers. This may render a potential reformulation applicable to integrate Abs response within and between influenza group 1 and group 2.

Chapter 4 introduces mathematical models of influenza infection in the host as well as drug compartment models, under the PK/PD approach. Incorporating theoretical concepts of inverse optimal and impulsive control, novel tailoring approaches are developed for control-based influenza treatment. For completeness, theoretical examples are illustrated for diverse scenarios. The contributions of this chapter are the following:

- Integrate inverse optimal control strategies with impulsive control methods for drug dose estimation based on viral and drug dynamics. Treatment strategies are tested at individual and population levels, reaching comparable drug efficacy of the current Food and Drug Administration (FDA) (WHO approved) recommendations (98%) with a drug's quantity reduction of up to 44%.

- At the theoretical level, the adaptation of previous results in discrete-time inverse optimal control systems into the impulsive fashion, accounting for passivity- and Lyapunov-based schemes. The corresponding foundations with mathematical proofs are presented.

- Bounded control strategies to be applied directly in drug dose estimation accounting for overdose prevention.

- Exploring limitations of the technology application in clinical practice, the tailoring strategies highlight the necessity of developing system identifiers and observers.

Lessons learned from control–based influenza treatment strategies are further employed accounting for a neural state identifier, intended to explore solutions in real-world practices. In this sense, **Chapter 5** introduces the so-called neurocontrol treatment scheduling, which applies the impulsive controller combined with a Recurrent High Order Neural Network (RHONN). The contributions of this chapter are the following:

- Introduce the application of a RHONN as a system-state estimator, accounting for a theoretical basis of neural networks using the Extended Kalman Filter as the training algorithm.

- Since the RHONN is used as a render of the unknown system (influenza within-host model), the impulsive control strategies are applied based on the RHONN estimations. This scheme may guide learning-based strategies for solving clinical affairs such as data scarcity at the host level.

- The theoretical basis for the neurocontrol scheme is described for discrete-time impulsive systems which robustness is challenged through an Monte Carlo survey in influenza treatment.

- The neurocontrol-based treatment reaches a similar efficacy to the FDA-approved treatment (95%) while saving almost 40% of the drug in early treatment.

This thesis concludes in **Chapter 6** summarizing main ideas, limitations and results, and points out open questions for future research. Some of the results of this thesis have led to the following peer-reviewed publications:

- **G. Hernandez-Mejia**, A. Y. Alanis, and E. A. Hernandez-Vargas, Neural inverse optimal control for discrete-time impulsive systems, Neurocomputing, vol. 314, pp. 101-108, 2018. `https://doi.org/10.1016/j.neucom.2018.06.034`
- **G. Hernandez-Mejia**, A. Y. Alanis, M. Hernandez-Gonzalez, R. Findeisen, and E. A. Hernandez-Vargas, Passivity-based inverse optimal impulsive control for influenza treatment in the host, IEEE Transactions on Control System Technology, 2019. `https://ieeexplore.ieee.org/document/8632723`
- **G. Hernandez-Mejia** and E. A. Hernandez-Vargas, Uncovering antibody crossreaction dynamics in influenza A infections, Bioinformatics, vol. btaa691, 2020. `https://doi.org/10.1093/bioinformatics/btaa691`
- **G. Hernandez-Mejia**, E. A. Hernandez-Vargas, A. Y. Alanis and N. Arana-Daniel, Recurrent High Order Neural Networks Identification for Infectious Diseases, Proceedings of the International Joint Conference on Neural Networks (IJCNN), Rio de Janeiro, Brazil, pp. 1-7, 2018. `https://ieeexplore.ieee.org/document/8489067`
- **G. Hernandez-Mejia** and E.A. Hernandez-Vargas. PK/PD-Based Impulsive Control to Tailor Therapies in Infectious Diseases. 21st IFAC World Congress (Virtual), Berlin, Germany, 2020. `https://doi.org/10.1016/j.ifacol.2020.12.418`
- **G. Hernandez-Mejia**, X. Du and E. A. Hernandez-Vargas, Bounded Input Impulsive Control for Scheduling Therapies, Journal of Process Control, vol. 102, pp. 34–43, 2021. `https://doi.org/10.1016/j.jprocont.2021.03.003`

Further peer-reviewed publications prepared during the doctoral studies but not included in this thesis

- **G. Hernandez-Mejia**, E. N. Sánchez, V. M. Chan, and E. A. Hernandez-Vargas. Impulsive Neural Control to Schedule Antivirals and Immunomodulators for COVID-19. In 2022 IEEE 61st Conference on Decision and Control (CDC) (pp. 5633-5638). IEEE. `https://10.1109/CDC51059.2022.9992454`
- G. D. Vega-Magdaleno, A. Y. Alanis, **G. Hernandez-Mejia** and E. A. Hernandez-Vargas, Impulsive MPC for Influenza Infection Treatment at Variable Time, Special issue: 2nd IFAC Conference on Modelling, Identification and Control of Nonlinear Systems (MICNON), Guadalajara, Mexico, 2018. `https://doi.org/10.1016/j.ifacol.2018.07.258`
- C. Parra-Rojas, V. K. Nguyen, **G. Hernandez-Mejia**, and E. A. Hernandez-Vargas, Neuraminidase inhibitors in influenza treatment and prevention -is it time to call it a day?, Viruses, vol. 10, no. 9, p. 454, 2018. `https://doi.org/10.3390/v10090454`

- A. E. S. Almocera, **G. Hernandez-Mejia**, C. Parra-Rojas, and E. A. Hernandez-Vargas, The trichotomy of pneumococcal infection outcomes in the Host, Communications in Nonlinear Science and Numerical Simulation, vol.73, p.1-13, 2019. `https://doi.org/10.1016/j.cnsns.2019.01.025`

- **G. Hernandez-Mejia** and E. A. Hernandez-Vargas, When is SARS-CoV-2 in your shopping list?, Mathematical Biosciences, vol. 328, 108434, 2020. `https://doi.org/10.1016/j.mbs.2020.108434`

- M. Hernandez-Gonzalez, **G. Hernandez-Mejia**, A. Y. Alanis and E. A. Hernandez-Vargas, State Estimation for Stochastic Nonlinear Systems with Applications to Viral Infections, Proceedings of the 18th European Control Conference (IEEE-ECC), Naples, Italy, 2019. `https://ieeexplore.ieee.org/document/8795918`

- E. A. Hernandez-Vargas, A. Boianelli and **G. Hernandez-Mejia**, Bacterial pneumonia fate decisions, Part of special issue: 10th IFAC Symposium on Biological and Medical Systems (BMS), São Paulo, Brazil, 2018. `https://doi.org/10.1016/j.ifacol.2019.02.001`

Chapter books

- **G. Hernandez-Mejia** and E. A. Hernandez-Vargas. Chapter 8 - Learning-Based Identification of Viral Infection Dynamics, Book: Artificial Neural Networks for Engineering Applications, Academic Press, 2019. `https://doi.org/10.1016/B978-0-12-818247-5.00017-4`

- **G. Hernandez-Mejia**. Chapter 6 - Control-based drug tailoring schemes towards personalized influenza treatment, Book: Feedback Control for Personalized Medicine, Academic Press, 2022. `https://doi.org/10.1016/B978-0-32-390171-0.00015-9`

Chapter 2

Panorama of influenza infection, host response and treatment

This chapter explores the influenza A virus infection characteristics in the host as well as the global threat in the last years. Regarding within-host aspects, the influenza pathogenesis, host immune responses, and the so-called antibodies (Abs) cross-reaction are introduced. The chapter also presents the overall panorama of influenza treatment, opening tailoring strategies through control-based dose estimation systems. *This chapter presents partial content of Ref. [66]*[1].

2.1 Influenza pandemics overview

The flu-inducing agent - the influenza virus- discovery took a long journey. In 1892, Richard Pfeiffer isolated from the noses of flu-infected patients a small rod-shaped bacterium that he thought was the causative agent of influenza [67, 68]. This bacterium-agent idea remained until the early 1930s when Richard Shope isolated the influenza virus from infected pigs, giving the first description of the etiological cause of influenza [69, 70, 71]. This discovery was shortly followed by the isolation of the virus from humans by the group of Patrick Laidlaw (Wilson Smith, Christopher Andrewes, and Patrick Laidlaw) in 1933 [54], concluding that a virus, not a bacterium, caused influenza. On the other hand, numerous authors have tried to identify pandemics throughout the entire history, hence, reports of possible influenza pandemics can be found in the literature from the early Greek writings of 412 BC to the more precise documentation of the present time. Along with several reports dating from the 14th and 15th centuries, the first convincing report was by Molineux in 1694 [72]. Also, diverse references to influenza epidemics have been made for the 17th century in America and Europe. Since the 18th century, the quality and quantity of collected data increased and, for the first time, medical reports started to comment on the number of infected individuals, whether considering the event as an epidemic or a pandemic (Definition 2.1 and 2.2), the spread throughout countries, and the possible origins of the virus strains

---

[1] Partial reprint from Ref [66], Gustavo Hernandez-Mejia, Control-based drug tailoring schemes towards personalized influenza treatment in *Feedback Control for Personalized Medicine*, pp. 109-128., Copyright (2022), with permission from Elsevier. Subsection 2.2.4 and Figure 2.4 are first published in this thesis.

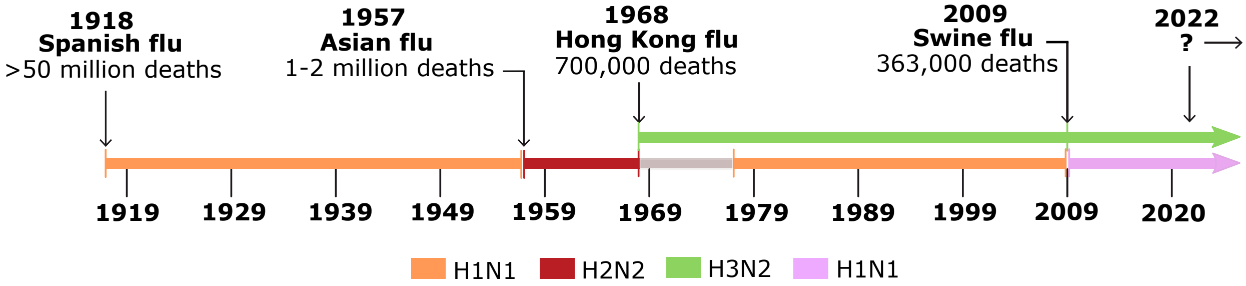

Figure 2.1: Influenza pandemics. After the 1918 Spanish flu pandemic, caused by a founder H1N1 influenza A virus, three following pandemics in 1957 (Asian flu), 1968 (Hong Kong flu), and 2009 (Swine flu) were caused by reassorted descendants of the 1918 virus. Color-coded timelines depict the years of annual epidemics of seasonal influenza that occurred after each pandemic along with the estimated number of fatalities. This shows that pandemic events including the circulating or emerging influenza strains may potentially occur in the next years. This figure was taken and adapted from Taubenberger *et al.* [76].

[73]. Before continuing with some historical landmarks of influenza from the 20th century on, let us set some definitions.

Definition 2.1. *Epidemic. This refers to an increase, often sudden, in the number of cases of a disease above what is normally expected in that population in that area. Outbreak carries the same definition of epidemic but is often used for a more limited geographic area [74].*

Definition 2.2. *Pandemic. This indicates an epidemic that has spread over several countries or continents, usually affecting a massive number of people [74].*

Definition 2.3. *Virus Reassortment. A process of the genetic recombination of segmented RNA viruses where co-infection of a host cell with multiple viruses may result in the mixing of gene segments to generate progeny viruses with novel genome combinations [75].*

Four pandemics of human influenza have occurred since the 1918 pandemic which was caused by influenza A H1N1 virus, such event is associated with more than 50 million deaths, hence, considered the most devastating influenza pandemic to date [77]. As shown in Figure 2.1, the influenza pandemics of 1957, the one of 1968, and the most recent in 2009, were caused by influenza A H2N2, H3N2, and H1N1 viruses, respectively. While in 1977 influenza A H1N1 virus restarted circulation in humans without pandemic effects since the strain was similar to that which preceded the 1957 H2N2 pandemic, the 2009 pandemic influenza A H1N1 virus, in contrast, was antigenically different from the previous seasonal influenza A H1N1 viruses. This new virus replaced the last circulating influenza A H1N1 strains [2, 77]. Human H3N2 viruses co-circulated with human 1918 lineage seasonal H1N1 viruses from 1977 to 2009, when this parentage was replaced by the new swine-origin H1N1 2009 pandemic virus due to reassortment (Definition 2.3). Since 2009, H3N2 viruses have co-circulated with 2009 pandemic lineage H1N1 viruses in humans. Seasonal influenza B viruses (not shown) are co-circulating in humans along with influenza A viruses. In this sense, uncovering the secrets of the previous influenza pandemics and the virus involved has been extremely rewarding, but still, challenges remain an urgent necessity at diverse stages covering from epidemiology levels to host-related points, such as the immune response, virus pathogenesis, and treatment of influenza infection.

2.2 Influenza virus in the host

2.2.1 Influenza virus structure

Influenza A virus is an enveloped RNA virus with eight single- stranded RNA segments located inside the virus particle, a general scheme is shown in Figure 2.2. RNA segments encode the viral glycoproteins haemagglutinin (HA) and neuraminidase (NA). The HA glycoprotein has two characteristic structures, the 'stalk' domain and the globular 'head' domain. The HA mediates binding to sialic acid-containing receptors and viral entry. The NA, on the other hand, allows releasing viruses bound to non-functional receptors, facilitating viral spread [2].

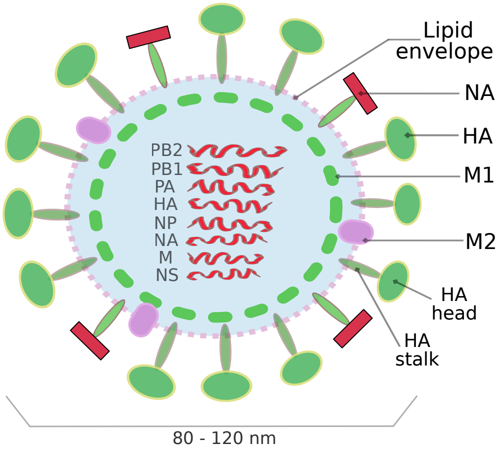

Figure 2.2: Influenza A virus structure. The virus contains eight RNA segments, which encode RNA polymerase subunits, viral glycoproteins (haemagglutinin (HA), with its globular 'head' and 'stalk' structures, facilitate viral entry, and neuraminidase (NA), which allows viral release), viral nucleoprotein (NP), matrix protein (M1), membrane protein (M2), and the nonstructural protein. The viral particle (virion) is formed by a lipid membrane derived from the infected cell. Figure adapted from Ref. [2] and Ref.[76].

The RNA genome is bound by the viral nucleoprotein (NP) encoded by the RNA segment 5 and the rest of the RNA segments, 7 and 8, encode the matrix protein (M1) and membrane protein (M2), and the nonstructural protein (NS). It is thought that the M1 protein provides a scaffold that helps to build the structure of the virion (the viral particle) and regulates the viral RNA segments in the cell. The M2 protein is required for viral entry and exit and, together with HA and NA glycoproteins, is located on the surface of the virus anchored in a lipid membrane that comes from the infected cell [76].

Definition 2.4. *Antigenic shift. The process by which two or more different strains of a virus, combine to form a new subtype that has a mixture of the surface antigens of the two or more original strains. Antigenic shift is a specific case of reassortment that confers a phenotypic change.*

Definition 2.5. *Antigenic drift. A type of genetic variation in viruses, arising by the accumulation of mutations in the virus genes that code for virus-surface proteins that host antibodies recognize. The process results in a new strain of virions that are not effectively inhibited by antibodies responses from previous strains.*

The segmented nature of the influenza viral genome enables reassortment of genomic RNA segments, the so-called antigenic shift (Definition 2.4) when two viruses of the same type (two influenza A viruses or two influenza B viruses) infect the same cell. Animal reservoirs (as those of avian strains) provide a source of antigenically diverse HA and NA genes

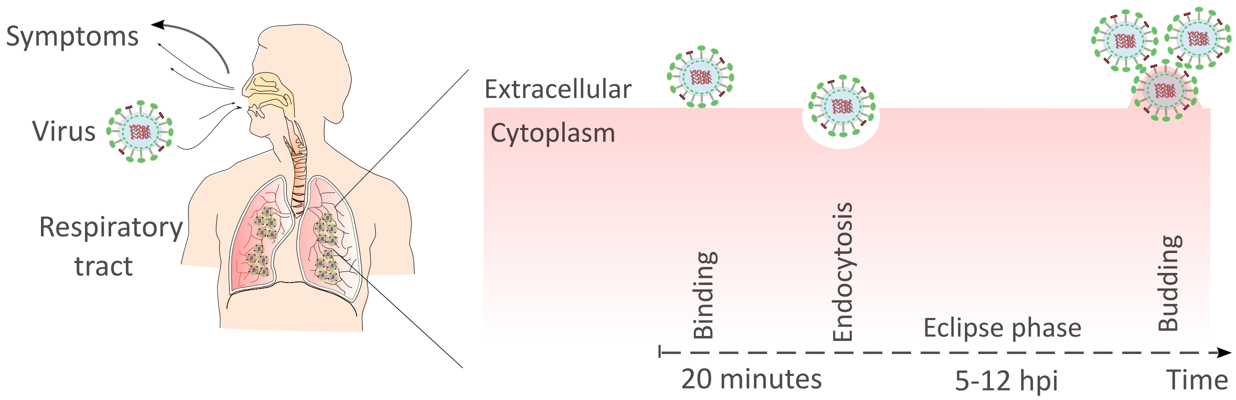

Figure 2.3: Influenza A virus infection phases. The main phases of influenza infection in the host. Virions enter the respiratory tract and bind to target cells. Afterward, virions enter the eclipse phase which ranges 5-12 hours post-infection (hpi), and start to replicate before infecting other cells. This figure was adapted from Boianelli *et al.* [49].

that can be exchanged by reassortment after co-infection of the same host, increasing virus diversity and in some instances leading to the generation of human pandemic influenza virus strains with HA and/or NA derived from animal strains. Between pandemics, annual seasonal influenza A viruses are generated by continuous viral genetic mutations, the antigenic drift (Definition 2.5), and by intra-subtype reassortments [2, 75, 78]. The HA and NA viral proteins are the most antigenically variable and even classified into antigenically diverse subtypes in the case of the influenza A virus, a total of 16 antigenically different HA and 9 antigenically different NA serotypes or subtypes have been identified among different avian strains [2]. Of note, since HA and NA viral glycoproteins are located at the surface of the virion, they are the main targets for protective Abs induced by influenza virus infection and vaccination [57, 79].

2.2.2 Influenza virus pathogenesis

Influenza viruses are transmitted in different routes, in humans, for instance, through the respiratory route whereas avian influenza viruses in wild birds are transmitted through the fecal-oral or fecal–respiratory routes [80, 81]. The virus targets epithelial cells of the respiratory or intestinal tract for infection and productive replication. The severity of infection in humans is associated with replication of the virus in the lower respiratory tract, developing a serious inflammation process resulting from immune cell infiltration [82].

An influenza infection starts when virions enter the upper portion of the respiratory tract, once inside, they follow the different phases shown in Figure 2.3. First, in the binding phase, virions attach to the receptors of the epithelial cells' surface due to the fusion capacity of the influenza HA protein [82]. Approximately 20 min after infection, the virion is endocytosed inside the epithelial cell (endocytosis phase) [83]. Next, in the cytoplasm, the viral RNA is released and used to produce new virions that are later released to the extracellular environment in the budding phase. The period between successful cell infection and the virus release is an eclipse phase which ranges from 5 to 12 hours post-infection (hpi) [84].

The newly generated virions start to infect other cells favored by the NA activity which prevents unfruitful binding of new virions HA to receptors in the viral glycoproteins and on the membrane of the infected cells, this facilitates viral spread [49].

2.2.3 Host immune response

Host immunity, composed of the innate and adaptive immune responses, represents a barrier that influenza virus needs to overcome to replicate and propagate in new hosts [85]. The innate immune system forms the first element of defense against infection, whose components' goal is to prevent respiratory epithelial cells from it, using mucus, collectins, and intracellular sensing mechanisms [86]. Through sensing, rapid innate cellular immune responses are induced to control virion replication where influenza RNA is recognized in infected cells via pattern-recognition receptors. Signaling of various receptors (toll-like receptors) leads to the production of proinflammatory cytokines and type I interferons (IFN-I), such as IFN-α and IFN-β, that inhibit protein synthesis in host cells [87, 88]. After infection of the alveoli, alveolar macrophages become activated and phagocytose apoptotic influenza infected cells, reducing viral spread [89]. In addition, dendritic cells, antigen-presenting cells, monitor the airway lumen using their extended dendrites through the tight junctions between the airway epithelial cells, detecting virions and apoptotic bodies from infected cells. Finally, natural killer (NK) cells recognize antibody-bound influenza infected cells and lyse them through the antibody-dependent cell cytotoxicity process. It is also thought that NK cells assist in regulating the infection-induced pathology [85, 90].

On the other hand, the adaptive immune response to influenza considers elements such as pathogen-specific Abs and cytotoxic CD8+ T cells responses [85]. The CD8+ T cells (cytotoxic T lymphocytes) and CD4+ T cells display cytolytic activity to infected cells, they recognize and eliminate virus-infected cells, preventing the production of progeny virus [91]. Governed by B-cells activity, antibody response correlates with protective immunity and is considered an central part of the response to both, influenza infection and vaccination [54]. During influenza pathogenesis, diverse proteins become reachable to Abs. HA and NA proteins are accessible on virions and infected cells. Parts of the influenza M2 ion channel are also accessible, mostly on the surface of infected cells. It is possible that some internal viral proteins, M1, NP, the polymerases, and the nuclear export protein (NEP), become accessible in cells that die after infection [57, 92]. Such accessibility phenomena indicate that not all influenza virus antigens are expressed to similar levels and, therefore, are not similarly accessible to B-cell receptors. In this direction, discrete antigenic sites on the head domain of HA, on which the receptor-binding site (RBS) is located, seem to be the preferential target of the Abs response. These sites present immunodominance (Definition 2.6) over most other B-cell epitopes of the virus, however, the reasons for the antigenic immunodominance at molecular and immunological levels remain to be uncovered [3, 93, 94, 95].

Definition 2.6. *Immunodominance. The phenomenon in which an antigen or epitope is preferentially targeted by the immune system compared with other antigens.*

Definition 2.7. *B-cell. B (bursal or bone marrow-derived) lymphocytes. A population of cells that express clonally diverse cell surface immunoglobulin (Ig) receptors recognizing specific antigenic epitopes.*

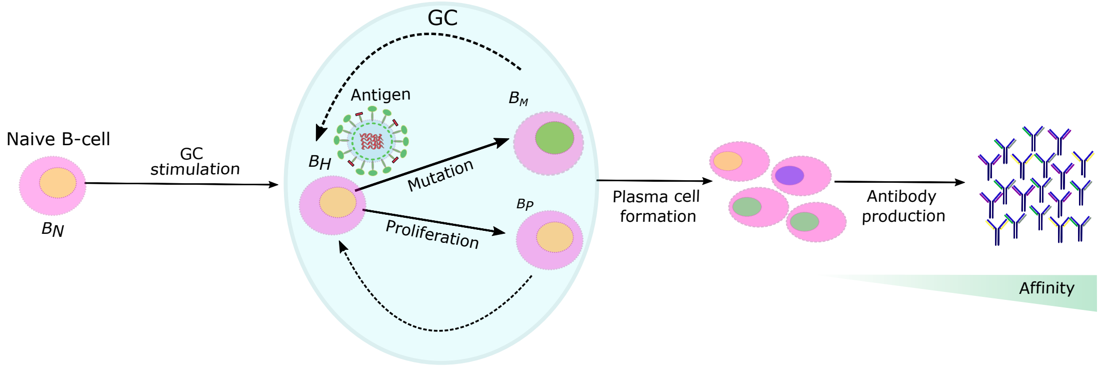

Figure 2.4: Germinal center (GC) general model. Stimulation of naive B-cells (B_N) into GCs leads to cyclic migration of B-cells that gain affinity via the affinity maturation process, forming high-affinity B-cells (B_H). The last produce two cell populations, one of the same characteristics of high-affinity B-cell, identified as the proliferation of B-cells (B_P), and the second one, the mutated B-cells (B_M), the ones undergoing affinity maturation. Dashed arrows in the GC oval stand for the several cycles of mutation and proliferation to reach affinity for the antigen. B-cells differentiate into plasma cells which afterward produce Abs that incorporate the diversity of clones and affinity of the population.

Definition 2.8. *Plasma cell. A non-dividing, terminally differentiated antibody-secreting cell of a B-cell lineage.*

Definition 2.9. *Somatic hypermutation (SHM). A phenomenon in which point mutations are introduced in the heavy or light chain variable region gene segments, resulting in a change in the expressed protein, which may alter affinity or specificity for antigen [57].*

Definition 2.10. *Antibody. A large, Y-shaped protein used by the immune system to identify and neutralize foreign objects such as pathogenic bacteria and viruses by recognizing a unique molecule of the pathogen, called an antigen.*

Definition 2.11. *Germinal centers (GCs). These are compartments within secondary lymphoid organs that contain mitotic cells. They are the site of B cell clonal expansion, SHM, and affinity-based selection, the combination of which results in the production of high-affinity antibodies [17].*

Antibody response echoes a large set of events, for instance, upon exposure to antigen, Abs attain high affinity through SHM of immunoglobulin genes in B-cells in a process known as affinity maturation (AM) [15]. Antigen-induced B-cell activation and differentiation in secondary lymphoid tissues are mediated by dynamic changes in gene expression, giving rise to the germinal center (GC) reaction (Definition 2.11). The GC reaction is characterized by clonal expansion, SHM, and selection for the increased affinity of B-cell receptors (BCR) for its unique antigenic epitope through AM, following a Darwinian evolution-like path [16]. B-cells are subsequently selected based on the ability of their mutant Abs to bind antigen, which later leads to increased fitness of the population as a whole [17, 18, 19]. In GCs, B-cells follow one of three paths, they can differentiate into plasma cells (PCs) that secrete Abs, they can re-establish a nonproliferative state and join the memory B-cell pool, or they can enter the GC reaction, the process results in the progressive increase of Abs affinity over time [16].

A general model of the path that B-cell follows from naive cells to Abs production is shown in Figure 2.4. Regarding broad protection, experiments in mice have shown that the reaction of the GC to complex antigens, such as influenza, promotes a wide range of specificities and affinities, with potential advantages for broad protection [96]. Similar scenarios have been found for human infection [93, 97].

A key constraint to GCs processes is that they select Abs with higher affinity for antigen, however, further exploration is needed for understanding Abs ability to neutralize the virus and the cross-reaction potential to other strains with respect to the present pathogen [16]. The influenza antigenic drift renders high-affinity protective Abs from one season that potentially become ineffective against newly emerging strains. Thus, further studies of GCs reaction to influenza are fundamental for understanding the breadth and magnitude of Abs response. For reviews of diverse mechanisms of B-cells and Abs responses to the influenza virus as well as GC activity, see Refs. [57, 17, 18, 98].

2.2.4 Antibody cross-reaction to influenza

Individuals might be infected or exposed to influenza viruses several times during a lifetime, however, Abs responses to the first infection in life and its immune imprinting (Definition 2.12) might bias further responses to subsequent exposures. This phenomenon, originally named as the original antigenic sin, strongly depends on the relatedness of the two virus variants [95, 99, 100, 101].

Definition 2.12. *Antigenic imprinting. A phenomenon that describes the bias of antibody response due to previous immune history, this can influence vaccines effectiveness and has been reported in diverse viruses.*

Definition 2.13. *HA proteins groups 1 and 2. Group 1 HA proteins: a phylogenetic cluster of influenza HA subtypes that includes H1, H2, H5, H6, H8, H9, H11, H12, H13, H16, H17, and H18. Group 2 HA proteins: a phylogenetic cluster of influenza HA subtypes that includes H3, H4, H7, H10, H14, and H15 [5].*

Definition 2.14. *Cross-reactivity. Refers to the phenomenon by which an antibody directed against one specific antigen is successful in binding with another different antigen due to similar three-dimensional structural regions - the epitopes - between the two antigens.*

Abs that bind to the head domain of HA typically have potent neutralizing activity and generally have haemagglutination inhibition (HI) activity, Abs that exhibit this function are relatively strain-specific because of the mutating nature of the HA head domain [102]. On the other hand, HA stalk-reactive Abs are often cross-reactive within and across HA subtypes due to the conserved nature of the stalk domain [103, 104]. It has been observed that stalk-reactive antibodies are able to bind to group 1 HAs or group 2 HAs (Definition 2.13) [5, 56, 105]. This class of Abs probably forms the majority of the cross-reactive Abs that are induced by natural infection, a phenomenon also observed in memory B-cells cross-reaction with influenza groups 1 and 2 HAs in human adults [106, 107]. In this sense, thus, understanding cross-reactive immunity is central for the development of universal vaccine strategies that promote Abs recall to protective levels.

Several mathematical models have been proposed to give *in silico* insights of immune players in the Abs response to infection [108]. Most of the models question mechanisms for antibody generation [7] taking into account elements such as B-cells, plasma cells, memory B-cells, the affinity maturation process in GCs, and follow specific setting for the antigen-B-cell binding for guiding Abs cross-reaction [7, 6, 109, 8, 110]. Based on such modeling schemes, we explore how Abs breadth and magnitude are guided in sequential infections following observations of Abs cross-reaction in animal experiments [5]. Unlike previously explored schemes, in Chapter 3 we explore how affinity flexible features could favour Abs magnitude of response, questioning properties that differentiate the breadth characteristics between sequential infections, detailing and updating our work of Ref. [111].

First, we integrate diverse theoretical components from previous modeling approaches originally focussed on influenza and HIV (antigens) infection, such as the representation of antigens using strings of characters, differences between them and processes for B-cells to gain affinity for such antigens [6, 7, 8, 109]. We then examine the effects of flexible affinity thresholds between infections, which becomes a necessary condition for rendering observations of Abs response to sequential influenza infections. The main effect of such flexibility is that, from a modeling perspective, it allows representing antigen-specific and broad responses which obey slight affinity changes in the variable and conserved areas of the antigen, in this case, hypothetically representing the influenza virus. On the basis of such affinity flexibility, we further explore the effects of the antigenic distance between the antigens of infection, as well as the effects of the time and order of infection. The modeling approach has desirable features for delving into, for instance, Abs response within H1 or H3 strains, which may need to solely define the new antigen. These characteristics render a platform that we expect can assist in understanding both natural influenza infection and vaccine design and efficacy, with the possibility of extension to other related respiratory antigens. For the last, the modeling approach could illustrate the SARS-CoV-2 spike protein characteristics to explore those antigenic structures that are targeted by neutralizing antibodies and exhibit mutation in response to the selective pressure of infection [112].

2.3 Influenza treatment

Along with vaccines, antiviral drugs are a key player in both the prevention and treatment of influenza virus infection and disease. For seasonal influenza, antivirals are mainly used for treating severely ill patients, particularly those with compromised immune system. In a pandemic scheme, antiviral drugs are essential for both treating infected patients and preventing infection in exposed individuals [1]. Currently, the World Health Organization (WHO) and the Food and Drug Administration (FDA) recommend the use of NA inhibitors (NIs) as the first-line treatment.

2.3.1 General view of antiviral drugs for influenza

Before 2004, the adamantane derivatives rimantadine and amantadine were drugs licensed for influenza treatment, however, from the 2004–2005 influenza season on, the use of adamantane derivatives was no longer recommended due to the emergence of resistance in most circulating influenza strains [113].

Definition 2.15. *Neuraminidase inhibitors. A type of antiviral drug that disrupts the release of influenza virions from the host cell by mimicking the neuraminidase sialic acid binding site. NIs bind neuraminidase to the budding viruses, blocking their enzymatic activity.*

Oseltamivir, for instance, is an orally delivered NI prodrug, oseltamivir phosphate, which is afterward converted to its active carboxylate form in the liver. Zanamivir, on the other hand, is an inhaled NI powder, therefore, its administration route constantly limits the use in individuals with respiratory problems. A third NI drug is peramivir which is intravenously administered and plays an option for hospitalized patients [114, 115]. Study results report improved outcomes associated with NIs, including reduced risk of pneumonia and reduced mortality in hospitalized patients. Better results have been observed with early NIs administration, that is up to 2 days of symptom onset, later administration can still be beneficial in severe cases [59, 116]. Oseltamivir became the market leader due to its oral delivery being preferable over inhaled zanamivir. Nowadays, most of the developed countries primarily used NIs for the treatment of hospitalized or severely ill patients, however, the emergence of oseltamivir resistance is of particular concern for H1N1 viruses [4, 117]. Further drugs that target different stages of the influenza virus life cycle than NIs in human cells have been developed and tested, among these are baloxavir marboxil (BAM) and favipiravir (FP). BAM was licensed in Japan and the US in 2018, this drug inhibits the endonuclease of the viral polymerase complex of influenza A and B viruses. While this drug had similar effects on reducing symptom duration as those seen for oseltamivir, it had significantly greater effects on reducing viral replication and shedding. Similar to BAM, FP acts by reducing viral replication through inhibition of the RNA-dependent RNA polymerase of the virus [118, 119]. Further studies may focus on whether the enhanced reduction in viral replication will translate into reduced severity of disease in severely ill patients or if it may also reduce secondary transmission [120, 121].

Regarding other therapies, monoclonal antibodies (mAbs) against the conserved region of the HA are under clinical development for the treatment of severe influenza infection. Besides, many other mAbs candidates are in pre-clinical development which hopefully leads to improved options for influenza therapy in the future [122]. The treatment of hospitalized patients with immune plasma or with hyperimmune immunoglobulin, pooled from the plasma of donors with high anti-influenza mAbs titers, is also under clinical assessment [123]. In this direction, future influenza therapies may involve a cocktail of drugs/therapies combining different targeting mechanisms that should contribute to weakening drug resistance [124].

2.3.2 Optimizing influenza therapies

The treatment schedule of NIs, as recommended by FDA and WHO, usually consist of a fixed-dose administered once or twice per day for a period of time [1, 61]. However, the seek for better medication strategies is an unceasing task that leads to a constant exploration of novel alternatives in drug development at diverse levels such as mechanisms of drug delivery and response, treatment scheduling optimization, and medication personalization. In this sense, the combination of different knowledge areas such as pharmacology, systems biology and control theory, can guide the path into influenza treatment progress.

Regarding pharmacology, pharmacokinetic (PK) and pharmacodynamic (PD) modeling and simulation - the PK/PD approach - has been extensively used in pharmaceutical companies and research groups that develop and apply mathematical and statistical methods to characterize, understand and predict a drug's behavior [34]. Towards similar directions, Systems biology (SB) provides system-level insights to understand interactions and dynamics at various scales, within cells, tissues, organs, and organisms through mathematical and computational models. In recent years, modeling of host viral infections such as influenza has risen as a promising tool to quantify infection levels as well as to identify potential therapeutic targets for disease control [49]. Also recently, SB and pharmacology models -coupled as Systems Pharmacology- have guided research in precision medicine for complex diseases [125]. Lastly, control theory (Definition 2.16) has resulted in widespread adoption of closed-loop (feedback) control in systems biology due to improvements in computing, actuation, and characterization of drug's PK/PD properties, all using mathematical modeling platforms.

Definition 2.16. *Control theory. A discipline whose objective deals with developing models and algorithms governing the application of inputs to a dynamical system to drive it to the desired state ensuring a level of control stability, often to achieve a degree of optimality.*

Closed-loop drug estimation systems enable optimal scheduling of drug administration by leveraging classic and modern control-relevant models, systems pharmacology, and decision-making, based on clinical targets [25]. Hence, influenza treatment scheduling is to be considered a control-based optimization duty, whose outcomes may guide the tailoring of treatment, in a framework of dose estimation. In this sense, the interactions between the virus, the immune response, infected and susceptible cells, and the drug's PK/PD dynamics, which may vary from one patient to another, are studied as a dynamical system to be analysed by optimal control-based methods which also incorporate clinical requirements [64, 126]. In this sense, dose tailoring in the treatment scheduling framework can be estimated depending on the evolution of each patient infection - a personalized scheme [64, 25, 126]. Figure 2.5 depicts the structure of the control-based treatment tailoring, developed in Chapter 4. The first block of mathematical models describes biological phenomena such as infectious diseases, characterizing the viral and host dynamics, which also outline a clinical response. The second block, the dose tailoring system, computes the drug dose based on the viral, host, and drug responses. A closed-loop scheme is then formed adding a third block, the PK/PD models, standing for drug dynamics. Of note, since the control strategies perform based on the drug's PK/PD models, the complete approach can be also identified as a PK/PD-based control scheme [127].

Control-based schemes have been extensively used in a variety of biomedical applications that extend from the study of optimal cellular resources [128], medication infusion [129], circadian phases control [130], diabetes treatment [131], and infectious diseases such as HIV [132, 133], and influenza [65, 126, 127]. In addition, learning-based methods have boosted the development of control schemes. Recurrent neural networks (RNN), for instance, have been used as universal approximators that ultimately improve control systems due to their flexible design and the incorporation of prior information of the system structure into the RNN, making a piece of suitable machinery for real-time implementations [134, 135, 38]. Combining neural networks' approximation with control-based methods, the so-called

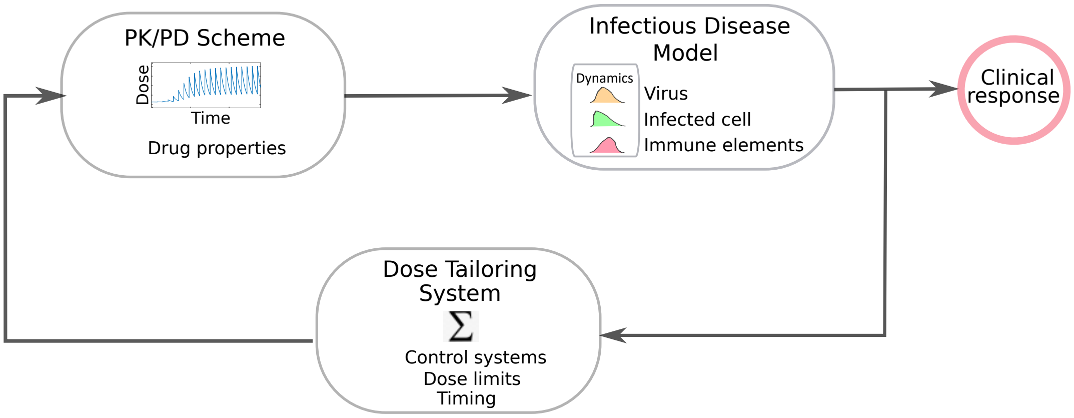

Figure 2.5: Control-based drug tailoring framework. The influenza dynamics, accounting for viral and host response, are represented by a mathematical model that also reflects a clinical response. The dose tailoring system calculates the drug dose on the basis of influenza dynamics and drug properties, which are taken from a PK/PD model. This scheme forms a closed-loop system for automatically tailoring drug doses at a personal level.

neurocontrol structure is conceived in Chapter 5, which eliminates uncertainties in model parameters, provides robustness, and allows overcoming real-world affairs, such as data scarcity or measurement limitations [37, 43]. All these schemes are subject to a strong mathematical background that attempt to ensure different control aspects, such as stability and optimality, accounting for specifications to meet clinical demands.

Taking all together, we devise control-based influenza treatment scheduling frameworks using influenza host models and PK/PD dynamics of NIs [64, 65], accounting for dose boundaries [127, 136], and learning-based methods for clinical limitations, such as scarcity of viral measurements [37]. We challenge the mechanisms at a population level through Monte Carlo simulations in a form of virtual clinical trials, where the treatment dose has been tailored to the virtual-host personal infection evolution. Hence, control-based treatment scheduling optimization shows to serve as a tool for developing novel treatments strategies, testing antiviral activity, exploring the host response variability and viral properties. We expect these types of virtual experiments can guide and inform systems of infectious diseases and pharmacology.

Chapter 3

Antibody cross-reaction in sequential infections – a modeling approach

Sequential infections with related influenza strains, two infections with different strains of a subtype, have been uncovered to confer enhanced breadth and magnitude of antibodies (Abs) response, particularly after the second infection – a cross-reactome scheme observed in experimental studies in animal models and in humans. Considering previous modeling strategies on the theoretical representation of influenza strains (antigens) and B-cells with variable and conserved areas, together with affinity maturation processes, we explore how and to what extent antibody-antigen affinity flexibility could guide the cross-reactome in sequential infections for a hypothetical family of antigens. We delve into diverse scenarios of affinity thresholds in the conserved and variable areas of the antigens and analyse the characteristics that may lead to enhanced breadth and magnitude of responses for the first and second infections using slightly different antigens. While the Abs response reached a high magnitude when using equivalent affinity thresholds in the conserved and variable areas during the first infection, improved cross-reactome was developed when slightly increasing the variable threshold for the second infection. Such an outcome could correlate with observations in theoretical and experimental settings and may be attached to reaching specific mutations for getting affinity to a newly presented antigen while broadly reaching related antigens. The scheme herein developed may serve as a proof of concept platform for exploring fundamental mechanisms that favour the Abs cross-reaction. *This chapter extends in a didactic manner the partial content of Ref. [111]*[1].

3.1 Introduction

3.1.1 Antibody cross-reaction outcomes in sequential infections

In the last decade, sequential infections with complex pathogens such as the influenza virus have been uncovered to render a particular behaviour regarding the antibodies (Abs) cross-

---

[1] Partial reprint from Ref [111], Gustavo Hernandez-Mejia and Esteban A Hernandez-Vargas, Uncovering antibody cross-reaction dynamics in influenza A infections, Bioinformatics, Volume 37, Issue 2, January 2021, Pages 229–235, by permission of Oxford University Press. Permissions apply to Figure 3.2, Figure 3.3, and Figure A.1.

reaction. The Abs responses reach a diversity of strains, going from the proper strains of infection to slightly different ones and even reaching novel strains, this is the case of the Abs response reaching 2009 H1N1 strains under sequential infections of previous seasonal strains [137]. Characterized by a high breadth and magnitude of response, experiments with different animal models (mice, ferrets, and guinea pigs) have challenged the Abs cross-reaction following sequential infections with divergent influenza strains from group 1 HAs (H1) and group 2 HAs (H3). In such a framework, Abs responses not only reaches the strains of the infection subtype (H3 or H1) but also develops heterosubtypic responses, an outcome enhanced after the second infection [5]. Similar cross-reactivity behaviour has been encountered in the human repertoire of memory B-cells, with abundant cells for both influenza strain groups [107]. In addition, the reaction among strain subtypes (diverse H1, H2, or H3 strains) has been found to vary in magnitude independently of strain differences for various influenza subtypes [138], a framework presumed to follow B-cell responses towards the conserved stem region of the HA [139], and that has also been hypothesized as a core mechanism when exploring Abs response differences between sequential infection and sequential vaccination, both providing cross-protection although in different magnitude levels [140].

The mechanisms governing such behaviour are still to be better understood and both, experimental and theoretical schemes are demanded. A possible framework is under the mechanisms that describe the preference of the immune system for a certain target epitope over other targets –immunodominance. Usually, after one infection with a specific influenza strain, Abs against the HA head domain are induced at a higher magnitude than those against the stalk domain. It is considered that the restricted accessibility of the membrane-proximal HA stalk domain to membrane-bound B-cell receptors potentially drives such behaviour [95]. However, the Abs response after the second sequential infection with a related strain of the same influenza subtype can become of higher hierarchy towards HA stalk, a phenomenon involving a great number of puzzle pieces to be connected. One of the existing models suggests that HA stalk-specific B-cells seed the pool following primary infection and they are efficiently recruited into recall responses compared to those of novel HA, where competition with HA globular head-specific B-cells is minimized [141]. Further studies support the view that Abs directed at the conserved HA stalk confer protection and such specificities are boosted following encounters with antigenically distinct but related HA proteins [142]. In this sense, regarding sequential infections, the Abs responses generating breadth and magnitude to divergent influenza subtypes points to become a common outcome, with broadly reactive Abs targeting the conserved HA region [143]. Similar phenomena have been uncovered in other complex antigens such as in the HIV envelope, where avoiding interactions with some residues can allow better access and more powerful interactions with the conserved residues of the epitope, following specific mutations for broad reactions [24]. The last may indicate a possible redirection of the Abs response following alterations of affinity in the variable regions which could be driven by the encounter of novel antigen regions that, in turn, would demand extra efforts for reaching the same affinity level as the first encounters.

3.1.2 Antibody cross-reaction – modeling background

Several theoretical models have been proposed to give insights into the players in Abs response to infection [108], most of them use agent-based models to incorporate antigen and

Abs properties as well as different dynamic settings to describe the breadth and magnitude of Abs response. Binding models and germinal center reaction models, for instance, are designed to focus on specific aspects of binding sites or germinal centers' internal properties. For in-depth reviews, see Ref. [108] for binding models and Ref. [144] for germinal centers.

Considering the differences among antigens as the potential breadth of Abs response, and the affinity level related to the magnitude of response for each of the antigens, diverse schemes generally incorporate antibody-epitope binding affinities. The use of abstract multidimensional grids is, for instance, a framework where antigens and Abs are represented as points in the grid and affinity is based on the summed distance in each dimension. This mapping scheme is generally known as the *shape-space*, a pioneering framework in theoretical immunology for representing the breadth of Abs response developed by Perelson *et al.* in 1979 [20]. Two decades later, modeling extensions were applied for integrating breadth and magnitude. Developed by Smith *et al.* [6], the antigenic distance scheme considers gradual differences between strings of digits representing the facing residues of antigens and Abs, and provides metrics for the Abs cross-reaction. The strings represent general structures of antigens and Abs, with no classification into variable or conserved portions of the strings. In the last, differences among antigens and levels in binding affinity are measured using the Hamming distance between binary strings (Definition 3.7). Under such a scheme, the Abs response for infection or vaccination is explored considering that the higher response in magnitude correlates with the less antigenic difference and the breadth of response is limited to close related antigens [6, 145]. Regarding the dimensionality of the *shape-space*, for the case of influenza, theoretical studies stand for the characterization of the space integrating data from affinity assays, such as the hemagglutination inhibition (HI) assay, using two-dimensional spaces, which gave rise to the antigenic cartography (Definition 3.1) [21, 22].

Definition 3.1. *Antigenic Cartography. Refers to the process of creating maps, such as two-dimensional representations, of antigenically variable pathogens to represent the antigenic or genetic differences among them. The maps allow monitoring the variability among vaccines and circulating strains and thus estimating the effects of vaccination [22].*

Regarding binding interface (Definition 3.2), models have explored binary representations (strings of binary digits) where antibodies and antigens are represented as facing residues. Matching residues with the same binary digits attract each other indicating higher affinity and opposite ones make to decrease in affinity. Mutations (point-mutations, Definition 3.3) are given by changing digits in random positions making the overall binding affinity increase or minimize due to the facing residues in the string. Key mutations (Definition 3.4) can be theoretically integrated by featuring a binding common space of consecutive digits, this technique has been explored by Khailaie *et al.* [110] to represent the T-cells binding interface, where the contribution of the largest common space match to the affinity is ponderated according to the position of the digit in the binding interface. Further models suggest that the affinity can be guided by the maximum number of interacting residues, the longest common substring (LCS) of both sequences, where the total affinity is the global sum of affinities of the conserved and variable sections [7].

Definition 3.2. *Antibody-antigen binding interface. Binding relies on the specific interaction of amino acids at the paratope-epitope interface. A paratope, also known as an antigen-*

binding site, is the part of an antibody that recognizes and binds to an antigen. On the other hand, an epitope is the part of an antigen that is recognized by Abs, B-cells, or T-cells [146].

Definition 3.3. *Point-mutation. Also known as substitution, is a genetic mutation where a single nucleotide base is changed, inserted, or deleted from a DNA or RNA sequence of a genome. These changes can range from having detrimental, favorable, or minor effects on certain functionality [146]. This process, therefore, leads to different effects of point-mutations, where some of them have negligible effects but others lead to key affinity changes – key mutations (Definition 3.4).*

Definition 3.4. *Key mutations. Point-mutations that can provide an increase/decrease in the affinity of B-cells in substantial manners.*

In this direction, key mutations can be also designed for antibody accessibility with a level of the requested change in affinity accounting for a predefined distribution of mutation affinity changes. This technique considers variable and conserved areas where mutations can affect affinity and has been used to question cross-reactivity in HIV [8]. In such a scheme, B-cell receptors that decrease contacts with variable residues are more likely to be able to access and make contacts with the protected conserved residues, a framework theoretically and experimentally tested under sequential HIV (HIV envelope structure) infections [8]. In addition, modeling studies suggest that breadth could benefit from a less diverse B-cell seed since it may favour the expansion and dominance of cross-reactive clones when conflicting selection forces are presented in sequential setting [147]. Finally, further studies have explored the diverse population dynamics of the B-cells, plasma cells and Abs developing schemes not only incorporating the affinity maturation (AM) process but also accounting for the evolving dynamics that lead a B-cell to generate Abs [109].

Herein, we detail and extend diverse modeling frameworks regarding the theoretical representation of antigens and B-cells as well as the affinity maturation processes to explore how binding characteristics guided by affinity thresholds may drive the Abs cross-reaction. We focus on the Abs outcome to a first and a second infection presented sequentially using slightly different hypothetical antigens. The model framework may generally represent the Abs cross-reaction to sequential infections with influenza strains of the same subtype. The proposed platform may serve as a basis for testing not only the binding affinity characteristics but also for exploring diverse strategies of sequential infections, such as the order and time between infections for different antigens, and the role of key mutations that may lead to promote breadth.

3.2 Stochastic mathematical modeling framework

We first focus on illustrating the observed cross-reactome behaviour in sequential infections with divergent influenza strains. Figure 3.1 depicts a cartoon of the Abs response phenomena for single (panel A) and sequential (panel B) infections with four antigens symbolised with the letters A, B, C, and D that would represent a family of influenza strains of a certain subtype. The antigenic difference between these antigens with respect to antigen-A is portrayed by W for each of them and the magnitude of Abs response is represented by M for each antigen. For the ease of appreciation, the antigenic difference with respect to antigen-A is depicted in the centre of Figure 3.1 with $\mathrm{W_B}$, $\mathrm{W_C}$, and $\mathrm{W_D}$. The magnitude of each infection scheme is also depicted at the bottom of the cartoon for a better appreciation. The Abs originally produced after a single infection with antigen-A can reach the other antigens, where the level of magnitude could be related to the level of difference concerning antigen-A, depicted in Figure 3.1-A. Also, the higher magnitude of response is usually developed towards the antigen of infection, antigen-A. On the other hand, the Abs response after sequential infections in Figure 3.1-B may independently develop from the level of difference with respect to antigen-A. In this case, antigens-B to -D would develop a higher magnitude of response, closely reaching that of antigen-A. Thus, the Abs cross-reaction after sequential infections reaches greater breadth and magnitude for all of the related antigens, as observed in experimental settings [5]. In a similar direction, Fonville *et al.* [148] showed that for similar antigenic distances, diverse levels of Abs responses can be observed during infection and vaccination in a family of strains of the H3 influenza subtype, mapping and visualizing the breadth and magnitude through Abs landscapes (Definition 3.6). We, therefore, integrate diverse schemes to represent the Abs cross-reaction in sequential infections for influenza strains. In this section, we present the followed strategies for the representation of the antigenic space dimension, the antigen representation through strings of characters containing variable and conserved proportions, and the distance between the antigens of infection. Binding affinity is integrated featuring affinity threshold for the variable and conserved proportions, we explore cases that might lead to breadth and magnitude of Abs response in sequential infections.

3.2.1 Antibody-antigen binding interaction properties

Space dimensionality. Diverse studies have been developed to derive shape space parameters consistent with immunological data, mainly using HI assays, giving raise to a two-dimensional antigenic space for the case of influenza [145, 22]. Pioneering studies suggest that spaces above five dimensions would fairly represent the antigenic space, accounting for the desired method of antigen representation, as a point in the space (Euclidean space), which may lead to even higher dimension, or as a sequence of digits, with up to eight dimensions [145]. Further studies stand for a reduction of the dimensionality of the antigenic space, using ordinal multidimensional scaling (oMDS) techniques (Definition 3.5), where antigenic space could reduce to reach a five-dimensional scheme while still integrating data from immunological assays. One of the main outcomes of the space model is the observation that antigenic distance is linearly related to the logarithm of the HI measurement. Based in such observation, modifications of the metric MDS (mMDS) were used to position the antigens in a two-dimensional space [22].

Definition 3.5. *Multidimensional scaling (MDS). A set of algorithms that reconstruct the true dimension of a space, and the relative coordinates of points, given only distances, or more generally monotonic transformations of distances between the points [21]. There are two classes of MDS schemes, ordinal MDS, for which the rank order of distances are given as input, and metric MDS, in which distances between points are given as input [149, 150].*

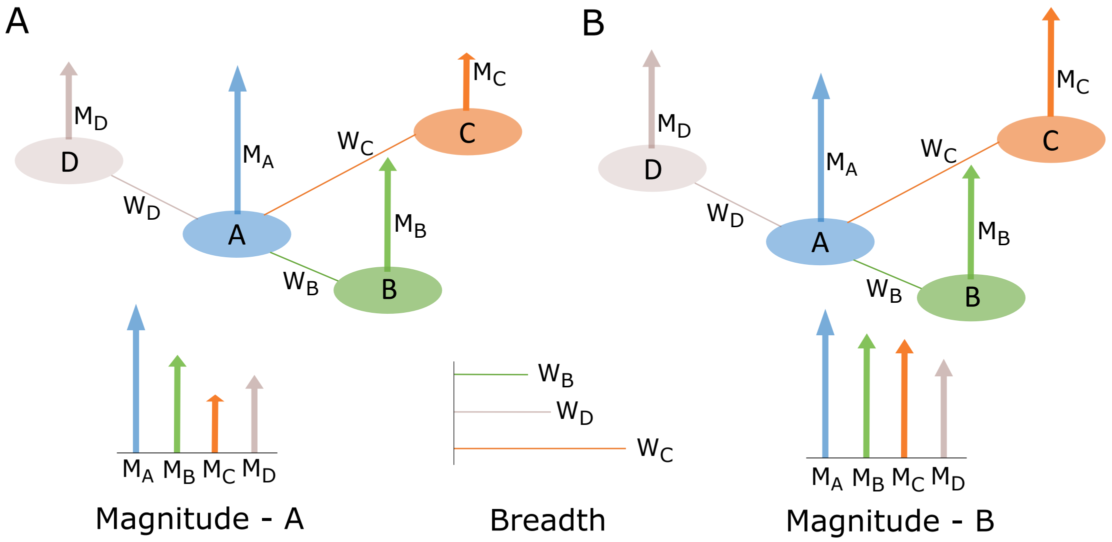

Figure 3.1: Cartoon of the breadth and magnitude of Abs responses for single (panel A) and sequential infections (panel B). Four antigens are represented with the letters A, B, C, and D. The antigenic distance between each antigen with respect to antigen-A, the antigen of infection, is represented by W for each of the antigens (breadth), and the magnitude of Abs response is rendered by M. After a single infection, panel A illustrates that the breadth and magnitude of response may be related to the level of difference with respect to antigen-A; more distanced antigens, such as antigen-C, may develop a rather low magnitude of response. However, the Abs response to a second (sequential) infection (panel B) may not only reach close antigens (B and D) but also reach the antigen-C, for which the magnitude could also be as high as close antigens, such as antigen-B. Such a cross-reactome behaviour has been observed in experimental studies [5, 107].

Definition 3.6. *Antibody landscape. A method for the quantitative analysis of antibody-mediated immunity to antigenically variable pathogens, achieved by accounting for antigenic variation among pathogen strains. The antibody landscape is mounted on a two-dimensional antigenic map [148].*

In this direction, for the development of the antigenic space, the prediction error between predicted and measured HI values decreased only slightly as the number of dimensions increased from two to five, indicating that distortion due to compression from higher dimensions to two dimensions is acceptably small and that a two-dimensional antigenic space is a fair characterization of influenza HI data sets. It is, however, expected that higher dimensional antigenic spaces will be required for other pathogens, potentially corresponding to the specific phylodynamics [22, 151] For further information regarding the methodology for deriving antigenic spaces (maps), please refer to Smith *et al.* [22], especially to the supplementary documents. In this sense, we use of an antigenic two-dimensional space since, as presented above, this is based on methods that focus on the representation of influenza virus immunological assays. Further schemes have usually followed a two-dimensional space for rendering the Abs affinity to specific antigenic sites of influenza virus [152] and to explore the levels of Abs responses for different antigenic distances within H3 influenza strains using Abs landscapes (Definition 3.6) [148].

Antigens and Abs representation through strings of characters. Theoretical models have explored different representations of antigen proteins for diverse phenomena including the antibody-antigen affinity. One of the main methods for representing antigens and Abs is through sequences of symbols –strings of different digits. The last has been generally used to represent both molecules and gene segments where the patterns of the strings represent the shapes of molecules and determine their ability to bind other molecules [153, 154]. The sequences of symbols can be loosely interpreted as peptides and the different symbols as properties of the amino acids such as classes of similar charge or hydrophobicity [145]. The mapping between sequence and shape is to be further explored, it's been typically related to specific phenomena or antigen characteristics under investigation, usually assuming the string sequence to be equivalent to antigen shape [6, 145].

Alphabet space – number of possible symbols. Strings of four different symbols have been used, for instance, to render antigenic differences for testing the efficacy of vaccines for diverse influenza strains, where efficacy is related to the Hamming distance (Definition 3.7) between strains [6]. A second example using strings of four symbols was used for testing the cross-reaction of a polyvalent malaria vaccine. Also using Hamming distance to measure differences between antigens, this study introduces a general representation of a conserved epitope, which had a defined antigenic distance of zero between all serotypes, and a polymorphic epitope, which had a predefined antigenic distance (Hamming) of four between each serotype [109]. In the last, the level of cross-reaction would be rather related to the distance between the polymorphic epitope, which has rather predefined immunogenicity. On the other hand, examples using strings of binary digits have been explored as procedures for representing immunological data into the digits space [145], and pioneering approaches for the testing of affinity and binding interactions of antigens and Abs [155]. Additionally, binary representations stand for T-cell affinity models [110], and the manipulation of selection forces, bit position in the string and mutation in a variable or conserved area, explored for antibody response in the HIV infection [8, 110]. Moreover, using binary representations is consistent with studies suggesting the use of alphabets of up to four different symbols with string lengths of mid to low twenties for representing cross-reaction setting in influenza infection [145]. In this sense, we integrate the use of binary strings for representing the antigens of infection. This selection seeks a simpler representation of antigens and, as presented above, follows the overall settings from previous theoretical studies [145, 155], and extended experimental explorations in sequential infections [8, 147].

Definition 3.7. *Hamming distance. A metric used for quantifying the extent to which two bitstrings of the same size differ by checking if the corresponding bits in two strings' positions agree [156].*

Distance metric and length of strings. The Hamming distance sets a metric for measuring the antigenic difference between hypothetical antigens represented by strings of symbols. The Hamming distance has been considered as the antigenic distance metric in most studies dealing with Abs cross-reaction to complex antigens, such as influenza [6, 109, 157]. There are, however, slight differences when rendering the Abs cross-reaction. Previous studies set the breadth level to a predefined level of antigenic distance (cutoff), this typically results in limited cross-reaction to those antigens with higher antigenic distance (for instance over five to seven) [6, 109, 152]. However, as experimental studies suggest that Abs breadth can actually reach more distanced antigens, from reacting to the complete subtype of influenza strains to reaching heterosubtypic responses, we use the Hamming metric solely for the antigenic distance regardless of a predefined breadth. Such a scheme has been lately explored for rendering Abs cross-reaction, where the Abs breath rather follows the affinity for antigens [7, 8, 147]. While the Hamming distance provides metrics for the antigenic difference that rather relates to the sequence of the antigen, the affinity of Abs for different antigens may be related to structural settings. As antigens could be close in space if the sequence is similar, the fitness of Abs response could vary as the binding structure changes from each antigen. In this sense, the model considers the Abs cross-reaction to follow the affinity for each antigen, given by the matching score of B-cells for antigens and the general fitness.

Regarding the size of the strings, it has been found that a length between six and up to 24 digits, depending on the purpose and characteristics of the antigens, could be used for their representation. Models representing a variable and a conserved area are mainly driven by two strings representing each of the areas [8, 7, 6, 109, 110]. Examples of shorter strings (up to 8 digits) for each of the antigen areas have been used when rendering specific theoretical schemes as the limited access to conserved areas [7]. In the case of HIV models, larger strings have been integrated to make contact with different types of residues, highly conserved (18 digits), residues representing motifs (6 digits), and variable residues (22 digits), summing 46 digits [8]. We integrate schemes for having specific strings for the conserved and variable areas that remain constant in length, relatively short size, and that allow representing mechanisms of the affinity maturation processes [7, 109, 110]. In this sense, antigens are formed by two strings of seven digits for the conserved and variable areas, respectively. This is applied for each of the space dimensions ($d1$ and $d2$ in (3.1)), generating the binding interface representation – Figure 3.2. This scheme remains consistent with the suggested representation of space parameters for the case of influenza [21, 145, 152]. Taking all together, Table 3.1 reports the family of hypothetical antigens represented by binary strings for the simulation experiments incorporating the aforementioned schemes. The antigen representation features conserved and variable substrings for each antigen, accounting for a two-dimensional setting, and the Hamming distance standing for the antigenic difference between antigens. The last is measured with respect to Antigen-A. Note that, in consistency with related studies, the conserved area remains practically constant to all of the antigens while the variable area can present major changes in the composition of the strings [8, 109, 152]. Finally, also consistent with previous studies, the Hamming distance can go from zero to over ten in total, regarding a strain reference (Antigen-A) [6, 157].

Binding affinity thresholds and fitness. Originally introduced as the concept of the longest common substring (LCS) between antibody and antigen, this stands for a threshold above which an antibody-antigen pair has a positive match score. The threshold is then related to the length of common substrings for the variable and conserved areas, very low match lengths meaning matches at just a few digit positions, which may become common, are not considered to be interactions between an antibody and antigen; they are too weak to generate any selective advantage [7]. In addition, regarding the effects of mutation in fitness, the longest common substring metrics allow that specific mutations, even of a single digit in a common substring, could lead to immune escape [7, 158], this means that large changes in matching length can also occur with a single mutation (Definition 3.3), a digit flip, if that mutation occurs in the middle of a common substring, standing for possible key mutations, see Definition 3.4. Such schemes are also consistent with experimental observations in binding structures [159, 110]. Thus, the LCS guide the binding strength for both of the areas of the antigen-antibody interface, where random mutations are free to occur in

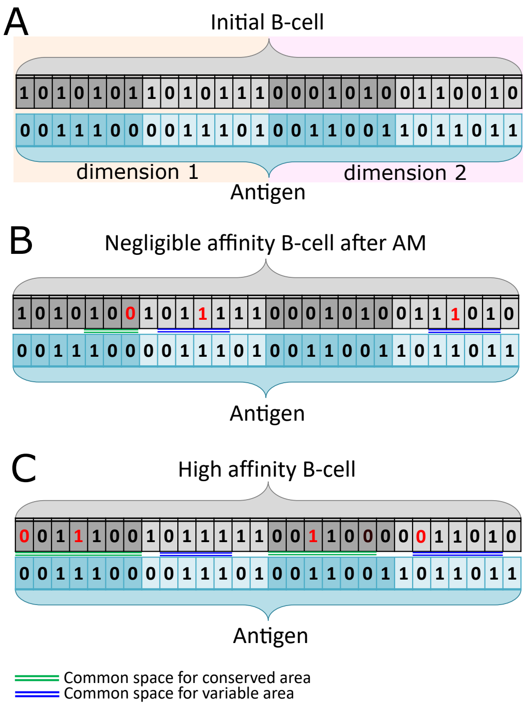

Figure 3.2: Mathematical model of the evolving affinity of B-cells for antigen. Antigens and B-cells are formed by two strings of fourteen binary characters. A binary string is formed by the conserved area, the darker one, and the variable area with a lighter color, each of seven digits. The affinity of a B-cell for antigen considers the common space in the conserved (green) and variable (blue) areas. An outstanding affinity considers the longest consecutive common bit-alignments between the antigen and B-cell. A) The naive B-cell population has a very low or no affinity for the antigen. B) Due to the affinity maturation process, a new set of slightly higher affinity B-cells arise, which establishes a new population threshold of affinity for the next generations of B-cells. Red characters result from several iterations of affinity maturation. C) As affinity maturation goes on, B-cells reach a high affinity for the antigen, characterized by longer common spaces of the conserved and variable areas. The complete scheme of the immune response model is depicted in Figure 3.3.

the variable and conserved sections. Subsection 3.2.2 provides details on the binding affinity schemes of the current model.

3.2.2 Fitness model and affinity maturation in germinal centers

In this subsection, we use schemes for representing diverse characteristics of the antibody-antigen binding interface together with central features such as the integration of a common longest substring for the variable or conserved areas, affinity thresholds and the affinity maturation process (Definition 3.8) through mutations in B-cells. As germinal centers (Definition 2.11) do not select for pathogen neutralization since antigenic epitopes are not presented in their functional setting, germinal centers' selection is only based on antibody-antigen affinity [16, 160]. In this direction, the proposed scheme aims to explore mechanisms of antibody generation that operate in both directions, high fitness for greater Abs magnitude to the given antigen and Abs diversity for a breadth reaction, reflecting the affinity maturation that B-cells undergo in germinal centers [7, 17, 161]. Figure 3.2 depicts an schematic of the affinity maturation process depicting the antigen and B-cell binding interface with the principal stages of the phenomena to investigate. A complete scheme of the proposed model involving the considered immune elements is depicted in Figure 3.3.

Definition 3.8. *Affinity maturation. This is the process whereby the immune system generates Abs of higher affinities as a response to antigen [162].*

Antigen - B-cell matching score and fitness. For each antigen and B-cell pair, the matching score indicates how strong the interaction is between them [7], it is determined by three indicators easily identified in Figure 3.2, separately applied for each dimension. The conserved matching area consists of the first seven darker-coloured string digits from left to right. The variable matching area is given by the seven leftover lighter-coloured digits, and the common space between strings is highlighted in green for common space in the conserved area and blue in the secondary matching area. The division of the matching areas is thought of as the physical structure of an antigen, such as the head and the stalk of influenza. While the stalk is conserved among and even between influenza A virus subtypes, the head domain varies more among strains [104]. Therefore, the first digits of the strings, the conserved matching area, are designed to remain mostly constant among antigens under a slight Hamming distance among them. On the other hand, the variability of the digits on the remaining structure of the strings, the variable matching area, are randomly accommodated for a rather variable-like proportion of the structure in the antigen. The matching score ($M(B_i, A_j)$) for an antigen (A_j) and B-cell (B_i) pair is given as follows

$$M(B_i, A_j) = L_{C_{d1}} + L_{V_{d1}} + L_{C_{d2}} + L_{V_{d2}} \tag{3.1}$$

where L_C is the longest common space (consecutive bit-alignments) of the conserved area of any of the dimensions. Similarly, L_V stands for the longest common space in the variable area of any of the dimensions, separately, as depicted in Figure 3.2–B,C. L_C and L_V feature the following restriction

$$L_C = \begin{cases} L_C & if \quad L_C > \beta \\ 0 & otherwise \end{cases} \tag{3.2}$$

$$L_V = \begin{cases} L_V & if \quad L_V > \alpha \\ \gamma & otherwise \end{cases} \tag{3.3}$$

where α and β are the thresholds above which an antigen and B-cell pair have a favorable match score in the secondary and principal matching areas, respectively. γ is a parameter that contributes to the repertoire diversity, avoiding strain-specific behavior, especially during the first germinal center cycles. The fitness of a B-cell for antigen ($F(B_i)$) is exponentially influenced by the matching score of a B-cell accounting for the number of antigens per infection (N_A) in the following form

$$F(B_i) = e^{\frac{1}{N_A} \sum_j M(B_i, A_j)}. \tag{3.4}$$

The fitness of a B-cell is exponentially higher if its match score against all viruses is high and, assuming a relation of B-cells fitness with Abs production, those B-cells that recognize an abundant virus in the germinal center are more likely to continue in the system [17]. That is, the exponential framework for the fitness is based on previous studies suggesting that B-cell receptors do not interact with peptide chains in a linear fashion and that in the germinal centers, where affinity maturation occurs, viral particles are outspread on follicular dendritic cells in proportion to their abundance in the host. Therefore, Abs recognizing an abundant antigen will receive a survival signal, leaving the germinal center and continue circulating in the system [8, 7, 17]

3.2.3 B-cell proliferation, maturation and death

An essential characteristic of germinal centers reaction is dynamic behavior. Germinal center B-cells constantly migrate between microanatomical compartments as they undergo iterative

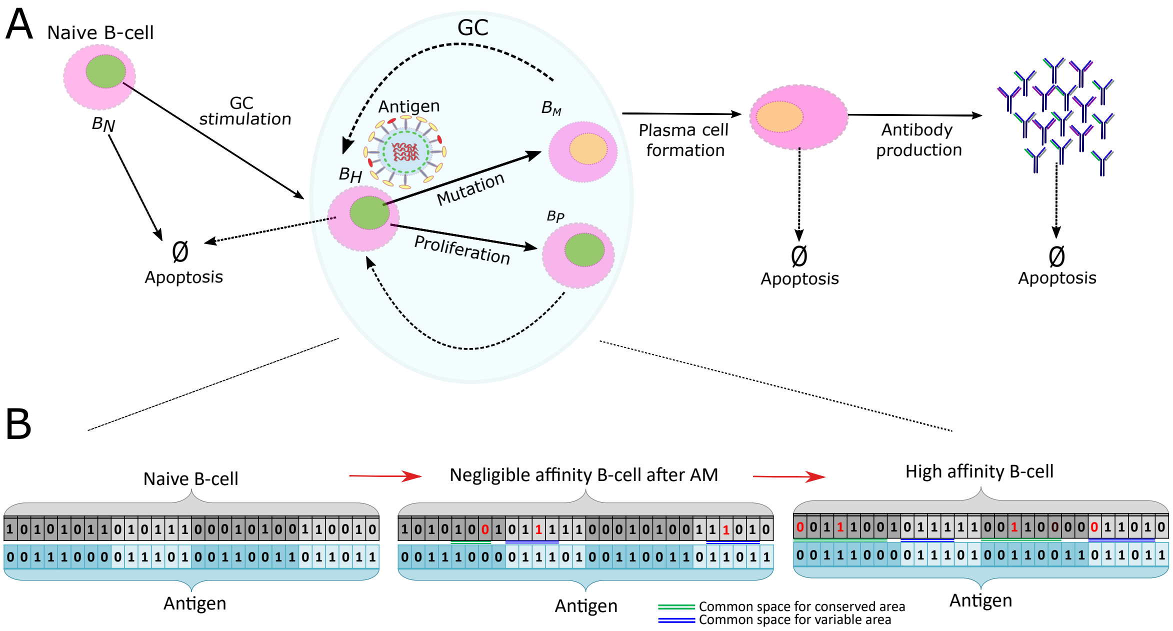

Figure 3.3: Schematic of the *in-silico* immune system stochastic model. A) The principal immune components of the model following the stimulation of naive B-cells (B_N), the affinity maturation process to increase fitness, and the production of plasma cells and Abs. Importantly, each element in the model represents a complete population and, in the case of plasma cells and Abs, the diversity of clones in the population. Dashed arrows in the germinal center (GC) oval stand for the several cycles of mutation and proliferation to reach affinity for the antigen. High-affinity B-cells (B_H) produce two cell populations, one of the same characteristics of high-affinity B-cell, identified as the proliferation of B-cells (B_P), and the second one, the mutated B-cells (B_M) which undergo affinity maturation (AM). B) The principal stages of the affinity maturation process, corresponding to Figure 3.2. A flow diagram of the Abs cross-reaction model is depicted in Figure 3.4.

cycles of somatic hypermutation and selection, seeking to obtain the signals required for their survival. In the model, selection and the relative fitness-based expansion and contraction of clonal populations follow dynamic rules based on a threshold given by the average fitness of the B-cell population [163]. A flow diagram of the Abs cross-reaction model accounting for the B-cells, plasma cells and Abs dynamics, as well as for the main features for the sequential infection setting, is depicted in Figure 3.4. Those B-cells above the fitness threshold, the high-affinity B-cells, are considered to produce two populations of equal size, as depicted in Figure 3.3–A. The first subpopulation conserve the same characteristics of the high-affinity B-cell, and the second one, the mutated B-cells, undergo affinity maturation. This generative process is considered as the proliferation of B-cells. For each daughter and mutated B-cell produced, a B-cell is uniformly selected at random to die regardless of its fitness, allowing a constant B-cells population [7]. In the model, the population of B-cells after the first infection remains unaltered in its average affinity characteristics, and this will start to change again when the second antigen of the sequential infections appears. The use of the B-cell seed characteristics after the first infection follows schemes indicating that a less diverse B-cell seed may favor the expansion and dominance of cross-reactive clones, but only when conflicting selection forces are presented in series (sequence) [147].

Affinity maturation and mutation of B-cells. The affinity maturation process allows B-cells to modify their string structure to gradually gain affinity for the antigen [8, 7]. During the affinity maturation process in the model, a digit of each B-cell string of the mutated B-cell population, is uniformly randomly selected to undergo a binary flip, this process occurs once per germinal center cycle [7]. Binary changes, seen as point mutations, can make a B-cell increase the common space of any, the conserved or variable matching area, to gain fitness. Since the binary changes are done at random positions, the risk of reducing the matching score of a B-cell due to affinity maturation is latent. Thus, affinity maturation is widely responsible for higher or lower matching scores and fitness. In Figure 3.2 the affinity maturation process is highlighted with red binary digits representing mutations over several germinal center cycles coming from a naive B-cell to a high-affinity B-cell. In Figure 3.2–B, there is not an effective matching score due to the short level of bit-alignments for dimension 1 and few common positions for the secondary, which is considered as a negligible matching score. However, note that after two mutations on dimension 1, a key mutation, Figure 3.2–C shows the complete bit-alignments of the conserved matching, forming a high-affinity B-cell.

Key mutations. This type of mutations regards for those in the middle of the largest common substring. In general, a string of size N having a mutation just in the middle will result in N/2 interacting digits. This is applied to both, the variable and conserved areas and follows the random mutations in the germinal center cycles. In this sense, not all of the mutations are the same for contributing to the matching strength. For instance, Figure 3.2–C shows a mutation in the conserved area (dimension 1) at the left-most digit – an extreme of the string, which will contribute (or neglect) the matching score by only one digit, regardless of the length of the common space substring for the conserved area. Analysis of empirical data has indicated that few mutations can confer (or limit) immune escape [158]. An illustration of binding gaining is found in Figure 3.2–C, where a single mutation in the conserved area (dimension 1) in the very middle of the string will stand for six matching digits for the binding interface, already setting a high-affinity B-cell. These schemes are analogous to the impact of Abs mutations on its binding with an antigen [7]. Thus, key mutations will be needed for guiding the Abs towards a new antigen after a first encounter, however, mutations continue to be at random positions, therefore, catching the specific position becomes highly difficult. A slight increase in the affinity threshold can demand such a mutation, therefore, we explore how the Abs outcome behaves for different affinity thresholds. As the threshold demands key mutations, that might not appear, but high affinity continues in the conserved area, these Abs remain to increase in population and will cross-react with diverse antigens.

3.2.4 Plasma cells and antibodies production

The dynamics of plasma cell and Abs production follows the schemes of Chaudhury *et al.* [109]. Each high-affinity B-cell has a 50% probability of differentiating into a plasma cell, the set of plasma cells, the plasma cell population, decays according to its half-life in a discrete fashion, that is, for every germinal center cycle, a proportion of the initial plasma cell population is eliminated based on a death probability, forming the plasma cell dynamics shown Figure 3.9–C. This approach considers the tau-leaping methodology (Definition 3.9) [164]. This means that given the half-life of a population and time-step size for the decay (hours, days, etc.), a probability of an individual to be selected and remain in the population

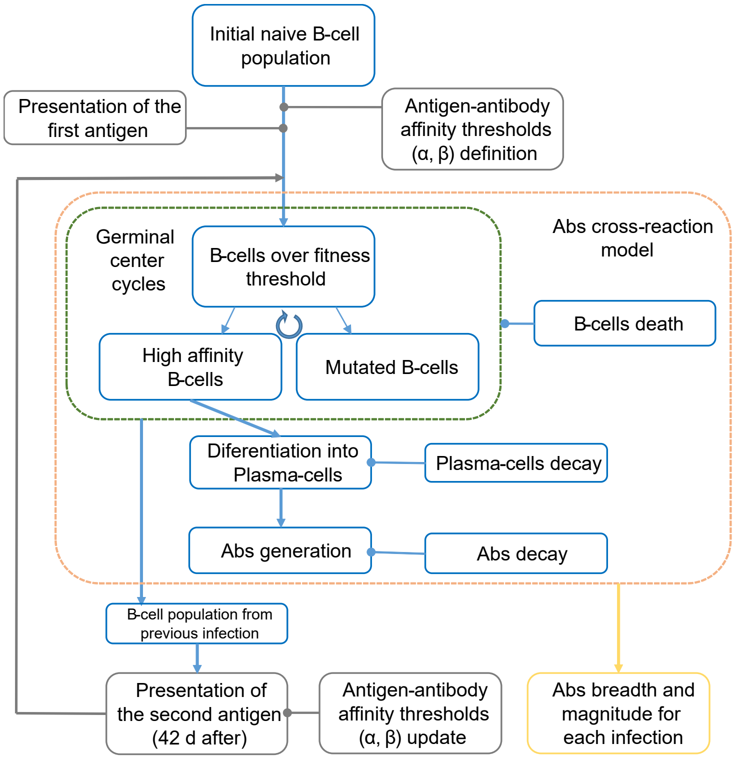

Figure 3.4: Flow diagram of the Abs cross-reaction model to sequential infections. The Abs cross-reaction model, the dashed orange rounded rectangle, incorporates the dynamics in populations of B-cells, plasma cells and Abs, accounting for decay/death processes of each cell population, and the internal features of the germinal center, the dashed green rounded rectangle. Initially, naive B-cells encounter the first antigen of infection, for which a very first B-cell population fitness threshold is established together with the antigen-Abs affinity thresholds (α, β). Higher affinity B-cells will be produced via affinity maturation on the germinal center cycles which will produce plasma cells and Abs. The Abs cross-reactome (yellow rounded rectangle) is registered via the distinct antigens the Abs can reach (breadth) and quantity of them (magnitude). Finally, for the second antigen encounter (antigen encounters are in grey color), antigen-Abs affinity thresholds are updated and the process continues again for the germinal center cycles, accounting for the B-cell population that resulted from the first infection.

is generated. The time-step can be selected as a resolution parameter, the smaller time-step the higher resolution of decay. Similarly, the greater the initial population the better behavior of the discrete decay. For a computational tool, see Ref [165]. After a germinal center cycle, the newly produced plasma cells are added to the remaining population of previous cycles, following the flow indicated by the arrows in Figure 3.3–A, after the germinal center cycle. Antibodies are produced as copies of plasma cells, their population rise and decay following discrete events on every germinal center according to its half-life. In the modeling schemes, Abs eliciting is a result of B-cells affinity for antigen, the probabilistic nature of B-cells to become plasma cells, and the stochasticity involved in both processes. Besides, the schemes allow the early appearance of high-affinity Abs and a large number of plasma cells [166], as depicted in Figure 3.9–C,D.

Definition 3.9. *Tau-leaping (τ-leaping). This is an algorithm to increase the computational speed of the stochastic simulation algorithm, a method for numerically generating time tra-*

jectories of the system state populations. Instead of computing the time to every reaction, τ-leaping approximates the process and attempts to leap in time, executing a large number of reactions in a period τ. Here, this is used for estimating a population decay with a certain half-life [167].

Finally, regarding parameterization, the germinal center (GC) cycle (B-cell division time) is 6 h [17], the B-cell mutation rate is 10^{-2} /B-cell/GC cycle, meaning one mutation event every GC cycle, selection of B-cells also occurs once per GC cycle [7]. The plasma cell's (PC) half-life is 3 d [6], the antibody's half-life is 10 d [109, 168], and the antibody generation is 5 Abs/PC/GC cycle [6, 109]. This parameter adjusts the magnitude of Abs response but does not affect the breadth phenomena. The size of the B-cell population is 10 thousand cells, which remains fixed for the complete simulation time (84 d). In the model, the digits of binary strings of B-cells are generated uniformly at random, for the variable and conserved areas, and both dimensions. The B-cell repertoire is given by the binary string length of each dimension (L_d) as $2^{L_{d1}+L_{d2}} = 2^{28}$, $L_{d1} = L_{d2}$= 14. Regarding the antigen population, it consists of 10 elements (virions) whose binary strings have Hamming distance of up to 2 in the variable area (in both dimensions) with respect to the strings given in Table 3.1, for each antigen of infection. These remain fixed for the simulation time. The threshold values for the secondary and principal matching areas, α and β, respectively, serve as tuning parameters to control the breadth outcome, see Section 3.3 for further details. Results of each of the tested scenarios in Section 3.3 report the average outcome of ten simulations. This project was developed from scratch, coded in Python 3.8, and runs on the High-Performance Computing (HPC) cluster FUCHS-CSC from the Center for Scientific Computing (Frankfurt, Germany).

3.3 Numerical results

3.3.1 Exploring affinity thresholds for sequential infections

The competition between B-cell clones and mutated variants, which may regard a great number of structural rearrangements [169], is thought to guide the progressive loss of clonal diversity in the B-cell population [16]. The immune system must regulate the competition to balance diversity and affinity, translated into Abs breadth and magnitude. While a rigorous affinity regulation will fastly derive in average population affinity at the expense of diversity, a relaxed regulation will lead to high diversity, but affinity will slowly increase [17]. In the proposed model, the Abs cross-reaction is related to the threshold of the common space of the conserved and variable areas. Different threshold frameworks were tested for the conserved and variable areas to explore scenarios that better represent an affinity–diversity balance in sequential infections. We use a hypothetical scheme where cross-reaction among six different antigens is tested, namely antigens-A, -B, -C, -D, -E and -F. Using antigen-A for the first infection, the Hamming distance is measured with respect to it for the rest of the antigens. For instance, Antigen-B has a total Hamming distance of 3, the distance for each of the antigens is reported in Table 3.1 for both dimensions and the total distance.

***In-silico* infection protocol.** We establish protocol of sequential infections that consists of using antigen-A for the first infection, followed by antigen-D 42 days after the first infection. The complete testing time is 84 days. Regarding the selection of the antigen for

	Dimension 1		Dimension 2		Difference (Hamming)		
Antigens	Conserved	Variable	Conserved	Variable	Difference D1	Difference D2	Total
Antigen - A	0011100	0011101	0011001	1011011	-	-	-
Antigen - B	0011100	0001101	0011001	1011110	1	2	3
Antigen - C	0011100	0100101	0011001	1001111	3	2	5
Antigen - D	0011100	0110011	0011001	1011111	4	1	5
Antigen - E	0011100	0000010	0011001	1011010	5	1	6
Antigen - F	0011011	1111110	0011001	0111111	7	3	10

Table 3.1: Family of hypothetical antigens featuring the binary strings for the conserved and variable areas. The Hamming distance of each antigen is reported with respect to antigen-A for dimensions 1 and 2 of the theoretical shape-space. The total Hamming distance sums the difference in each dimension.

the second infection, it is generally intended to select an antigen whose difference ranges in the middle of the Hamming distances among antigens. In this case, antigens -C and -D have both a total hamming distance of five, however, antigen-D is selected since, with respect to antigen-A, it features a higher distance at least in one of the dimensions (1), while antigen-C has similar distances in both dimensions (Table 3.1). This protocol scheme is based on experimental settings for testing the Abs cross-reaction to a set of influenza strains [5]. In this sense, the antigen of a first infection is presented and B-cells will perform affinity maturation for gaining fitness, while antigens remain fixed. The same scheme is applied during the second infection.

We set different exploration cases, each with various scenarios for both affinity thresholds. Table 3.2 reports the tested cases with each scenario. While cases 1 and 4 have four test scenarios, cases 2 and 3 have three test scenarios. The values in Table 3.2 stand for the sequential (first | second) infections settings. Cases 1 and 2 explore a fixed threshold at the conserved area (β) while using different values for the variable threshold α, a fixed value in both infections (case 1) and with slight threshold changes (case 2). On the other hand, cases 3 and 4 explore the conserved area threshold, testing slight changes and fixed thresholds between infections, respectively. In the case 4, threshold α is explored mostly under slight changes between infections. In this sense, exploring these 15 scenarios, we test threshold conditions for antigen-specific reactions in sequential infections as well as the potential characterization of an increased breadth, and its possible effects in the magnitude of Abs response. Figures 3.5 - 3.9 report results of each tested scenario, each displaying the the average of the ten simulations per scenario. The figures show the Abs counts for each antigen, including antigens of infection, antigen-A and antigen-D for the first and second infection, respectively. The heat-map of Abs magnitude scales classifies the magnitude of Abs response counted for each of the six tested antigens. The color stands for the Abs magnitude at day 41 after the first infection and at day 84 after the second infection. The Figures also show the Abs dynamics of a particular simulation case of the tested scenario.

Case 1 - Diverse values for the variable area threshold, fixed between sequential infections. We tested several values of α and β affinity thresholds for both binding areas. First, we test the variable area threshold, fixing $\alpha = 2$, $\alpha = 3$, $\alpha = 4$, and $\alpha = 5$ for the two sequential infections. Threshold $\beta = 3$ in the conserved area remains fixed for all experiments, results are depicted in Figure 3.5. Considering a fixed α threshold, using $\alpha = 3$, Abs develop an antigen-specific response (Figure 3.5–B) generally in both infections. This phenomenon is more remarked when $\alpha = 2$, the Abs response is practically directed

Cases	Threshold α (first | second)	Threshold β (first | second)
Case 1	2 | 2	3 | 3
	3 | 3	3 | 3
	4 | 4	3 | 3
	5 | 5	3 | 3
Case 2	3 | 3	4 | 4
	3 | 4	4 | 4
	4 | 4	4 | 4
Case 3	3 | 3	3 | 4
	3 | 4	3 | 4
	4 | 4	3 | 4
Case 4	3 | 4	1 | 1
	3 | 4	2 | 2
	3 | 4	2 | 3
	3 | 4	3 | 3*
	3 | 4	5 | 5

* Optimal cross-reactome scenario.

Table 3.2: Exploration cases for the threshold values at the variable (α) and conserved (β) areas. The values stand for the sequential (first | second) infection setting.

to the antigen of infection (Figure 3.5–A), which could be limited to represent Abs cross-reaction for a family of viral antigens. Conversely, $\alpha = 4$ promotes a wide breadth of the Abs response in both infections, with weak specificity for the antigen of infection, the antigen-A, (Figure 3.5–C). Weaker Abs magnitude and specificity but breadth still to all antigens are shown when $\alpha = 5$ (Figure 3.5–D). Note that while the breadth and magnitude of response using $\alpha = 3$ in Figure 3.5–B may adequate to the Abs response representation for the first infection, the effect of antigen-specific reaction will no longer be desired since only some antigens like antigen-D, antigen-A and antigen-E develop high magnitudes. On the other hand, selecting $\alpha = 4$ as in Figure 3.5–C, breadth covers all of the antigens, however, reaction to antigen-B and -C is generally higher in magnitude with respect to the antigen of infection, antigen-A, a scheme that is not desired since weakens antigen-specific reactions.

Case 2 - Slight changes for the variable area threshold (α) between sequential infections, fixed (β) between infections. The affinity threshold of the conserved area is tested using $\beta = 4$ for the sequential infections, Abs dynamics is depicted in Figure 3.6. Regarding the threshold of the variable area, three scenarios were tested, first $\alpha = 3$ for both infections in Figure 3.6–A, also the threshold varying with $\alpha = 3$ (first infection) and $\alpha = 4$ (second infection) in Figure 3.6–B. Finally, Figure 3.6–C shows results with a fixed value of $\alpha = 4$. For all cases, the first infection develops broad responses, however, the magnitude of response remains in the low scales of the heat-map, with a maximum general magnitude between 10^4 and 10^5 of counts in the heat-map scale. Also, the breadth for the first infection slightly covers some of the antigens, such as the cross-reaction for antigen-F. Using a dynamic change of threshold α between infections, the Abs develop higher levels of breadth and magnitude, covering all of the tested antigens. For this scenario, the specificity of response to the antigen of infection is higher, especially for the first infection, compared to the rest of scenarios for the case. Note that for the first scenario of Case 2, antigen-specific

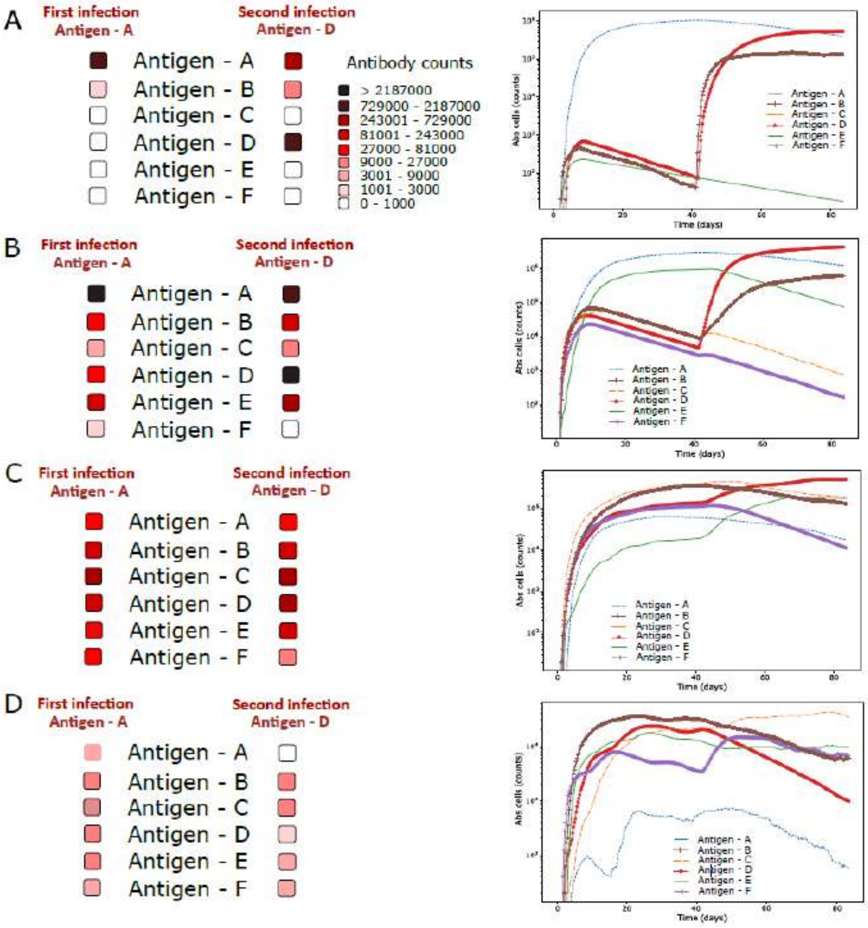

Figure 3.5: Fixed threshold tests for the variable area α. Tests using $\alpha = 2$ (A), $\alpha = 3$ (B), $\alpha = 4$ (C), and $\alpha = 5$ (D). The threshold $\beta = 3$ remains fixed for all scenarios. The heat-map of Abs magnitude scales classifies the magnitude of Abs response counted for each of the six antigens. The color stands for the Abs magnitude at day 41 after the first infection and at day 84 after the second infection, using antigen-A for the first infection and antigen-D for the second infection. Panels of Abs dynamics over time of a particular simulation case depict each antigen with different colors and symbols. This plotting framework is considered in Figures 3.6 - 3.9.

response is developed for the second infection and the Abs magnitude is generally developed to reach 10^6 for antigen-D while Abs magnitude actually decay for the rest of the antigens.

Case 3 - Slight changes between sequential infections for both thresholds. In Figure 3.7, we explored $\beta = 3$ for the first infection and $\beta = 4$ for the second infection. Regarding the threshold of the variable area, three scenarios were tested, first $\alpha = 3$ for both infections in Figure 3.7–A, also the threshold varying with $\alpha = 3$ (first infection) and $\alpha = 4$ (second infection) in Figure 3.7–B. Finally, Figure 3.7–C shows results with a fixed value of $\alpha = 4$. Generally, for the first infection with $\beta = 3$, the Abs cross-reaction is developed towards all of the antigens, with special focus on the antigen of infection. However, when $\beta = 4$ for the second infection, diverse panoramas can be appreciated as the threshold α varies. First, the Abs response becomes quite antigen-specific for the antigen of the infection and a weak magnitude of response is developed for the remaining antigens. Second, the

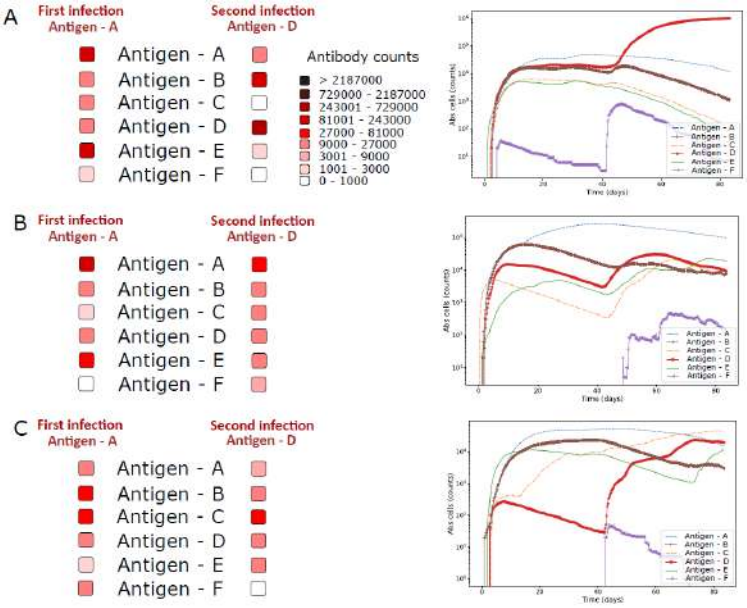

Figure 3.6: Test of affinity threshold for the conserved area, $\beta = 4$ for the first and second infections. The test uses the antigens antigen-A and antigen-D for the first and second infections, respectively. A) Fixed threshold of $\alpha = 3$ for the first and second infection. B) A dynamic threshold of $\alpha = 3$ for the first infection and $\alpha = 4$ for the second infection. C) Fixed threshold of $\alpha = 4$ for the first and second infections. The Abs heat-maps display the average of ten simulations. The Abs dynamics show a particular simulation case.

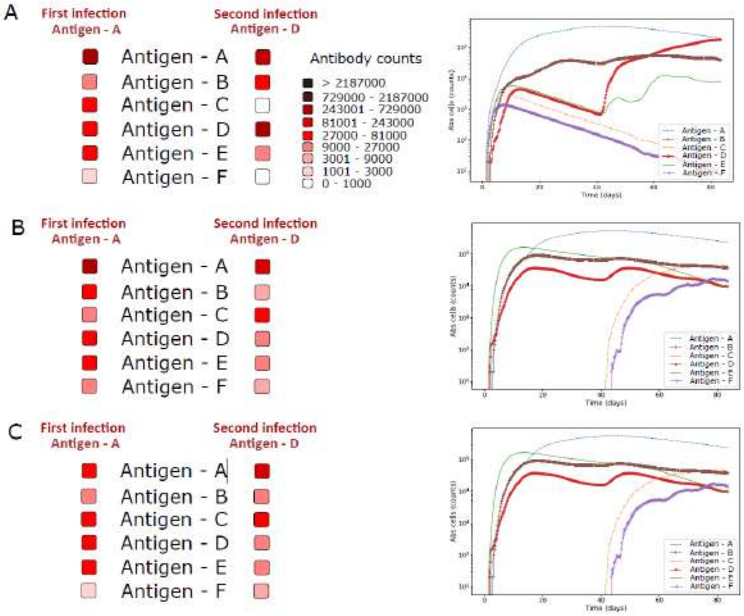

Figure 3.7: Test of affinity threshold for the conserved area, $\beta = 3$ for the first infection and $\beta = 4$ for the second one. The test uses the antigens antigen-A and antigen-D for the first and second infections, respectively. A) Fixed threshold of $\alpha = 3$ for the first and second infection. B) A dynamic threshold of $\alpha = 3$ for the first infection and $\alpha = 4$ for the second infection. C) Fixed threshold of $\alpha = 4$ for the first and second infections. The Abs dynamics show a particular simulation case.

response improves in breadth and magnitude for $\alpha = 4$ in Figure 3.7–B, however, the magnitude is not comparable to the optimal test. Finally, a similar scheme of Abs response is shown in Figure 3.7–C, with a great level of broad response. However, the magnitude of Abs level remains below those of the first infection, where it is generally desired that the Abs magnitude is enhanced after the second infection. In this sense, the outcome of scenarios in this simulation case 3 can guide an initial setting for a generally desired Abs dynamics, standing for $\alpha = \beta = 3$ for the first infection. One can note that slight threshold changes become key for the breadth and magnitude, and the exploration for those affinity limits may stand for avoiding fixed thresholds between infections.

Case 4 - Slight changes between sequential infections for variable area threshold (α), fixed and slight changes (β) threshold between infections. Results in Figure 3.8 depict a dynamic threshold α between infections, in all cases using $\alpha = 3$ (first infection) and $\alpha = 4$ (second infection). Following this framework, selecting $\beta \leq 2$ generally guides to an antigen-specific behavior and, considering $\beta = 5$, Abs responses are weak in breadth and magnitude, as depicted in Figure 3.8. When varying threshold $\beta = 2$ (first infection) and $\beta = 3$ (second infection), the broad response remains limited and is not able to reach strongly antigen-F, for instance. This is an effect mainly kept from the first to the second infection. However, from the set of scenarios tested in Case 4, one of them shows to develop broad responses that increase in magnitude during the second infection, where all of the antigens show high levels of Abs response, a scenario shown in Figure 3.9.

Enhanced breadth and magnitude of Abs response – optimal scenario. In the testing scenario of Figure 3.9, the magnitude of Abs response is not only kept for all of the antigens, but is also increased in most of them. This scenario renders a cross-reactome that may stand for an optimal combination of dynamic thresholds for the variable area while keeping a fixed threshold for the conserved area. The threshold values configuration can be initially identified in previous tests, such as the second scenario of Case 1 and the first two scenarios of Case 3. In these tests, the initial threshold values allow identifying a broad response for the first infection, balancing breadth and specific responses. On the other hand, the third scenario of Case 1 could represent a great level of breadth response while showing weak specific response to the antigen of infection, especially in the first infection, a scenario contrasting with the second test of Case 3 during the first infection, that, however, develops rather specific responses to the second antigen. Thus, it was identified that a threshold of $\alpha = 3$ during the first infection and a threshold of $\alpha = 4$ for the second infection, and the threshold of the conserved area $\beta = 3$ fixed in both infections, may fairly represent the Abs cross-reactive phenomena of the sequential infections observed with influenza strains [5]. The scenario outcome for such configuration is depicted in Figure 3.9 where one can note that while for the first infection, the magnitude is mainly towards the antigen of infection, antigen-A, for the second infection, the Abs magnitude reaches the complete set of antigens. Figure 3.9-B,C depict a case simulation outcome of the B-cells and plasma cell dynamics for all of the antigens while Figure 3.9-D depicts the Abs response following the plasma cell dynamics. The Abs mean of the tests for this scenario and a 90% confidence interval for each strain Abs dynamics are depicted in Figure A.1.

Taking the four cases with their scenarios together, for the combinations of the different values of affinity thresholds, this chapter emphasizes the necessity of changes between infections for the variable area affinity threshold, which may become a necessary condition

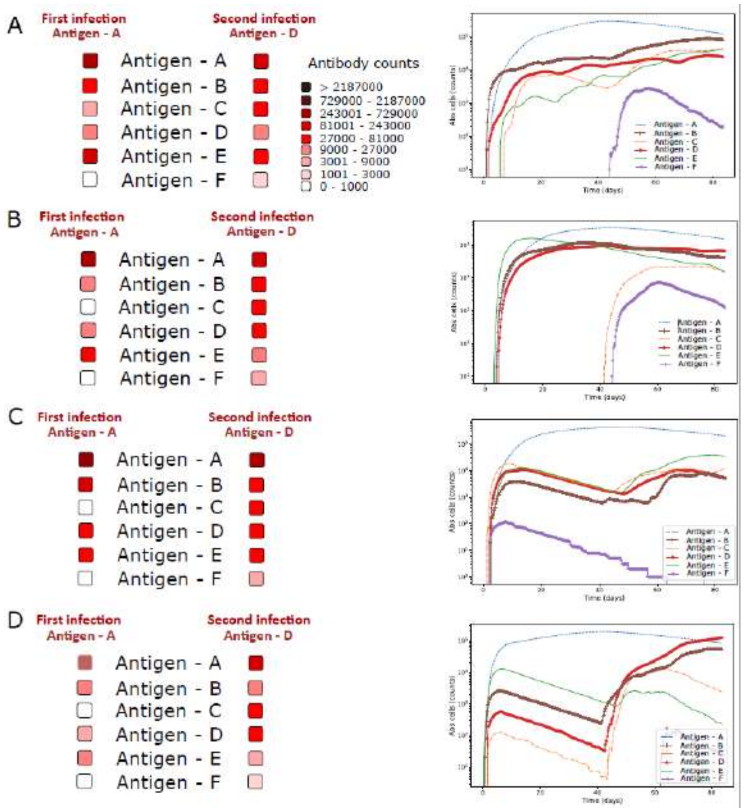

Figure 3.8: Test of affinity threshold (β) for the conserved area. The test uses antigen-A and antigen-D for the first and second infections, respectively. A) Fixed threshold of $\beta = 1$ for the first and second infection. B) Fixed threshold of $\beta = 2$ for the first and second infection. C) A dynamic threshold of $\beta = 2$ for the first infection and $\beta = 3$ for the second infection. D) Fixed threshold of $\beta = 5$ for the first and second infection. The Abs heat-maps display the average of ten simulations. The Abs dynamics show a single simulation case. A particular scenario of Case 4 is shown in Figure 3.9, where the breadth and magnitude is enhanced during the second infection.

that rises from the set of tests to describe the overall phenomena observed in experimental studies dealing with sequential infections with influenza virus [5], generally rendered in Figure 3.1–B. Affinity changes may direct the breadth and magnitude of response in Abs cross-reaction. As affinity changes relate key mutations that may become difficult to reach as the second antigen is presented, some mutations might be beneficial for breadth, as they will enhance contacts with the proportion of antigen previously known, the conserved area. This may be consistent with previous observations indicating that slight mutations enhance breadth and potency by providing increased flexibility and/or direct antigen contact [24, 23].

3.3.2 Breadth and magnitude to related antigens

Using the identified threshold setting that favor Abs breadth and magnitude, we explore the effects of the antigenic difference for the cross-reactive outcome by selecting other antigenically closed or distanced antigens in terms of the Hamming distance. Those antigens that have a relatively small level of difference are called the internal clusters (antigens) while external clusters refer to those that have the greatest distance. Alike previous models where

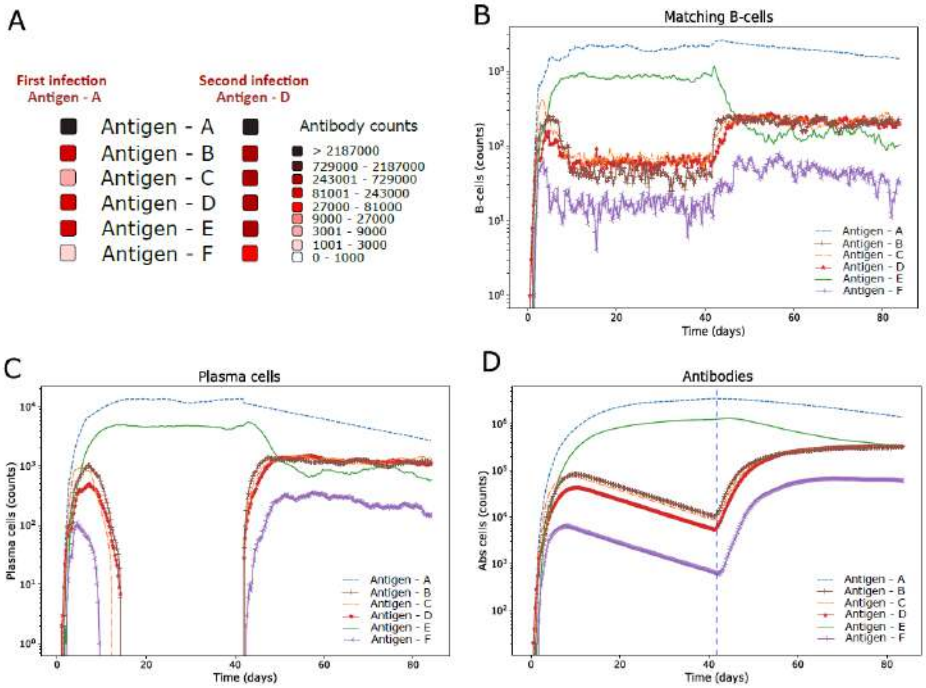

Figure 3.9: Antibody cross-reation to secuential infections – optimal Abs response scenario. A) Antibodies counts for each antigen, including antigens of infection, antigen-A and antigen-D for the first and second infection, respectively. The heat-map of Abs magnitude scales classifies the magnitude of Abs response counted for each of the six tested antigens. The color stands for the Abs magnitude at day 41 after the first infection and at day 84 after the second infection. (B) B-cells matching for each antigen plotted as a function of time. (C) A high-affinity B-cell has the chance to generate a plasma cell that decays according to its half-life. Due to a combined effect of the high threshold for the variable area during the second infection and affinity maturation, the plasma cells in the Antigen-D infection manage to remain more time than for the Antigen-A infection. (D) The Abs dynamics for each antigen over time.

the antigenic distance closely relates to the breadth of Abs for a given limit in antigenic Hamming distance [6], the scheme here presents no predefined limit for cross-reaction, letting the Abs dynamics to develop on the basis of affinity for the family of antigens. In this sense, considering the distance between antigens in Table 3.1, where the maximum case is a distance of ten, this number is considered as an indicator for setting the internal and external clusters. Internal clusters are considered as with Hamming distance of up to five while external clusters are those of Hamming distance of at least ten. For the internal clusters, the antigen-E strain was selected for the first infection and the antigen-B for the second one. The Hamming distance between these antigens is five. Results are shown in Figure 3.10–A, where high breadth and magnitude can be observed. Sequential infections with external clusters are tested with antigen-F and antigen-D for which the Hamming distance is 10. Results of external clusters are shown in Figure 3.10–B, where a strain-specific shape can be observed, especially for the first infection.

The general behaviour of the sequential infections for antigenically closed and distanced antigens follows the shape of the optimal test, especially during the second infection where Abs are generated to all antigens. The last set of tests may add to the scheme presented in Figure 3.1–B. The breadth of responses may reach antigens sharing structural characteristics

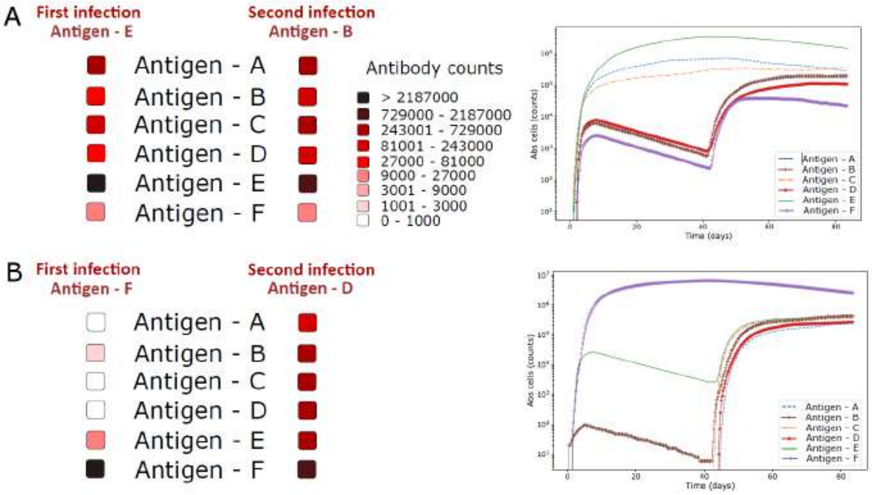

Figure 3.10: The internal clusters test shows the influence of antigenic similarity between antigens through sequential infections, using closely related antigens (A) and distanced antigens (B). The heat-map displays the intervals of Abs counts for different antigens with the same characteristics of Figure 3.9. (A) Abs counts after the first infection with antigen-E and second infection with antigen-B. (B) Abs counts after the first infection with antigen-F and second infection with antigen-D. Abs dynamics is depicted for each of the cases.

such as those of an influenza subtype, for H3 or H1 strains. Further scenarios should explore the breadth toward heterosubtypic responses, where the conserved area of the antigens may contain not only slight changes among the family, but also may require to explore other accessibility schemes.

3.3.3 Time and inverse order of sequential infections

Further informative results rely on the time windows between infections and the inverse order of infection of antigens. We tested three time windows between infections, considering the second infection 10, 20 and 84 days after the first infection using the antigens of the cases tests, results are depicted in Figure 3.11–A–C. A six-week maximum time window (42 days, as in the principal test) between infections resulted in favoring Abs development and better cross-reactive outcome. The test using 84 days after the first infection (Figure 3.11–C) manages to generate medium to high Abs magnitude, however, it is still lower compared to the Abs levels for 10 d, 20 d and the principal test with 42 days after the first infection.

The inverse order tests explore the Abs outcome employing the same antigens as in the cases tests but in the opposite infection order, that is, using antigen-D followed by antigen-A for the sequential infection protocol. The time between infections remains as in the principal tests, 42 d. It was found that the Abs outcome in the first infection produces a slightly lower magnitude of cross-reactive Abs, however, as can be observed in Figure 3.11–D, the breadth of cross-reaction covers almost all antigens of the group. After the second infection, the general Abs outcome observed in Figure 3.11–D is comparable to the principal test. To summarize, for the antigens employed in this tests, a *commutative* outcome can be observed between these antigens, which can be dependent on the selection of the antigen and due to the static setting of them may aid in the shape of the commutative results - differences in antigen mutation rates may affect the commutative outcome [170]. These changes may

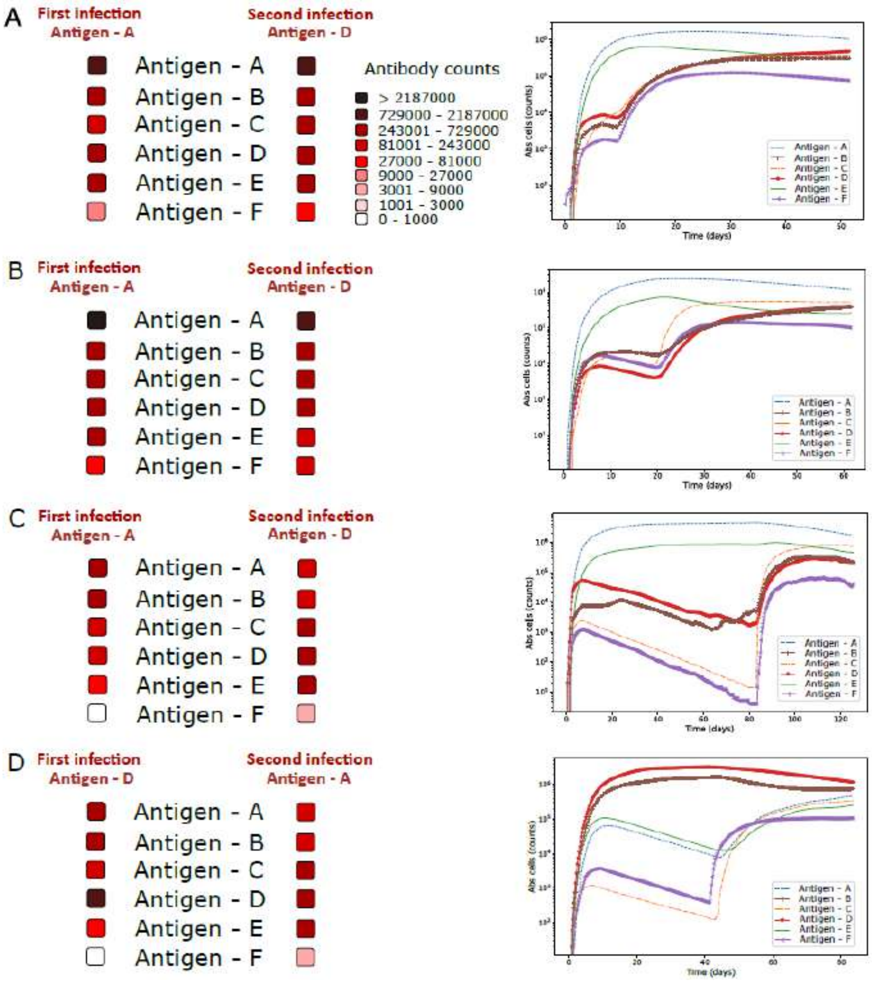

Figure 3.11: Test for time and orfer of infection. A red-colored heat-map displays the intervals of Abs counts for antigens with the same characteristics of Figure 3.9. The time windows between infections are tested for 10 d (A), 20 d (B), and 84 d (C). Also, the test for conmutative infections respect to the pincipal test is shown in panel (D), which uses antigen-D and antigen-A for the first and second infections, respectively.

handle the commutative shape with, for instance, reordering among antigens in influenza infections (strains). A comparison of different influenza strains mutation rates during the time scales of infection is further needed to better inform on the commutation results.

3.4 Discussion and schemes for future studies

In this chapter, we present a modeling framework for Abs cross-reaction in sequential infections, a scheme that results in a high breadth and magnitude of Abs using related antigens, such as the strains of a subtype of the influenza virus. We incorporate previously explored frameworks for modeling Abs responses to complex antigens, such as HIV and influenza. We account for the antigenic distance between antigens of infection on the basis of the dimensionality of antigenic cartography and influenza shape-space parameterization, the representation of antigens using strings of characters focusing on the binary alphabet, and link antigenic distance and binary strings via the Hamming distance [6, 20, 21, 22]. In addition, we incorporate schemes for the B-cell-antigen binding affinity, the fitness of B-cells for the presented antigen, and a dynamical affinity framework via the longest common substring between the conserved and variable portions of the B-cell-antigen binding areas [7, 8]. Such schemes have been used for exploring affinity maturation processes.

Antibodies cross-reaction has been generally questioned on the basis of affinity, B-cell population fitness, the effects of antigenic distance, and the use of further immune elements analysed in single infections. However, these elements may not be sufficient to render a particular set of sequential infections; strain-specific with a low to middle broad response to the first infection, and an extended response in breadth and magnitude for the second infection [5], a phenomenon illustrated in Figure 3.1. While antigenic distance and dimensionality may reflect on affinity to one antigen or the other, broad responses can only regard affinity maturation, common substrings in the variable and conserved areas, and a possible interplay between the forces focussing on them. In this context, for instance, the presence of key mutations on each of the areas, those in the middle of the area strings in our model, allows to in- or decrease the common substring, therefore, in- or decrementing affinity. Current approaches barely explore the possibility that dynamics of receptor-antigen binding may strongly impact the efficacy of Abs responses from one infection to a later one. In this sense, we also explored the flexibility of affinity thresholds in the conserved and variable areas between sequential infections towards identifying possible settings that allow reasonable representations of the breadth and magnitude of Abs response.

Previous studies have identified similar dynamic settings –a footprint shift that focuses on conserved viral residues– observed during HIV-broad Abs development [171, 172]. Also, in responses without a flexible footprint, broad clones are quickly outcompeted by strain-specific ones and get decreased in magnitude [171, 172, 23]. Such an effect is also reflected in our simulations, especially in Case 2, where using fixed thresholds for $\alpha = 3$ and $\beta = 4$ resulted in losing breadth and magnitude during the second infection. On the other hand, also using fixed thresholds between infections in Case 1, breadth is reached with an antigen-specific outcome when $\alpha = 3$ and even increased if using $\alpha = 4$, the last at expenses of specificity, both scenarios using $\beta = 3$. In this sense, the model suggests that dynamic settings for the affinity thresholds between infections may contribute to Abs cross-reaction.

The biological players behind this dynamic phenomenon need to be better explored. Some lines may initially guide this path, using structural and functional analyses, for instance, it has been informed that somatic mutations in framework regions (a subdivision of the variable region of the antibody) residues enhance breadth and potency by providing increased flexibility and/or directing antigen contact [24]. In addition, structure analysis of certain lineage antibodies has demonstrated maturing epitopes to focus on the conformationally conserved portion of the CD4 binding sites [171, 23]. Also, based on broad responses of Abs, recent modeling studies suggest that B-cell receptors can search across potential binding targets on the viral protein and place at the site of best complementarity; broad clones primarily target conserved residues whereas narrow clones chiefly bind variable elements. Provided such flexibility in recognition and affinity, B-cell receptors can spontaneously switch in a way that mitigates the tension in response to changing selective forces [23]. Related concepts have been explored in the context of a trade-off evolution in changing environments [173]. Furthermore, B-cells may utilize affinity-enhancing mutations outside the current contact region while buffering affinity reduction within the contact, thus enhancing the rate and size of favourable changes [8, 23]. This target switch allows strain-specific ancestors to generate cross-reactive descendants, enabling persistent adaptation to new antigen encounters [23]. The last might be reflected in our model, the affinity-enhancing mutations outside the contact region of the first antigen, given by a slight change in the affinity threshold in the second infection, will demand critical mutations for the current region (variable area), while no extra efforts may be demanded in the conserved area, which its affinity turns out to persist via the actual B-cell population fitness that already contains a level of broad players from the first infection. We are aware that this initial scheme integrates slight dynamic changes in a rather explicit and even almost arbitrary fashion between the infections, feedbacking from the Abs breadth and magnitude outcome. However, we consider this could be consistent with studies of evolutionary antigen-B-cell binding [23], which may stand for an optimized setting where affinity shifts could be further integrated into our model, to dynamically vary based on antigen variation (due to new infection but not to antigen mutation in the host), timing and B-cell population affinity.

As for additional cross-reaction modeling procedures, besides proposing binding interaction flexibility within and between antigen areas, we introduce an antigenic distance cutoff-less breadth and magnitude. Unlike other schemes [109, 6, 157], we do not explicitly set a limit for Abs cross-reaction due to antigenic distance, and Abs have the possibility to bind any member of a family of related antigens only based on the overall Abs fitness. In principle, earlier studies explored a breadth cutoff translated into limiting binding interactions based on a certain Hamming distance. We keep the concepts of antigenic distance and the Hamming metric, but Abs breadth is flexible. Highly distanced antigens would also reach different levels or no magnitude at all, but this only mirrors the current B-cell population fitness for the presented antigen. The opposite case can also happen, a related, shortly distanced member of the antigen family can be reached but can also develop minor magnitudes. More recent models incorporate mapping of antigenic sites of influenza through strings of characters that obey antigenic maps using antigen sequencing instead of hemagglutination inhibition essays [152, 157]. Such framework conserves the breadth cutoff, however, among their outcomes, it figures out that Abs cross-reaction can reach the most distanced antigens, although the magnitude is rather strain-specific [157]. This kind of outcome is also reflected in our scenario using fixed $\alpha = 3$ and $\beta = 3$ in Case 1, where both infections behave antigen-specific, with magnitude loss in the second one. However, we consider that the cutoff scheme could present limitations especially when approaching more than one family of antigens. Abs can reach heterosubtypic and intergroup cross-reaction [5, 107], therefore, rendering under a cutoff setting will make it merely harder to explore mechanisms for antigen-specific in parallel with broader responses, such as those in influenza infections.

Further investigation could also include immune elements to explore larger time windows, along with exposures to related antigens with the basis of middle to larger antigenic distances. This should generally picture exposures on the basis of, for instance, seasonal influenza. For such a framework, key immune elements are memory B-cells and multiple germinal centers. Memory B-cells that exit a germinal center continue circulating and could be reactivated by a second exposure to the antigen that originally activated its development. Memory B-cells can also then seed new germinal centers upon immunization with a second antigen that is different from the first antigen but shares conserved residues [174]. In this direction, the model would extend to account for activation and survival signals for B-cells together with phenomena of dark (for recycling and mutation) and light (for selection) zones in germinal centers, as well as the termination of them [16]. Thus, antigen recognition and binding threshold flexibility, memory B-cells, antigenic variations (due to shift and drift), and germinal center processes may guide exploration paths for modeling lifelong exposures.

Taking it all together, this Chapter highlights how affinity dynamics interplay could drive non-intuitive processes at a system level, and possible settings for flexible antigen-B-cell interactions-mediated evolutionary and autoregulated immune dynamics. We expect this serves as an adding point for studying and lately understanding the complex immune processes to a viral infection that ultimately could inform research in influenza infection and vaccine development.

Chapter 4

Control–based treatment tailoring for influenza infection

Neuraminidase inhibitors are currently used to treat influenza, however, treatment recommendations remain debatable. In this chapter, discrete-time inverse optimal impulsive control schemes are proposed to address the antiviral treatment scheduling scheme. Results regarding stability, passivity, bounded inputs, and optimality for the impulsive action are adapted. The study is founded on mathematical models of influenza A virus adjusted to data from clinical trials where participants were experimentally infected with influenza H1N1 and treated with NIs. Results show that control-based techniques can tailor dosage and reduce the amount of medication while simultaneously reach the efficacy levels of the current FDA (WHO approved) recommendations. Monte Carlo simulations disclose the robustness of the proposed control-based techniques while exploring the applicability to the personalized treatment of infectious diseases through a virtual clinical trial. *This chapter extends in a didactic manner the partial content of Refs. [65, 127, 136]*[1].

4.1 Introduction – modeling and control bases

4.1.1 Host level modeling of influenza infection and treatment dynamics

Mathematical models of infectious diseases have been developed to provide different levels of detail to give quantitative insights into within-host viral dynamics, for instance, to quantify the influenza A virus infection level and to identify potential therapeutics to influenza

---

[1] Partial reprint from Ref [65], Gustavo Hernandez-Mejia, Alma Y. Alanis, Miguel Hernandez-Gonzalez, Rolf Findeisen, and Esteban A. Hernandez-Vargas, Passivity-Based Inverse Optimal Impulsive Control for Influenza Treatment in the Host, Transactions on Control Systems Technology, © 2019 IEEE.
Partial reprint from Ref [127], Gustavo Hernandez-Mejia and E.A. Hernandez-Vargas, PK/PD-Based Impulsive Control to Tailor Therapies in Infectious Diseases, IFAC-PapersOnline, 53/2 (2020), pp. 16055–16060, Elsevier (CC BY-NC-ND license).
Partial reprint from Ref [136], Gustavo Hernandez-Mejia, Xin Du, Alma Y. Alanis, and Esteban A. Hernandez-Vargas, Bounded input impulsive control for scheduling therapies, Volume 102, Pages 34-43, Copyright (2021), with permission from Elsevier.

disease. The first mathematical model to describe influenza dynamics, using experimentally infected mice, was developed by Larson *et al.* in 1976 [26]. Baccam *et al.* later presented a model of influenza infection kinetics in humans, adopting the well-known target cell-limited model [10], depicted in Figure 4.1-A. In this simple model, influenza infection is limited by the availability of susceptible target (epithelial) cells rather than the effects of the immune response. Some models have also sought to integrate the eclipse phase, the period between successful cell infection and the virus release (depicted in Figure 2.3), from *in vivo* and *in vitro* studies attempting to represent time windows from infection to viral release [49, 10, 175]. The target cell model has been fitted to human influenza data, however, similarly to the previous models, the study raised identifiability issues since the parameters can not be estimated uniquely from the corresponding experimental data [47]. Parameter uncertainty fitting has been tried to be reduced using the target cell model by measuring both infectious and total viral load. However, while the infectious load is reported via 50% (median) tissue culture infectious doses (TCID_{50}) (Definition 4.1), the total viral load is measured via reverse transcription-polymerase chain reaction (RT-PCR) (Definition 4.2), and the variation in TCID_{50} assay sensitivity and calibration affected the parameter estimation [48].

Definition 4.1. *Median Tissue Culture Infectious Dose ($TCID_{50}$). This is an essay whose method is used to quantify the viral titer of a testing virus. Host tissue cells are cultured on a well plate titer, and then varying dilutions of the testing viral fluid are added to the wells. After incubation, the percentage of infected wells is observed for each dilution, whose results are used to compute the $TCID_{50}$ value [176] (computation procedures can be found in Ref. [177]).*

Definition 4.2. *Reverse Transcription - Polymerase Chain Reaction (RT-PCR). This is a sensitive technique for the quantification of steady-state mRNA levels, particularly in samples with limited quantities of extracted RNA, or for analysis of low-level transcripts. The procedure amplifies defined mRNA transcripts using the retroviral enzymes with reverse transcriptase (RT) activity, later coupled to PCR [178].*

Better understanding key factors guiding the influenza infection course is crucial, this involves not solely the activity of epithelial cells but also the immune host responses. Modeling such schemes had taken diversified paths, with some studies attempting to establish a comprehensive view of the host response [27, 28] while others have pursued more focused approaches, detailing the role of IFN-I, NK cells, and the relevant role in the clearance of the viral infection by CD8+ T cells [49, 179, 180, 181, 182]. CD8+ T cells are responsible for clearing infected cells and resolving the infection. The infiltration of these cells into the respiratory tract is coincident with virus decay and the infection conclusion [183, 184]. Further models of control of influenza virus infection through CD8+ T-cell have also uncovered important details about long-term protective immunity, such as the plateauing of memory CD8+ T cells promoted by repeated exposure to influenza viruses [29, 30, 31]. For reviews on mathematical models of influenza infection, immune response, data from *in vivo* and *in vitro* studies, host animal and human models, and modeling platforms, see Refs. [49, 31, 185].

Regarding therapeutic schemes, treatment dynamics can be also explored using mathematical models that help identify sources of variability in the dose-concentration-effect

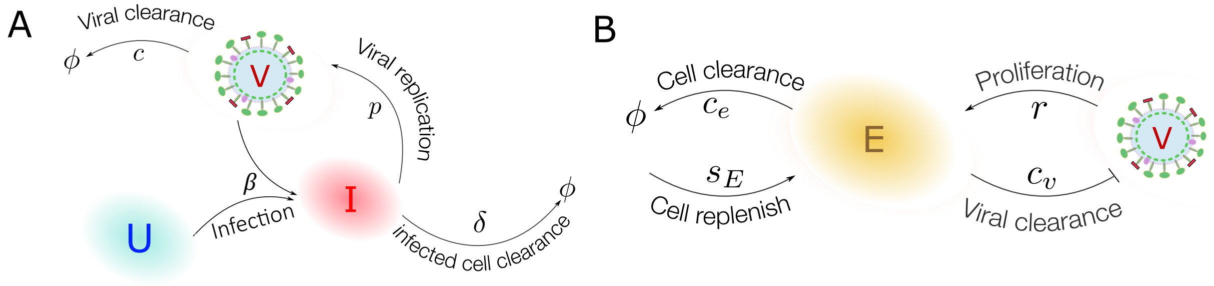

Figure 4.1: Influenza infection models. A) Target cell-limited model. The virus (V) infects susceptible cells (U) with rate β while infected cells are cleared with rate δ. Newly infectious cells (I) release virus at rate p and viral particles are cleared at rate c. Equations (4.1)-(4.3) stand for the dynamics of the target cell model. B) Infection model with CD8+ T cells (CD8) response. The virus (V) induces CD8 (E) clonal expansion with a rate r inhibiting the viral replication through the clearance of the infected cells, an effect represented by c_v. CD8+ T cells are replenished with rate s_E and die with rate c_e. The dynamic infection model is described in (5.22)-(5.23) in Chapter 5. Note that in both models the viral clearance is represented by ϕ. Panel B was adapted from Ref. [49].

relationship of a drug. This is essentially the goal of the PK/PD schemes (Definition 4.3) and consists of a variety of modeling paths whose principal characteristics are depicted in Figure 4.2. PD models of response usually cover several dependent variables as clinical endpoints, surrogates, and biomarkers. However, in most cases, only one of them is modeled at a time. It is therefore important to choose an appropriate dependent variable that is meaningful, appropriate for modeling, and that preferably can be measured [9].

Definition 4.3. *PK/PD schemes. PK is frequently referred to as ”what the body does to the drug”, this scheme includes the processes of absorption, distribution, metabolism, and excretion that govern the concentration-time course of a drug in blood or plasma, using compartments as dynamics blocks of the concentration-time course. PD, on the other hand, describes ”what the drug does to the body”. This approach centers on the drug effect depending on time and drug concentrations in the past -if available- until the present, along with additional covariates [9, 34, 33].*

A common scheme that describes the concentration-effect relationship on the PD phase in a rather simple manner relies on considering the maximum drug effect under the EC_{50} value, which is the concentration that generates 50% of the maximum effect [9]. This approach resembles the increasing trend of drug effects as the drug concentration increase. On the other hand, PK models use compartments as dynamics blocks to describe the concentration-time course. This is a usual abstract concept that assumes that the drug is homogeneously mixed and shares similar kinetics in a certain region of the body [186]. PK models generally integrate the bioavailability which is the fraction of the drug that is systematically absorbed and being available to produce an effect. Other characterizations regard the area under the curve of drug concentration in blood over time, the half-life which is the time for the drug to

---

[2] Figure 4.2 is reprinted from Lafont, E., Urien, S., Salem, J. E., Heming, N., and Faisy, C., Modeling for critically ill patients: an introduction for beginners, Journal of Critical Care, 30(6), 1287-1294, Copyright (2015), with permission from Elsevier (License Number 5158370430409, reuse in a thesis/dissertation).

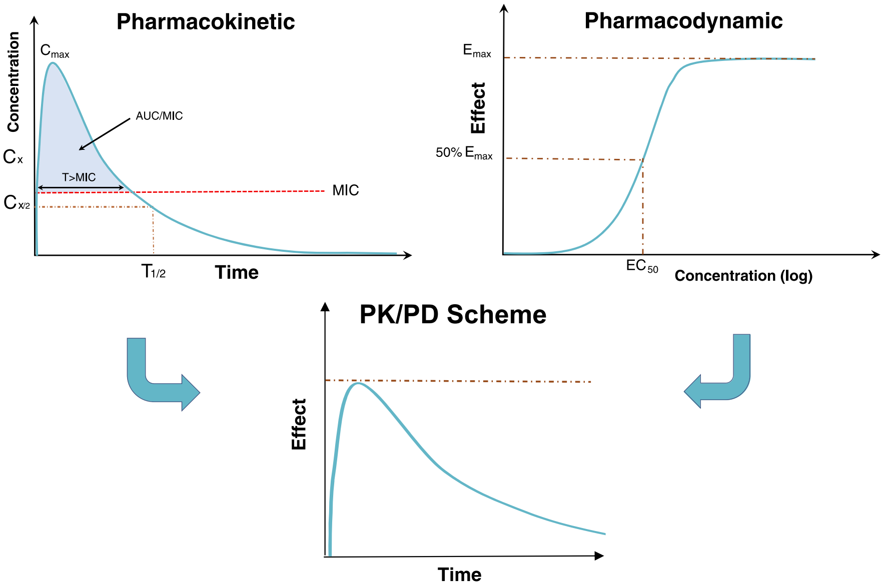

Figure 4.2: PK/PD dynamic schemes. PK stands for compartments that represent the concentration-time relation of a drug. For such relation, MIC is the minimum inhibitory concentration defined as the lowest or minimum antimicrobial concentration of a drug that inhibits visible microbial growth, $T_{1/2}$ is the half-life which is the time required to move from a drug concentration C_x to half of its concentration $C_{x/2}$, with C_{max} being the maximal concentration. In the case of PD, EC_{50} indicates the concentration producing 50% of maximum effect (potency), E_{max} is the maximum effect (efficacy), which can become uniform after a certain concentration. Together, the PK/PD scheme stands for the effect-time relation a drug can have and is used for exploring therapeutic endpoints. This figure was adapted from Lafont *et al.* in Ref. [32][2].

lose half of its biological activity, and the volume of distribution that is a theoretical volume of blood that the administered drug would have to occupy [186, 32, 9].

Coupled together, PK/PD models integrate the dynamics components into a set of mathematical expressions, this approach has been employed at different stages of drug discovery and application by pharmaceutical companies to improve drug efficacy and productivity as well as at the clinical level [34, 33]. In this direction, the application of modeling and simulation to understand data during drug development can potentially bring improvements towards model efficiency and approximation, especially when taking advantage of population-level modeling such as virtual clinical trials [187, 188].

4.1.2 Panorama of control-based schemes

Control theory is a framework for guiding a system to behave as desired by calculating the system input which normally also satisfies some optimality criteria and keeps the system stable (Definition 2.16). There are many types of applications of control frameworks, a commonly used scheme is the closed-loop control. Examples can go from controlling the water temperature of a boiler to controlling the wings of an aircraft, or even controlling the glucose levels of a diabetic person (via hybrid control, see Ref [189]), examples are depicted in Figure 4.3. Closed-loop control, also known as feedback control, combines a set of mechanical, electronic, computational elements, among others to automatically regulate

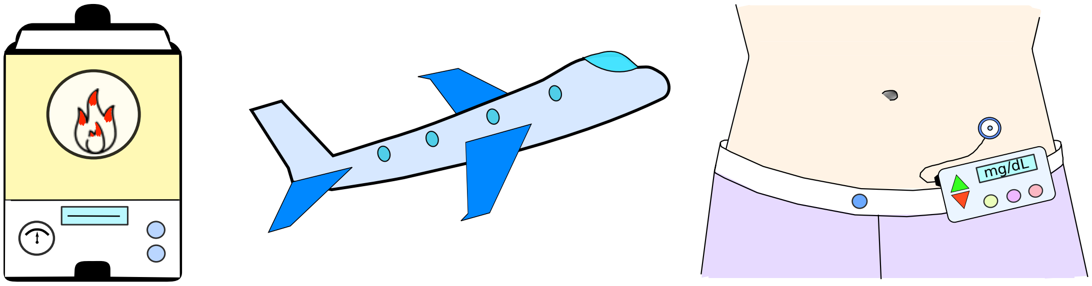

Boiler system

Aircraft system

Insulin pump system

Figure 4.3: Cartoon of control systems examples. A controller in a boiler system performs to keep water temperature to a defined set point. Similarly, the control systems of an aircraft maintain the stability and direction of the fuselage through a complex network of sensors that feedback information about the position, direction, among others. The insulin pump, finally, is a control system to keep the glucose level within a recommended range. Sensors report the glucose concentration in the body to the controller, which computed the necessary insulin amount to be administered for defined time periods. Controllers in these examples seek for the stability of the system - temperature, direction and inclination, and glucose level, respectively. However, controllers also perform to satisfy optimization criteria like, for instance, the time to stabilize an aircraft with minimum aviation fuel, or in the case of insulin, set an optimal amount of insulin for a certain carbohydrate input.

the system input to the desired set point using mathematical models. Feedback control is classically formed by four elements, the system (also called *the plant*), the feedback signal which can be from a sensor, the set point, and the controller [11]. We can easily identify these elements in the above examples. In the case of a boiler, the system is the mechanism that heats the water, this can be de- or activated depending on if the set point, the desired water temperature, is reached. The feedback signal is given by a thermostat that directly measures the water temperature and reports it to the controller. The last is the actual mechanism that turns the heater system on/off according to the set point and the information provided by the feedback sensor. In the case of an aircraft, the system can be considered as the complete set of mechanisms that form the aircraft, such as the fuselage - the aircraft's main body section, the wings and engines, vertical and horizontal stabilizers, among others. The set point must satisfy indicators to, for instance, keep the aircraft stable in direction (i.e. straight, left, right) and inclination (i.e. up, down). The feedback mechanism is composed of a complex set of sensors that inform about the state of each of the above indicators. The task of the control system, is to indicate the wings and stabilizers to move in a certain direction with a specific rate to satisfy the desired direction and inclination. In an insulin pump system, the goal is to aid compensate glucose levels with insulin, especially those of hyper/hypoglycemia. The system is then the body itself, where the glucose level is to be controlled. The set point is to keep the body within the lower (70 mg/dL) and upper (110 mg/dL) bounds of glucose [190]. The feedback system is based on sensors that report the glucose levels and can also incorporate user-provided information, such as an estimated carbohydrate content of a meal [189]. The controller uses the information provided to calculate the quantity of insulin to be administered, usually in predefined time intervals [191].

Another key feature of the above control systems is the performance to meet some optimality criteria. Optimization consists of minimizing or maximizing a variable, function, or

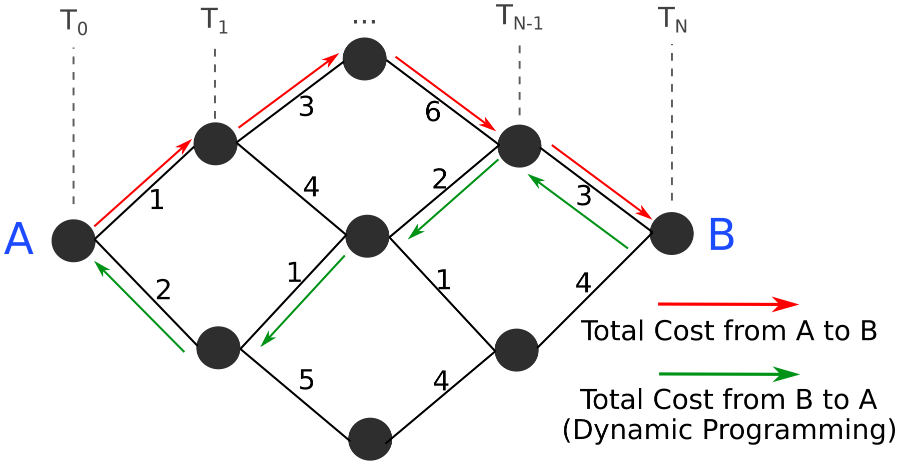

Figure 4.4: Illustrative scheme of dynamic programming. The cartoon shows the possible paths to go from point A to point B, points between A and B represent states that different paths can follow. The steps to go from point A to point B are represented by the upper numbers from T_0 to T_N. The cost to go between states is indicated with integers, where one can seek the minimum cost. Red arrows indicate the vision for selecting the minimum cost from one state to the next one, from A to B. On the other hand, the cost to go from A to B, from a perspective starting in B, is depicted with green arrows. While the total cost in red is 13, the cost in green is 8, the last stands for an optimized path using dynamic programming. The points in this scheme may represent the states of a system at a certain time, and the paths cost functions. Note that as the number of point values increases, i.e. real-world scenarios, the solution of dynamic programming becomes highly complex as each point represents a possible state value of a system dynamics at a certain time.

criteria by finding the best available values of some objective function to a defined input to the performing system [192]. In the example cases of Figure 4.3, the optimization criteria can be for example, in the case of the water boiler, to minimize the time to reach the set point temperature. It can also be the case, that it is desired to minimize the required energy to heat the water. In the aircraft example, a minimization rule can indicate maintaining a certain velocity with less aerospace fuel. In the case of the insulin pump, it can be the goal to minimize the postprandial glucose high peaks while integrating meal consumption characteristics. All the above examples currently use control systems and are widely accepted for optimization rules and performance. In this chapter and in Chapter 5, we seek to pave the way towards feedback control systems in infectious diseases, applied to the influenza treatment case, depicted in Figure 2.5. The system is, as in the case of the insulin pump, the body which is infected with the influenza virus. The set point is to eliminate the virus to undetectable levels. The controller will be a system that calculates the dose of the drug according to the system state while sensors report the viral load, cellular and immune behavior. Although the feedback technology is still to develop, mathematical frameworks can start rendering such mechanisms. Next, we theoretically explore the control schemes.

Optimal control seeks to find a control law for a given system such that a performance criterion is minimized. This problem is usually solved using dynamic programming, a technique for identifying the minimization path from the final point in time to the starting point, by solving for the path options. For illustrative purposes, Figure 4.4 shows a cartoon of the effect of selecting dynamic programing instead of solving forwards in time. In a general manner (red arrows), we evaluate the cost starting from point A to B (forwards in time). Selecting 1 (up) or 2 (down), in this case, selecting up for minimizing the cost. In the new state, options are 3 (up) and 4 (down), with the last being selected. The process continues until point B and the total cost is 13. On the other hand, using dynamic programming, we visualize from point B to point A (backward in time), where one can select from 3 (up) and 4 (down), selecting up, the process is repeated until point A with a final cost of 8. Considering a real-world scenario, the points in Figure 4.4 stand for the possible values of the state of a system at a certain time (the upper values T_0 to T_N), that is all vertical points for a given time step. This means that dynamic programing will look for minimizing the cost at all possible values of the dynamic system and all possible options of control inputs, which becomes a high dimension task to solve, this is referred to as the curse of dimensionality in dynamic programming [193]. The optimization criteria, the path from B to A, is usually formulated as a cost functional and therefore, formally, solving the associated Hamilton–Jacobi–Bellman (HJB) equation (Definition 4.4) is rather a difficult assignment since it involves solving partial differential equations in the form of (4.19) [194, 195].

In this sense, to solve the optimal control problem for nonlinear discrete-time systems with known mathematical models, diverse approaches are considered such as the heuristic dynamic programming (DP, Definition 4.5) methods [196], extended to obtain optimal control laws [197]. However, the ultimate scheme deals with the approximation (ADP) problem including variations on the structure of ADP, the development of iterative ADP algorithms, and applications of ADP schemes, a problem that may turn into a reinforcement learning approach [197, 198, 199, 200]. At this point, some concepts are introduced as *in words* descriptions, however, formal definitions are found in section 4.4.

Definition 4.4. *Hamilton–Jacobi–Bellman (HJB) equation. In optimal control theory, the Hamilton–Jacobi–Bellman equation sets necessary and sufficient conditions in terms of optimality of a control law regarding a cost function. The solution, usually for the linear case, can be used to compute the optimal control by defining the minimizer (or maximizer) of the HJB equation [201].*

Definition 4.5. *Dynamic programming. This concept refers to both a mathematical optimization method and a programming technique, it aims to simplify a complicated problem by mathematically breaking it down into simpler sub-problems in a recursive manner [202].*

Definition 4.6. *Control-Lyapunov function (CLF). The control-Lyapunov function is used to test whether a system is asymptotically stable, meaning that for any state x there exists a control $u(x)$ such that the system can be directed to the zero state asymptotically by applying $u(x)$ [203, 204].*

An alternative strategy that supports optimality at the expense of a meaningful cost function is the inverse optimal control which avoids solving the HJB equation [205]. In the inverse fashion, a stabilizing feedback control law is established, and then the corresponding cost functional is derived [206]. The inverse optimal control is a set of differential equations describing the shape of an objective function minimized with respect to the given control law and the initial state [207]. Hence, for the inverse approach, a stabilizing feedback control law, based on prior knowledge of a control Lyapunov function (CLF) (Definition 4.6) can

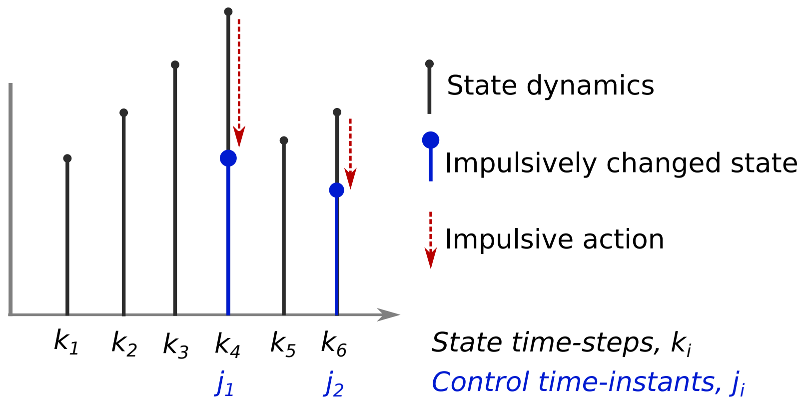

Figure 4.5: Scheme of an impulsive control system. The state dynamics (black pointed) evolve following the state time-steps k_i. The impulsive modification of the state (blue pointed) is the result of applying the impulsive action (arrow) at a certain instant, j_i. The magnitude and direction (increase or decrease) of the impulsive action can be suited as necessary for the control system. In this scheme, for illustrative purposes, only negative impulsive actions are drawn.

be designed first, and then it is established that this control law optimizes a cost functional [207, 208, 209, 210].

Concerning robust feedback features, control via passivation supports obtaining a robust stabilizing feedback scheme [211, 212]. Passivity systems theory is intimately linked to Lyapunov stability theory. A difference between the two approaches is that the state of the system and the equilibrium point are notions required in the Lyapunov approach while the passivity approach is rather based on the input-output behavior of the dynamic system. Considering these frameworks, a previous work considers a quadratic storage function as a CLF to obtain discrete-time inverse optimal control laws [212]. The existence of a CLF implies stabilizability and this expression can be considered as a cost functional [11, 213, 214]. The herein proposed methods integrate knowledge from the inverse optimal control theory, passivity systems, and CLF stability to design control laws for treatment scheduling, in the sense of the magnitude of control – the dose quantity tailoring.

On the other hand, there is the need to characterize the dose intake in the control system, hypothesized as instantaneous incorporation of the drug into the system at a certain time instant – the drug intake time. In this sense, impulsive control arises from the necessity to instantaneously change the state variables of a system. Impulsive control is, for instance, used if a system cannot be controlled by a continuous-time approach or if the input can only be applied at some k-th time-steps of a discrete-time system, namely the control instants (τ_k) [12, 215]. Such a framework is depicted in Figure 4.5, where the time-steps are given from k_1 to k_6 and with two control instants j_1 and j_2. At each control instant, the state (black point) is suddenly modified to a new value (blue point) with a certain modification magnitude (red arrow). Control instants can be chosen whenever some conditions are satisfied. The impulsive control law $U(\tau_k, x)$ is somehow related to the concept of control input in other control methods, however, it refers to giving a sudden change of state at instant τ_k.

Diverse studies have recently explored applications and problem solutions using impulsive schemes, going from finite-time stability and optimization problems with impulsive triggers to control of disease [35, 216, 217, 218, 219]. Taking the machinery above together, in this

Chapter we hypothesize a feedback control-based framework accounting for inverse optimal impulsive control strategies to design treatment tailoring techniques [64]. This scheme is based on the viral dynamics, the drug's PK/PD phases, and dose limits, as a feedback signals, towards rendering personalized treatment of influenza infection. The controller set point is the viral load under detectable levels. Results of this chapter serve as a basis for Chapter 5.

Notation

The notation employed through Chapter 4 and Chapter 5 is as follows: $\Re$ is the set of real numbers, $\Re^n$ is the set of $n \times 1$ column vectors, $\Re^{n\times m}$ is the set of $n \times m$ real matrices. $\aleph = \mathbb{Z}^+ \cup \{0\}$ is the set of non-negative integers, $S \subset \aleph$ is the resetting set, which is reserved for the control instants action. P^n is the set of $n \times n$ positive-definite matrices. Besides, $(\cdot)^T$ denotes the matrix transpose, $(\cdot)^{-1}$ stands for the matrix inverse, $\|\cdot\|$ stands for the Euclidean norm, and $|\cdot|$ denotes the absolute value.

4.2 Clinical trials with neuraminidase inhibitors

Clinical trial with zanamivir. Participants were healthy young adults susceptible to the challenge virus [220]. The volunteers were inoculated with $\backsim 10^5$ 50% tissue culture infectious doses ($TCID_{50}$) of a safety-tested pool of influenza A/Texas/91 (H1N1) virus by nasal drops of 0.25 mL per nostril. The experiment conducted four random, double-blind, placebo-controlled trials and followed a similar protocol using the same challenge virus. Zanamivir, in a range from 3.6 to 16 mg, was intranasally administered two or six times daily beginning 1 or 2 days after infection (early and delayed treatment) [220]. The concentration of zanamivir required for 50% of effect over viral replication (EC_{50z}, zanamivir) ranges between 0.22 to >100 μg/mL (1μM = 0.33 μg/mL) [221, 222]. For simulation purposes in this chapter, a value of 10 μM is taken. The intranasal spray volume is 0.1 mL [220], which is used for the unit conversion from μM to mg (the unit of drug quantity input). The EC_{50z} value of 10 μM is equivalent to ca. 3.3×10^{-4}mg. Further clinical trial details are in Ref. [220].

Clinical trial with oseltamivir. Healthy young adults were inoculated by intranasal drops of 0.25 mL per nostril with $\backsim 10^6$ $TCID_{50}$ of influenza A/Texas/36/91 (H1N1) [223]. Two randomized, double-blind, placebo-controlled, dose-ranging trials were conducted to test early treatment activity of oral oseltamivir capsules. Doses of 20 mg, 100 mg, or 200 mg twice daily, or 200 mg once daily of oseltamivir were administered starting 28 hours after inoculation. According to oseltamivir producer, EC_{50o} ranges between 0.0008 μM to >35 μM (1μM = 0.284 μg/mL) [224]. For simulation purposes, 0.028 μM is used based on the oseltamivir treatment data. The apparent volume of distribution for oral administration is 50 liters (employed to convert μM to mg) [225]. The EC_{50o} value of 0.028 μM is equivalent to ca. 0.4 mg.

4.3 Modeling of viral and drug dynamics

4.3.1 Influenza Host Model

The model described by Baccam *et al.* [10] is used for viral dynamics and treatment scheduling. The model has the following form

$$
\begin{aligned}
\dot{V}(t) &= pI(t) - cV(t), && (4.1)\\
\dot{U}(t) &= -\beta U(t)V(t), && (4.2)\\
\dot{I}(t) &= \beta U(t)V(t) - \delta I(t), && (4.3)
\end{aligned}
$$

where (U) represents the susceptible cells, (I) the infected cells, and (V) the virus. Susceptible cells become infected with a rate of β, infected cells shed virus at an average rate of p per cell and die at a rate of δ per cell [10]. Influenza virus is cleared at a rate of c per day, the effects of immune responses are implicitly included in the death rate of infected cells δ and the clearance rate of virus c. For both treatment scenarios, the initial conditions for (4.1)-(4.3) were taken from [47], these are $V(0) = 1 \times 10^{-5}$ TCID_{50}/ml, $U(0) = 4 \times 10^{8}$ cells and $I(0) = 0$ cells. For the zanamivir treatment, the model parameter values reported in Ref. [47] and data from Ref. [220] are used. Parameter values corresponding to the zanamivir treatment are β (6.3×10^{-2} ml/days·TCID_{50}), δ (1.3 days^{-1}), p (1.1×10^{-5} TCID_{50}/days·ml) and c (3 days^{-1}). In the case of oseltamivir treatment, the parameters to the viral mean data are adjusted from Ref. [223]. Parameter values for equations (4.1)-(4.3) are β (0.19×10^{-2} ml/days·TCID_{50}), δ (2.6 days^{-1}), p (70×10^{-5} TCID_{50}/days·ml) and c (6 days^{-1}).

4.3.2 Zanamivir PK/PD Model

The PK/PD modeling is needed to describe the distribution and effect of antiviral drugs in the host [226]. Pharmacokinetics describes the temporal drug concentration in different organs. One compartment model with a constant drug decay is considered, that is

$$\dot{D}(t) = -\delta_D D(t), \quad D(0) = 0.$$

Here, (D) is the amount of drug available, and δ_D is the drug elimination rate defined by the serum half-life of zanamivir which ranges from 2.5 to 5.1 hours [221, 227]. Here, the mean value is considered, 3.8 hours. The resulting elimination rate is given by $\delta_D = ln(2)/3.8$ hours which is 0.182 hours^{-1} or equivalently 4.37 days^{-1}. On the other hand, pharmacodynamics describes the effect of a drug on the organism. The PD model is

$$\eta = \frac{D(t)}{D(t) + EC_{50z}},$$

which represents the viral inhibition by the treatment [221, 227].

To link the PK/PD model to the system, the viral replication rate p in (4.1) is modified by $p(1-\eta)$, based on the assumption that antiviral therapies mainly affect the replication cycle of the virus [224, 227]. The expressions (4.2)-(4.3) remain unmodified leading to the following drug interaction mode

$$\begin{aligned}\dot{V}(t) &= p\left(1-\frac{D(t)}{D(t)+EC_{50z}}\right)I(t)-cV(t), && (4.4)\\ \dot{D}(t) &= -\delta_D D(t),\ \tau_k \leq t < \tau_{k+1}. && (4.5)\end{aligned}$$

Here, $\tau_k \leq t < \tau_{k+1}$, $\{k = 1, 2, \cdots\}$, are the time intervals between drug intakes, $\tau_{k+1} - \tau_k$ $= 12$ hours. The first drug intake of the treatment is given by $D(\tau_1) = D(t_0) =$ dose (mg).

4.3.3 Oseltamivir PK/PD Model

The PK model describing oseltamivir treatment is given by a two-compartment model [227, 225, 228]. One compartment represents oseltamivir phosphate (OP), while the second one describes its active metabolic compound form, oseltamivir carboxylate (OC). The ordinary differential equations describing the concentrations of OP and OC are [227]

$$\begin{aligned}\dot{G}(t) &= -k_a G(t), && (4.6)\\ \dot{OP}(t) &= k_a G(t) - k_f OP(t), && (4.7)\\ \dot{OC}(t) &= k_f OP(t) - k_e OC(t). && (4.8)\end{aligned}$$

Here, G represents the depot compartment of OP dose administered before the adsorption in the blood with a rate of k_a. The conversion rate from OP to OC is given by k_f, and k_e is the OC elimination rate. The initial values are $G(0)=$ dose, $OP(0) = 0$, and $OC(0) = 0$, the three variables are in mg. Parameter values are k_a (24.24 days^{-1}), k_f (16.41 days^{-1}) and k_e (3.26 days^{-1}). k_a is assumed to be reduced after the first oral dose with a decay rate of 7.31 [228]. The oseltamivir effect (PD) on influenza cycle infection is equivalent to those given in the zanamivir case. Therefore, the oseltamivir PK/PD integrated dynamics are (4.2)-(4.3) and the following

$$\begin{aligned}\dot{V}(t) &= p\left(1-\frac{OC(t)}{OC(t)+EC_{50o}}\right)I(t)-cV(t), && (4.9)\\ \dot{G}(t) &= -k_a G(t),\ \tau_k \leq t < \tau_{k+1} && (4.10)\\ \dot{OP}(t) &= k_a G(t) - k_f OP(t), && (4.11)\\ \dot{OC}(t) &= k_f OP(t) - k_e OC(t), && (4.12)\end{aligned}$$

where τ_k stands for the oral drug intake time of G, with the same time intervals as in the zanamivir treatment.

4.4 Inverse optimal impulsive control schemes

In this section, theoretical bases of the inverse optimal impulsive control techniques are introduced. First, a passivity approach is explored and later a bounded input controller is developed. Results regarding stability, passivity, optimality and boundedness of the impulsive action are presented.

4.4.1 Optimal control and impulsive control – introduction

Consider a general discrete-time nonlinear system with affine input

$$x(k+1) = f(x(k)) + g(x(k))u(k) \quad x_0 = x(0), \tag{4.13}$$

where $x(k)$ is the state of the system at time k, $u(k) \in \Re^m$ is the input and $f : \Re^n \to \Re^n$ and $g : \Re^n \to \Re^{n\times m}$ are smooth functions of the system with $f(0) = 0$. For system 4.13 it is necessary to compute a control law $u(k) = \overline{u}(x(k))$ that minimizes the a cost functional with the following form [194]

$$\begin{aligned} V(x(k)) &= \sum_{n=k}^{\infty} \big(l(x(n)) + u^T(n)Ru(n)\big) \\ &= l(x(k)) + u^T(k)Ru(k) + \sum_{n=k+1}^{\infty} \big(l(x(n)) + u^T(n)Ru(n)\big) \\ &= l(x(k)) + u^T(k)Ru(k) + V(x(k+1)) \end{aligned} \tag{4.14}$$

Function $l : \Re^n \to \Re^+$ is positive semidefinite function and weights the performance of the state vector $x(k)$ and $R : \Re^n \to \Re^{m\times m}$ weights the control efforts according to the state value [194]. In the sense, towards the infinite horizon optimization case, the Bellman's optimality principle (Definition 4.7) can be considered which sets that the value function $V^*(x(k))$ is time invariant and satisfies the discrete-time HJB equation.

$$V^*(x(k)) = \underset{u(k)}{min}\{l(x(k)) + u^T(k)Ru(k) + V^*(x(k+1))\}, \tag{4.15}$$

However, Bellman's principle of optimality also serves as a tool to limit the number of potentially optimal control strategies that must be investigated for solving (4.15). It also implies that optimal control strategies must be determined by working backward from the final stage – the infinite horizon. Thus, the optimal control problem is inherently a backward-in-time problem [198, 229].

Definition 4.7. *Bellman's principle of optimality. An optimal policy has the property that no matter what the previous decision has been (control inputs), the remaining decisions must constitute an optimal policy with regard to the state resulting from those previous decisions [229].*

Towards establishing the conditions that the optimal control law must satisfy, the discrete-time Hamiltonian $\mathcal{H}(x(k), u(k))$ is formulated as follows [230]

$$\mathcal{H}(x(k), u(k)) = l(x(k)) + u(k)^T Ru(k) + V^*(x(k)) - V(x(k)), \tag{4.16}$$

which is used to develop the control law $u(k)$ by calculating

$$\underset{u(k)}{min}\ \mathcal{H}(x(k), u(k)). \tag{4.17}$$

The minimization of (4.17) is achieved with a feedback optimal control law $\overline{u}(x(k))$, which needs to satisfy the necessary condition $\mathcal{H}(x(k), \overline{u}(x(k))) = 0$ [194]. Finally, $\overline{u}(x(k))$ is obtained by calculating the gradient of (4.16) with respect to $u(k)$ [229, 231]. Then, it follows

$$\begin{aligned}\frac{\partial V^*(x(k))}{\partial u(k)} &= \frac{\partial\big(l(x(k)) + u(k)^T R u(k)\big)}{\partial u(k)} + \frac{\partial x(k+1)}{\partial u(k)}\frac{\partial V^*(x(k+1))}{\partial x(k+1)} = 0,\\ &= 2Ru(k) + \big(0 + g^T(k)\big)\frac{\partial V^*(x(k+1))}{\partial x(k+1)},\\ &= 2Ru(k) + g^T(k)\frac{\partial V^*(x(k+1))}{\partial x(k+1)},\end{aligned}$$

and solving for $u(k)$, it follows

$$u(k) = -\frac{1}{2}R^{-1}g^T(k)\frac{\partial V^*(x(k+1))}{\partial x(k+1)}. \tag{4.18}$$

Therefore, (4.18) represents the feedback *optimal control law* [198, 229]. Finally, substituting (4.18) in (4.15), the HJB becomes

$$V^*(x(k)) = l(x(k)) + V^*(x(k+1)) + \frac{1}{4}\frac{\partial V^{*T}(x(k+1))}{\partial x(k+1)}R^{-1}g^T(k)\frac{\partial V^*(x(k+1))}{\partial x(k+1)}. \tag{4.19}$$

Equation (4.19) is the discrete-time HJB equation representing the value function corresponding to the optimal control policy $\overline{u}(x(k))$. However, solving the partial-differential equation structure of (4.19) is not straightforward, highlighting one of the main drawbacks in optimal control systems [198, 194]. To overcome this problem, the inverse optimal control scheme has been previously proposed and extensively developed for discrete-time nonlinear systems [198, 208, 209, 231]. The inverse approach considers the structure of control law (4.18) as the starting point and is considered to seek exponential (global) stability of the equilibrium point $x(k) = 0$ for system (4.13) as well as minimizing a cost functional (4.14), for which $l(x(k)) = -\overline{V}$ with the form $\overline{V} = V(x(k+1)) - V(x(k)) + +u^{*T}(k)Ru^*(k) \leq 0$, where $u^*(k)$ denotes the *inverse optimal control law* [208]. In this sense, the inverse approach is based on the knowledge of $V(x(k))$ which can be defined in such a manner that features characteristics to guarantee stability and minimization instead of solving (4.19). Such a scheme can set properties to $V(x(k))$ taking advantage of concepts such as system stability using a control Lyapunov function or input-output stability with a storing function in passivity systems [212, 231, 232]. Herein, the advantages of the inverse optimal control strategy are considered using the aforegoing stability concepts to develop control laws that meet optimality and minimization, adapted for the impulsive structure.

Impulsive control fulfills the necessity of instantaneously changing the state variables of a system, allowing the control input to be applied at some k-th time steps of a discrete-time system, namely the control instants (τ_k) [12, 215]. The impulsive action modifies the initial condition for the following k-th time-step as follows

$$x(\tau_j^+) = \Delta x(\tau_j)\big|_{k=\tau_j} + x(\tau_j^-), \tag{4.20}$$

$$x(k+1) = f(x(\tau_j^+)), \quad k = \tau_j \tag{4.21}$$

where $x(\tau_j^+)$ is the modified initial condition after the impulsive change and $x(\tau_j^-)$ stands for the state value before the impulsive action. Note that the control action is performed whenever $k = \tau_j$, following the form of (4.20), depicted in Figure 4.6. Moreover, after the state modification, the next k-th state value is calculated by (4.21) using the modified initial condition, $x(\tau_j^+)$. In Figure 4.6, the dashed arrow represents the impulsive change while the dashed-dot arrow indicates the generation of the new state. For simpler notation, the complete process is represented with τ_j, the control instant. Figure 4.6 represents the impulsive action (dashed arrows), the open-loop dynamics (empty circles), and the new initial condition (solid circles) after the impulsive change. In this chapter, the dose intake in the control system is hypothesized as instantaneous incorporation of the drug into the system at a certain time instant with the drug intake while the quantity of the drug is computed using the inverse optimal control approach.

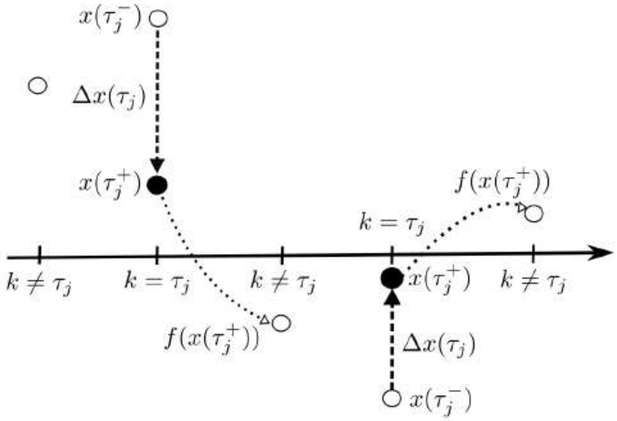

Figure 4.6: Impulsive control action. The intensity of the inverse optimal law $u(\tau_j)$ leads to the state modification $\Delta x(\tau_j)$ (dashed arrow), which moves the state from $x(\tau_j^-)$ to $x(\tau_j^+)$. Afterward, the next k-th state value is computed (dashed-dot arrow). The empty circles stand for the open loop discrete-time system dynamics. The control instants occur when $k = \tau_j$.

4.4.2 Inverse optimal impulsive control with passivity approach

Here, necessary definitions and conditions for each of the employed concepts are set to develop the inverse optimal impulsive framework. The discrete-time impulsively controlled system has the form

$$\begin{aligned} x(k+1) &= f(x(k)),\ x_0 = x(0),\ k \neq \tau_j, && (4.22)\\ \Delta x(\tau_j) &= f(x(\tau_j)) + g(x(\tau_j))u(\tau_j),\ k = \tau_j, && (4.23)\\ y(\tau_j) &= h(x(\tau_j)) + \Gamma(x(\tau_j))u(\tau_j),\ k = \tau_j && (4.24) \end{aligned}$$

where $\tau_j \in S$ are the impulsive control instants. $x(\tau_j) \in \Re^n$ is the state of the system at τ_j, $x(k) \in \Re^n$ is the state of the system in time $k \in \aleph$. The output $y(\tau_j) \in \Re^m$ and the input $u(\tau_j) \in \Re^m$. The functions $f : \Re^n \to \Re^n$, $g : \Re^n \to \Re^{n\times m}$. $h : \Re^n \to \Re^m$ and $\Gamma : \Re^n \to \Re^{m\times m}$ are smooth functions, assuming $h(0) = 0$. $\Delta x(\tau_j)$ is the impulsive change of the state at the control instant τ_j, as depicted in Figure 4.6. When $k \neq \tau_j$ the system (4.22) behaves as at open loop. In addition, the structure of the output (4.24) presents characteristics that support the passivity approach later introduced in this section.

Definition 4.8. *Radially unbounded function [211]. A positive definite function $Q(x(k))$ satisfying the condition $Q(x(k)) \to \infty$ as $\|x(k)\| \to \infty$ is said to be radially unbounded.*

Theorem 4.1. *Asymptotic stability [233]. The equilibrium $x(k) = 0$ of (4.22) is globally asymptotically stable if there is a function $Q : \Re^n \to \Re$ such that (i) Q is a positive definite function and radially unbounded, and (ii) -$\Delta Q(x(x), u(k))$ is a positive definite function.*

Definition 4.9. *Discrete-time control Lyapunov function [234, 13]. Let Q_1 be a radially unbounded, definite positive function, $(Q_1(x(k)) > 0, \forall x(k) \neq 0)$ with $Q_1(0) = 0$. If for any $x(k) \in \Re^n$, there exist real values $u(k)$ such that*

$$\Delta Q_1(x(k), u(k)) < 0, \tag{4.25}$$

where

$$\Delta Q_1(x(k), u(k)) = Q_1\big(f(x(k)) + g(x(k))u(k)\big) - Q_1(x(k)),$$

then $Q_1(\cdot)$ is said to be a discrete-time control Lyapunov function (DTCLF) for (4.22)-(4.23).

For passivity properties, consider the input-output form of the discrete-time impulsively controlled system (4.23)-(4.24), note that according to the passivity approach [11], the output for which the system is passive is not the variable to be controlled, it is only used for control synthesis. The following formal definitions are set and used throughout the chapter.

Definition 4.10. *Passivity. The system (4.23)-(4.24) is said to be passive if there exists a non-negative storage function $Q(x(\tau_j))$, known as storage function, such that for all $u(\tau_j)$,*

$$Q(x(k+1)) - Q(x(\tau_j)) \leq y(\tau_j)^T u(\tau_j), \tag{4.26}$$

this storage function may be selected as a DTCLF if it is a definite positive function [235].

Definition 4.11. *Feedback passive system. The system (4.23)-(4.24) is feedback passive if there exists a control law*

$$u(\tau_j) = \alpha(x(\tau_j)) + v(\tau_j), \;\; \alpha, v \in \Re^m, \tag{4.27}$$

with a smooth function $\alpha(x(\tau_j))$ and a storage function $Q(x(\tau_j))$, such that the system (4.23) with (4.27), represented by

$$\Delta x(\tau_j) \;\; = \;\; \overline{f}(x(\tau_j)) + g(x(\tau_j))v(\tau_j), \tag{4.28}$$

and output

$$\overline{y}(\tau_j) \;\; = \;\; \overline{h}(x(\tau_j)) + \Gamma(x(\tau_j))v(\tau_j), \tag{4.29}$$

satisfies relation (4.26) with $v(\tau_j)$ as the new input [11].

In the feedback passive system approach (Definition 4.11), $\overline{h} : \Re^n \rightarrow \Re^m$ is a smooth mapping, $\overline{h}(x(\tau_j)) = g^T(x(\tau_j))P_Q\overline{f}(x(\tau_j))$, with $\overline{h}(0) = 0$, and P_Q is a positive definite matrix and $\overline{f}(x(\tau_j)) = f(x(\tau_j)) + g(x(\tau_j))\alpha(x(\tau_j))$. Thus, the feedback passive formulation of the system (4.23)-(4.24) can be expressed as finding a passivation law $u(\tau_j)$ and an output $\overline{y}(\tau_j)$ such that relation (4.26) is satisfied with respect to the new input $v(\tau_j)$ [11]. The work [212] presents a discrete-time version of the inverse optimal control framework, here, an extension of this work is developed towards an impulsive approach. To this end, the following theorem is set for the impulsive controlled system (4.23)-(4.24), in which the passivity storage function, $Q(x(\tau_j))$, is employed as a DTCLF.

Theorem 4.2. *Consider the open loop system (4.22) which is bounded at $k \neq \tau_j$, the discrete-time nonlinear system (4.23) and output (4.29), and the control input (4.27), with $\alpha(x(\tau_j))$ given by*

$$\alpha(x(\tau_j)) = -(I_m + \Gamma(x(\tau_j))^{-1}h(x(\tau_j)), \quad k = \tau_j, \tag{4.30}$$

where I_m is the identity matrix of size $m \times m$, with $h(x(\tau_j))$ and $\Gamma(x(\tau_j))$ defined as

$$\begin{aligned} h(x(\tau_j)) &= g^T(x(\tau_j))P_Q f(x(\tau_j)), && (4.31)\\ \Gamma(x(\tau_j)) &= \frac{1}{2}g^T(x(\tau_j))P_Q g(x(\tau_j)). && (4.32)\end{aligned}$$

Consider the DTCLF

$$Q(x(\tau_j)) = \frac{1}{2}x(\tau_j)^T P_Q x(\tau_j), \;\; P_Q = P_Q^T > 0. \tag{4.33}$$

If there exists $P_Q \in P^n$ such that the following inequality holds

$$\Phi(x(\tau_j))^T P_Q \Phi(x(\tau_j)) - x(\tau_j)^T P_Q x(\tau_j) \leqslant 0, \tag{4.34}$$

where $\Phi(x(\tau_j)) = f(x(\tau_j)) + g(x(\tau_j))\alpha(x(\tau_j))$, then the system (4.23) with (4.27) is feedback passive for $\overline{y}(\tau_j)$ in (4.29). In addition, considering $Q(x(\tau_j))$ as a DTCLF, the impulsive control law (4.30) is inverse optimal in the sense that it minimizes the following functional

$$\Im = \sum_{\tau_j=0}^{\infty} L_{\Im}(x(\tau_j), \alpha(x(\tau_j))), \tag{4.35}$$

where

$$L_{\Im}(x(\tau_j), \alpha(x(\tau_j))) = l(x(\tau_j)) + \alpha^T(x(\tau_j))\alpha(x(\tau_j)),$$

$$l(x(\tau_j)) = -\frac{\overline{f}^T(x(\tau_j))P_Q\overline{f}(x(\tau_j)) - x(\tau_j)^T P_Q x(\tau_j)}{2} \geqslant 0,$$

and optimal value function $\Im^* = Q(x(0))$.

Proof. The proof can be found in Apendix B.1.

Corollary 4.1. *For a class of nonlinear systems in which the function $g(x(\tau_j))$ in (4.23) is a constant matrix*

$$g(x(\tau_j)) = B, \tag{4.36}$$

then the solution for P_Q in inequality (4.34) is reduced to the solution of the following inequality

$$\begin{bmatrix} P_Q - 2P_Q B(I_m + \frac{1}{2}B^T P_Q B)^{-2} B^T P_Q & 0 \\ 0 & -P_Q \end{bmatrix} < 0. \tag{4.37}$$

Proof. The complete proof is in Apendix B.1.1

4.4.3 Inverse optimal impulsive control with bounded input

In this subsection, we present the inverse approach using a stabilizing feedback control law which is optimal concerning a cost functional using a CLF candidate. The bounded input properties are integrated into the form of the control law, which is challenged to fulfill conditions for stability and optimality, using the negativity property for the CLF [236, 11]. The discrete-time impulsively controlled system with bounded input has the form

$$\begin{aligned} x(k+1) &= f(x(k)),\ x_0 = x(0),\ k \neq \tau_j, & (4.38)\\ \Delta x(\tau_j) &= f(x(\tau_j)) + g(x(\tau_j))\,\mathrm{sat}(u(\tau_j)),\ k = \tau_j, & (4.39)\\ \mathrm{sat}(u(\tau_j)) &= \min\big(u(\tau_j), u_{max}(\tau_j)\big), & (4.40) \end{aligned}$$

where $\tau_j \in S$ are the impulsive control instants. $x(\tau_j) \in \Re^n$ is the state of the system at τ_j, $x(k) \in \Re^n$ is the state of the system in time $k \in \aleph$. In addition, $f : \Re^n \to \Re^n$, $g : \Re^n \to \Re^{n\times m}$ are smooth functions of the system with the input $u(\tau_j) \in \Re^m$. $\Delta x(\tau_j)$ is the impulsive change of the state at the control instant τ_j, see Fig 4.6. The impulsive action modifies the initial condition for the following k-th time-step as (4.20) - (4.21), where $x(\tau_j^+)$ is the modified initial condition after the impulsive change and $x(\tau_j^-)$ stands for the state value before the impulsive action. First, results for global asymptotic and exponential stability are introduced.

Theorem 4.3. *Global Asymptotic and Exponential Stability [13, 11]. Consider the nonlinear impulsive system (4.38)-(4.39). Suppose there exists a positive definite function $V(x(k)) : \Re^n \to \Re$ satisfying $V(0) = 0$, $V(x(k)) > 0$, $\forall x(k) \neq 0$, $k = \tau_j$ and*

$$V\big(x(k) + f(x(k), u(k))\big) \leq V(x(k)), \tag{4.41}$$

then, the solution $x(k) = 0$ to system (4.38)-(4.39) is Lyapunov stable. In addition, if $V(\cdot)$ is a decreasing positive definite function, radially unbounded, and $-\Delta V(x(k))$ is also a positive definite function, then the solution $x(k) = 0$ is asymptotically stable. Moreover, if there exist scalars $c_1, c_2, c_3 > 0$ and $p \geq 1$ such that

$$\begin{aligned} c_1 \|x(k)\|^p \leq V(x(k)) \leq c_2 \|x(k)\|^p, & \quad (4.42)\\ \Delta V(x(k)) \leq -c_3 \|x(k)\|^p, & \quad (4.43) \end{aligned}$$

and (4.41) holds, then the solution $x(k) = 0$ *is exponentially stable. Finally, if*

$$V(x(k)) \to \infty \quad as \quad \|x(k)\| \to \infty, \tag{4.44}$$

then the above asymptotic and exponential stability results are global.

Acknowledging for Theorem 4.3 and previous studies [13, 65], these results are extended to develop the impulsive framework for discrete-time systems with bounded input, where the boundaries are given as control-design elements. Theorem 4.4 summarizes the results for the controlled system with bounded input (4.38)-(4.39).

Theorem 4.4. *Consider the discrete-time nonlinear impulsively controlled system (4.38)-(4.39), stable at* $k \neq \tau_j$*, with the bounded input (4.40) with* $u(\tau_j)$ *given by*

$$u(x(\tau_j)) = -\frac{1}{2}\big(R + P_2(x(\tau_j))\big)^{-1} P_1(x(\tau_j)),\ k = \tau_j \tag{4.45}$$

where $R : \Re^n \to \Re^{m\times m}$ *and*

$$\begin{aligned} P_1(x(\tau_j)) &= g^T(x(\tau_j)) P_Q\big(x(\tau_j) + f(x(\tau_j))\big), & (4.46)\\ P_2(x(\tau_j)) &= \frac{1}{2} g^T(x(\tau_j)) P_Q g(x(\tau_j)). & (4.47) \end{aligned}$$

Consider also the CLF $V(x(\tau_j))$ *as follows*

$$V(x(\tau_j)) = \frac{1}{2} x(\tau_j)^T P_Q x(\tau_j). \tag{4.48}$$

If there exists a matrix $P_Q = P_Q^T > 0$ *such that the following inequality holds*

$$V_f(x(\tau_j)) - \frac{1}{4} P_1^T(x(\tau_j))\big(R + P_2(x(\tau_j))\big)^{-1} P_1(x(\tau_j)) \leq -\beta_Q \|x(\tau_j)\|^2 \tag{4.49}$$

where $\beta_Q > 0$*, and*

$$\begin{aligned} V_f(x(\tau_j)) &= V\big(x(\tau_j) + f(x(\tau_j))\big) - V(x(\tau_j)) & (4.50)\\ V\big(x(\tau_j) + f(x(\tau_j))\big) &= \frac{1}{2}\big(x(\tau_j) + f(x(\tau_j))\big)^T P_Q \big(x(\tau_j) + f(x(\tau_j))\big), & (4.51) \end{aligned}$$

then the equilibrium point $x(\tau_j) = 0$ *of system (4.38)-(4.39) is globally exponentially stabilized by the impulsive control law (4.45). Moreover, using the CLF (4.48), the impulsive control law is inverse optimal in the sense that it minimizes the following cost functional*

$$V(x(\tau_j)) = \sum_{\tau_j = 0}^{\infty} \big(l(x(\tau_j)) + u^T(\tau_j) R u(\tau_j)\big) \tag{4.52}$$

with

$$l(x(\tau_j) = -\overline{V}\ |_{u^*(\tau_j) = \alpha(x(\tau_j)} \tag{4.53}$$

with the optimal value function $V^*(x(0)) = V(x(0))$*.*

Proof. The proof can be found in Apendix B.2

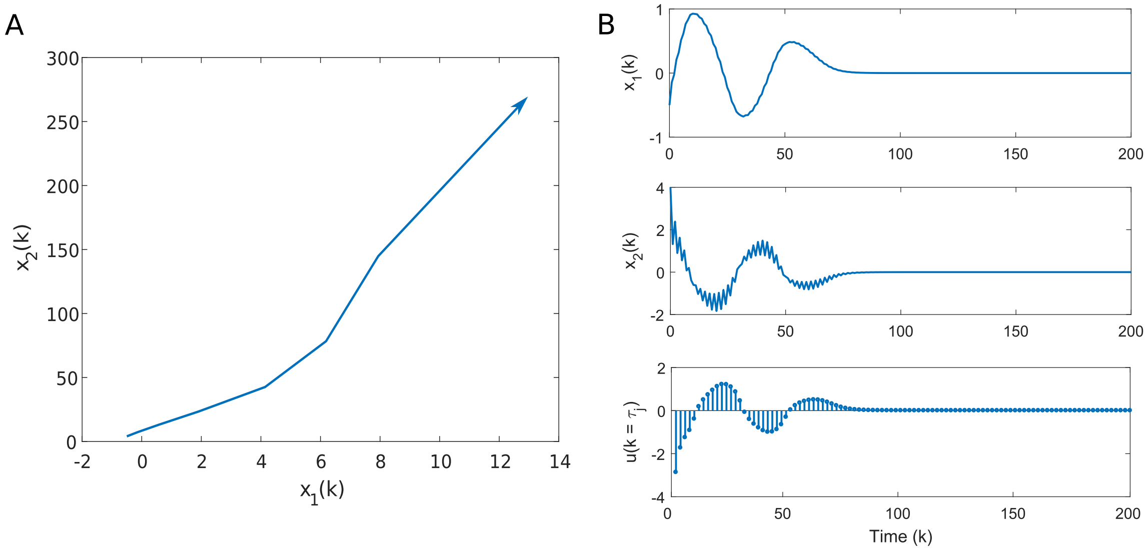

Figure 4.7: Phase portrait of the open-loop system (4.54) and impulsive action. A) open-loop system (4.54). B) System states (top and middle) and impulsive input over time (bottom).

Illustrative example 1

The applicability of Theorem 4.4 results is shown for an impulsively controlled system. Consider the nonlinear discrete-time system [11], unstable for $u(\tau_j) = 0$, following the form of $f(x(k))$ in (4.38) with

$$f(k+1) \quad = \quad \begin{bmatrix} 2.2sin(0.5x_1(k)) + 0.1x_2(k) \\ 0.1x_1(k)^2 + 1.8x_2(k) \end{bmatrix} \tag{4.54}$$

whose phase portrait is shown in Figure 4.7–A and

$$g(x(\tau_j)) \quad = \quad \begin{bmatrix} 0 \\ 2 + 0.1cos(x_2(\tau_j)) \end{bmatrix}, \qquad k = \tau_j. \tag{4.55}$$

Following (4.20), the impulsive modification is given at the control instants $k = \tau_j$, the intensity of the state change is given by the control law (4.45), and the state value for the next k-th step is given following (4.21). For the system (4.54)-(4.55), the control instants perform whenever (k mod 2) = 0, that stands for an impulsive change every two discrete-time system-steps. Note that due to the form of $g(x(\tau_j))$, the control action impulsively modifies solely the state $x_2(k)$ at $k = \tau_j$ as follows

$$x_2(\tau_j^+) \quad = \quad x_2(\tau_j^-) + \big(2 + 0.1cos(x_2(\tau_j))\big)u(\tau_j). \tag{4.56}$$

The initial state vales are $x(0) = [-0.5 \quad 4]$, $\zeta_Q = 1$, and the value for $u_{max} = \pm 4$, therefore, selecting $R = 19.78$ and the matrix P_Q as follows

$$P_Q \quad = \quad \begin{bmatrix} 3.76 & 2.90 \\ 2.90 & 3.76 \end{bmatrix}. \tag{4.57}$$

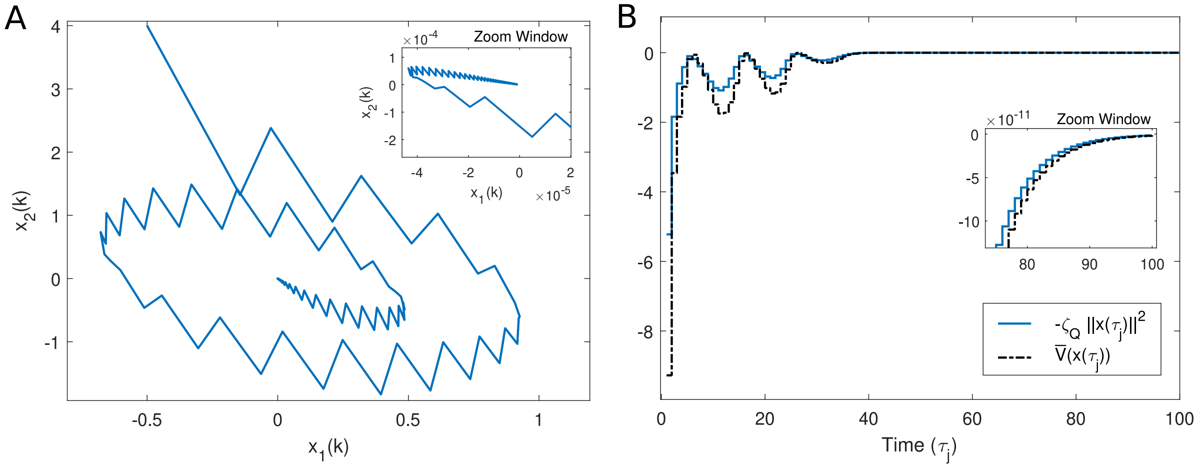

Figure 4.8: Phase portrait and negativity condition of the impulsively controlled system (4.54)-(4.55) (A). B) Negativity condition of inequality (4.49) for the same system. The solid line stands for $-\zeta_Q \left\| x_\tau \right\|^2$ ($\zeta_Q = 1$) and the dash-dotted line is $\overline{V}(x_\tau)$. The zoom windows in both panels highlight details of the stabilizing impulsive shape.

The states of the impulsively controlled system (4.54)-(4.55) as well as the control law shape are depicted in Figure 4.7–B. Note the impulsive effect of state $x_2(k)$ in Figure 4.7–B and the impulsive control law in Figure 4.7–B. In addition, the phase portrait of the controlled system is depicted in Figure 4.8–A, where the impulsive shape can be better perceived. Finally, the condition of inequality (4.49) over time for the system (4.54)-(4.55) is shown in Figure 4.8–B.

4.4.4 Bounded control with positive input

In this section, we explore the developed impulsive framework to systems whose bounded input considers positive values and a maximum positive input u_{pmax}. In a straightforward manner, based on Theorem 4.4, we summarise our results in the following corollary.

Corollary 4.2. *Consider the discrete-time nonlinear impulsively controlled system with bounded input (4.38)-(4.40), with the input $u_p(x(\tau_j))$ at the impulsive instants $k = \tau_j$ as follows*

$$
\begin{aligned}
u_p(x(\tau_j)) &= \left| -\frac{1}{2}\big(R_p + P_2(x(\tau_j))\big)^{-1} P_1(x(\tau_j)) \right|, && (4.58)\\
P_1(x(\tau_j)) &= g^T(x(\tau_j)) P_Q \big(x(\tau_j) + f(x(\tau_j))\big), && (4.59)\\
P_2(x(\tau_j)) &= \frac{1}{2} g^T(x(\tau_j)) P_Q g(x(\tau_j)). && (4.60)
\end{aligned}
$$

where $R_p = |R|$. If there exist the matrix $P_Q = P_Q^T > 0$, then the inequality (4.49) is modified as follows

$$
V_f(x(\tau_j)) + \frac{3}{4} P_1^T(x(\tau_j)) \big(R + P_2(x(\tau_j))\big)^{-1} P_1(x(\tau_j)) \leq -\beta_Q \left\| x(\tau_j) \right\|^2 \qquad (4.61)
$$

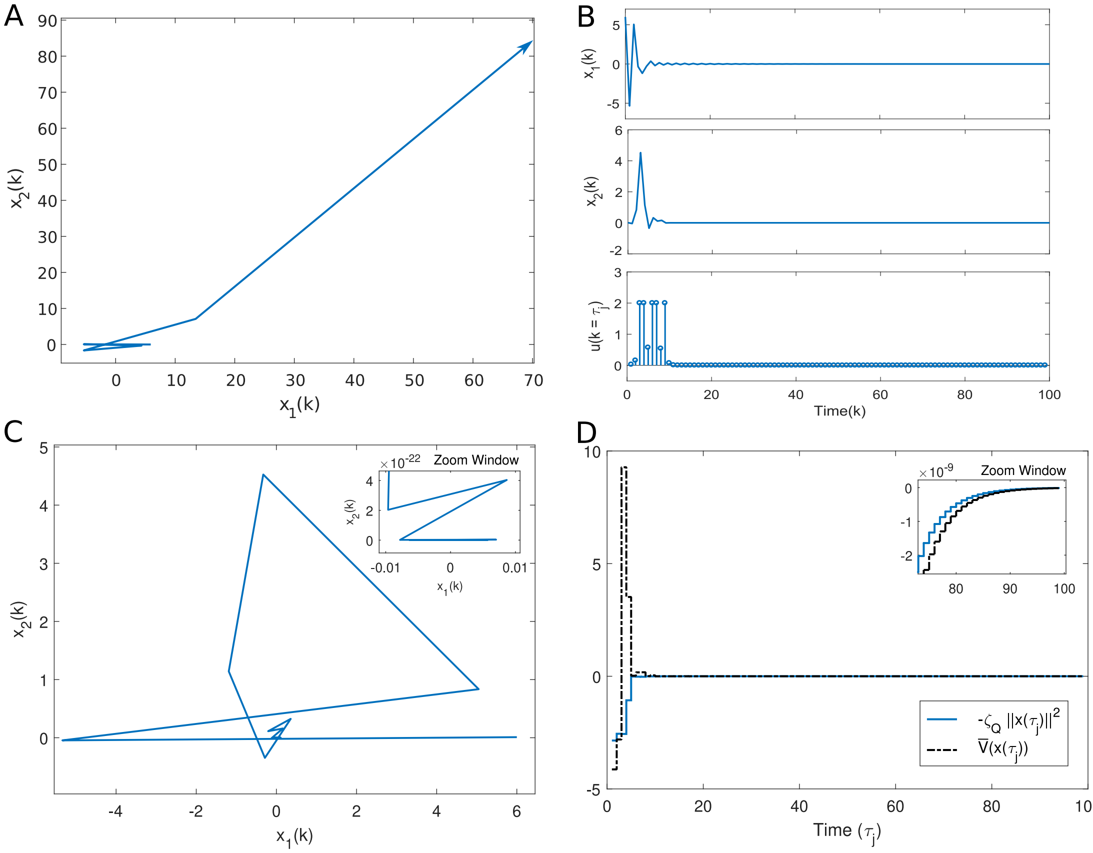

Figure 4.9: Impulsive action for the system (4.62)-(4.63). A) Open loop phase portrait. B) System states (top and middle) and impulsive input over time (bottom). C) Impulsively controlled phase portrait. Note the impulsive effect over the states that leads to system stabilization under a bounded non-negative input of magnitude $u_{pmax} = 2$. The control approach also estimates impulsive modifications of minor magnitude, as those in $k = 5$ and $k = 8$. D) Negativity condition. The solid line stands for $-\zeta_Q \left\| x_\tau \right\|^2$ and the dash-dotted line is $\overline{V}(x_\tau)$. The zoom windows highlight details of the stabilizing impulsive shape.

where $\beta_Q > 0$. The structure of the CLF (4.48), the cost functional (4.52)-(4.53) and the optimal value function remain as in Theorem 4.4.

Proof. The complete proof is in Apendix B.2.1

Illustrative example 2

The applicability of Corollary 4.2 is shown in a general case scenario, consider the following discrete-time system

$$f(k+1) = \begin{bmatrix} x_1(k)x_2(k) - 0.9x_1(k) \\ x_1(k)x_2(k) + x_2(k) \end{bmatrix}, \quad k \neq \tau_j, \tag{4.62}$$

$$g(x(k)) = \begin{bmatrix} 0 \\ 0.8x_1(k) \end{bmatrix}, \quad k \neq \tau_j, \tag{4.63}$$

$$x_2(\tau_j^+) = x_2(\tau_j^-) + \big(0.8x_1(\tau_j)\big)u(\tau_j), \quad k = \tau_j, \tag{4.64}$$

whose initial condition are $x(0) = [6 \quad 0.1]$, a maximum positive input $u_{pmax} = 2$, and the diagonal matrix $P_{Q2} = 0.3\ \mathrm{diag}(1.00)$, $\zeta_{Q2} = 0.1$. Control instants are $\tau_j = k$, $\forall k > 1$. Open loop an impulsive action for the system (4.62)-(4.63) portraits in Figure 4.9.

Finally, it is important to mention that, following heuristic methods, we establish a general starting point with a symmetric positive-definite matrix, *e.g.* a diagonal matrix of one. Next, the negativity condition is tested for the complete horizon, comparing performance indicators such as the treatment efficacy index (4.77) and drug administered, for the case of influenza treatment. The process continues until satisfying conditions on both sides, those of the control law and rather a realistic outcome. The method herein used is a first step regarding the process of finding the values of the matrix P_Q and further studies need to be conducted for recursive methods for the matrix values and conditions to satisfy. The applicability of bounded control schemes in infectious diseases can be found in Refs. [127, 136].

4.5 Treatment tailoring with impulsive action

For the influenza treatment, the FDA (WHO approved) recommends fixed doses of drug administered at fixed time intervals of generally every 12 hours [237, 224]. Thus, the same time intervals to compute the drug amount are considered based on the impulsive control technique. To this end, a discrete-time version of the influenza system is derived using the Euler approximation approach. For the system (4.2)-(4.5), which employs zanamivir, the resulting form is as follows

$$\begin{aligned}
U(k+1) &= U(k) - T\beta U(k)V(k), && (4.65)\\
I(k+1) &= I(k) + T\beta U(k)V(k) - T\delta I(k), && (4.66)\\
V(k+1) &= V(k) + Tp\left(1 - \frac{D(k)}{D(k)+EC_{50z}}\right) I(k) - \ TcV(k), && (4.67)\\
D(k+1) &= D(k) - T\delta_D D(k),\ k \neq \tau_j, && (4.68)\\
D(\tau_j^+) &= U_D(\tau_j) + D(\tau_j^-),\ k = \tau_j, && (4.69)\\
D(k+1) &= D(\tau_j^+) - T\delta_D D(\tau_j^+),\ k = \tau_j, && (4.70)
\end{aligned}$$

where T is the sampling interval and k stands for the time-steps. τ_j are the drug intake instants (inhalation), in this case $\tau_j = j \times 12$ hours, $\{j = 1, 2, \cdots\}$. $U_D(\tau_j)$ denotes the drug amount administered at the instant $k = \tau_j$, adding to the previous drug level $D(\tau_j^-)$. Note that the impulsive input modifies the initial condition $D(\tau_j^+)$ as given by (4.20). In this case, the impulsive modification depicted in Figure 4.6 represents the drug intake, where the dashed arrow refers to (4.69) and the dashed-dot arrow represents (4.70). The drug input $U_D(\tau_j)$ can be given in fixed doses or control-based doses. For the case of oseltamivir, the discrete-time system is given by (4.65)-(4.66) and the following equations

$$\begin{aligned} V(k+1) &= V(k) + Tp\left(1 - \frac{OC(k)}{OC(k) + EC_{50o}}\right) I(k) - \ TcV(k), && (4.71)\\ OP(k+1) &= OP(k) + Tk_a G(k) - Tk_f OP(k), && (4.72)\\ OC(k+1) &= OC(k) + Tk_f OP(k) - Tk_e OC(k), && (4.73)\\ G(k+1) &= G(k) - Tk_a G(k),\ k \neq \tau_j. && (4.74)\\ G(\tau_j^+) &= U_G(\tau_j) + G(\tau_j^-),\ k = \tau_j && (4.75)\\ G(k+1) &= G(\tau_j^+) - Tk_a G(\tau_j^+),\ k = \tau_j. && (4.76) \end{aligned}$$

$U_G(\tau_j)$ is the oseltamivir input given by either fixed doses or control-based doses, depending on the applied technique. Consistently with the impulsive fashion in (4.69), the drug intake is impulsively modified in (4.75) and the following time-step is computed considering the modified drug value in (4.76). The control-based doses for both zanamivir or oseltamivir regimens are defined by the control law $\alpha(x(\tau_j))$ described in the previous subsection. Therefore, the zanamivir amount $U_D(\tau_j)$ in (4.69) and oseltamivir $U_G(\tau_j)$ in (4.75) are calculated with the control law (4.30).

Performance comparison of the control-based framework with respect to the FDA treatment is presented. The initiation time, namely early and delayed treatments, were tested for fixed-doses (FDA approach) and control-based doses. The early and delayed treatments commence at 29 hours post-infection (hpi) and 48 hpi, respectively [220]. For therapy assessment and techniques comparison, it is mandatory to define suitable performance indicators. Therefore, the virological efficacy index (Ψ) is used, defined as

$$\Psi = 100\left(1 - \frac{AUC_c}{AUC}\right)\%, \tag{4.77}$$

where AUC_c represents the area under the virus dynamics V with treatment and AUC is the area under the curve of virus V without treatment [227]. Furthermore, the total drug amount used for different scheduling approaches is registered, which is the sum of all administered doses (mg).

4.5.1 Control-based treatment with zanamivir

The discrete-time zanamivir system (4.65)-(4.70) is represented by the impulsively controlled passive system (4.22)-(4.24) with control law (4.30) modifying the drug amount at each inhalation time $k = \tau_j$.

For numerical simulations, a sampling period of $T = 0.01$ days is assumed. The treatment with zanamivir is until day 5 after infection (day zero). In addition, according to passivity condition (4.26) with the proposed DTCLF function (4.33) it is necessary to select matrix P_Q. In this case, the zanamivir-matrix P_Z is as follows:

$$P_Z = \begin{bmatrix} 1 & 0 & 0 & 0 \\ 0 & 1 & 0 & -10^{-8} \\ 0 & 0 & 1 & -0.5 \\ 0 & -10^{-8} & -0.5 & 1 \end{bmatrix}. \tag{4.78}$$

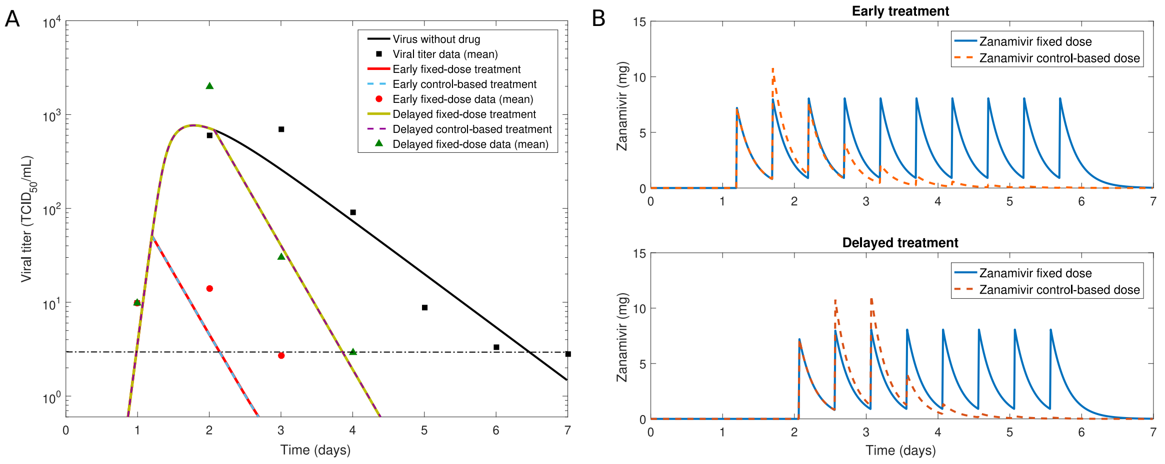

Figure 4.10: Influenza A viral dynamics with zanamivir treatment. A) Treatment results with fixed-dose (7.2 mg) and control-based dose are plotted for early (29 hpi) and delayed (48 hpi) initiation time. The viral load without treatment is also plotted. The viral titter data of the infected patients without treatment and the early and delayed therapies are shown in scatter points [220]. The dash-dot line indicates the limit of viral detection, 3 copies per mL. B) The control-based strategy uses only the first intake fixed to 7.2 mg, the following doses are calculated by the control technique for early and delayed treatment. The solid line shows the fixed-doses and the dashed line the control-based doses. © 2019 IEEE.

The matrix values were tuned manually. The therapy design considers that the control law contemplates the drug state $D(\tau_j)$ as the only one to be modified, thus $B_Z = [0,0,0,1]$. As a result, for the control law design, expressions (4.31) and (4.32) are with $\Gamma_Z = 0.5 \times [0,0,0,1]^T P_Z [0,0,0,1]$, $h_Z(x(\tau_j)) = [0,0,0,1]^T P_Z [f_Z(x(\tau_j))]$, and $f_Z(x(\tau_j))$ stands for the system in equations (4.65)-(4.68). In the control-based case, a threshold of 10 mg is set for overdose prevention. Simulation results in Figure 4.10–A show that the viral inhibition with fixed-dose and control-based dose are practically equal, while the control-based drug doses shown in Figure 4.10–B are significantly lower compared with the fixed-doses. In this case, the efficacy index Ψ in early treatment is 98.15% for the FDA and control-based therapies. However, the total drug amounts are 72 mg and 23.1 mg for fixed-dose and control-based doses, respectively. On the other hand, the delayed treatment efficacy index for FDA and control-based is 35.6%. The drug amounts of 57.6 mg and 24.4 mg are for fixed-doses and controlled doses, respectively. The fixed-dose is with 7.2 mg of zanamivir per inhalation.

4.5.2 Control-based treatment with oseltamivir

For the oseltamivir treatment, the matrix P_Q from (4.33), the selected oseltamivir-matrix P_O is given as follows

$$P_O = \begin{bmatrix} 10 & 0 & 0 & 0 & 0 & 0 \\ 0 & 10 & 0 & 0 & 0 & 0 \\ 0 & 0 & 10 & 0 & 0 & 0 \\ 0 & 0 & 0 & 10 & 0 & -8 \\ 0 & 0 & 0 & 0 & 10 & -0.007 \\ 0 & 0 & 0 & -8 & -0.007 & 10 \end{bmatrix}, \tag{4.79}$$

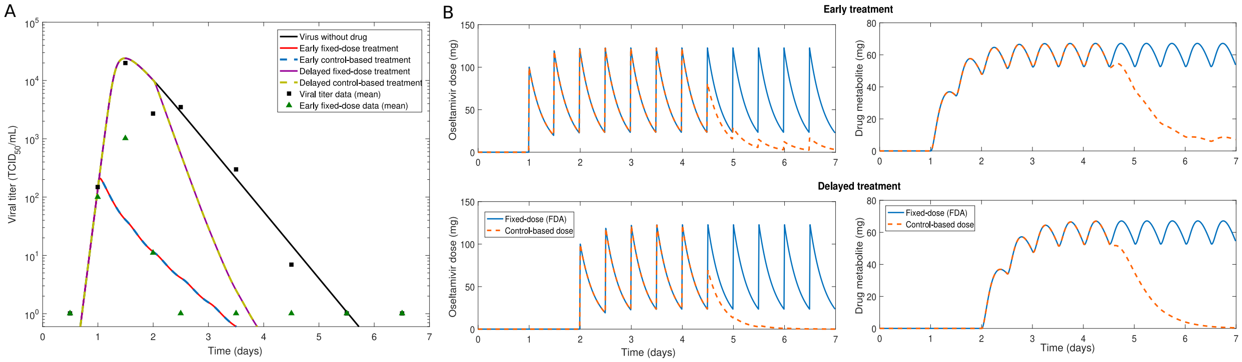

Figure 4.11: Influenza A viral dynamics with oseltamivir treatment. A) Viral load under treatment with fixed-dose (100 mg) and control-based dose, plotted for early (24 hpi) and delayed (48 hpi) initiation time. The viral load without treatment is also plotted. Scatter points depict the viral titter data [223] of patients with early therapy and without treatment. B) Dynamics of oseltamivir depot compartment G (dose) and oseltamivir carboxylate OC (metabolite) at early (top) and delayed (bottom) treatment. The solid line shows the fixed-doses and the dashed line the control-based doses. © 2019 IEEE.

with $B_O = [0,0,0,0,0,1]$, $\Gamma_O = 0.5 \times [0,0,0,0,0,1]^T P_O[0,0,0,0,0,1]$, and $h_O(x(\tau_j)) = [0,0,0,0,0,1]^T P_O[f_O(x(\tau_j))]$, where $f_O(x(\tau_j))$ stands for the system equations with oseltamivir drug. Note that the construction of the matrix P_Q considers the number of states of the system. The matrix values were fine-tuned. In addition, a limit of 100 mg is considered to avoid oseltamivir control-based overdose. The treatment with oseltamivir is until day 7 after infection. Figure 4.11–A shows the viral dynamics under the effect of fixed-doses and control-based doses. The viral elimination in both cases is practically equal, while the amounts of oseltamivir in the control-based strategy portrayed in Figure 4.11–B are clearly lower compared with the FDA fixed-doses.

Using oseltamivir, the efficacy index Ψ in early treatment is 99% in both cases, FDA and control-based. Total drug amounts are 1200 mg and 706 mg for fixed-dose and control-based dose, respectively. On the other hand, for delayed treatments the efficacy index is 12%, employing a total of 1000 mg and 450 mg for fixed-doses and controlled doses, respectively. In addition, Figure 4.11–B draws the behavior of OC during the early and delayed treatments. In both cases, it is easy to notice that the drug metabolite is reduced as a consequence of the adapted doses with the control-based strategy. It is important to remark that the control strategy results with oseltamivir are consistent with zanamivir control outcomes, since the oseltamivir control-based treatment reaches equivalent efficacy compared to the FDA treatment, while the amount of drug is decreased.

4.5.3 Population survey – virtual clinical trial

The Monte Carlo approach is used to evaluate the robustness of the proposed control-based therapy and the FDA (fixed-dose) medication. In the test, parameters and initial conditions of the influenza discrete-time models are selected for zanamivir or oseltamivir. In the case of zanamivir drug, the parameters are represented by $MC_Z = \{U(0),\ V(0),\ EC_{50z},\ p,\ c,\ \beta,\ \delta,\ \delta_D\}$. MC_Z contains the nominal values of each parameter. Oseltamivir parameters are represented by $MC_O = \{U(0),\ V(0),\ EC_{50o},\ p,\ c,\ \beta,\ \delta,\ k_e,\ k_f,\ k_a\}$. At each simulation, each parameter varies with a uniform random distribution within the interval of $\pm 20\% MC$. This range of variation is proposed as a reasonable biological variability range. A total of 1000 simulations per employed drug and initiation time are used. Figure 4.12–A shows the zanamivir efficacy index Ψ and total drug amount behavior in fixed-dose and controlled treatment strategies, considering early and delayed initiation time. Results report the 1000 simulations mean of each therapy by initiation time and an error bar indicates the 95% confidence interval. The mean of the efficacy index of early treatment is 96% for both FDA and controlled therapies. Regarding delayed treatment, the efficacy index average is 38% for fixed and controlled strategies, see Table 4.1. Importantly, although for FDA and control-based therapies the efficacy index average is equal, even for both initiation times, note that the mean of the total zanamivir amounts of control-based strategies is smaller than the mean of fixed-dose treatment. Considering early initiation, the total drug averages for FDA and control-based treatments are 72 mg and 18.4 mg, respectively. Lastly, for delayed treatment, the drug amount averages are 57.6 mg for fixed-dose and 18.5 mg for control-based techniques. The MC results for zanamivir are summarized in Table 4.1. Early and delayed treatments are included for FDA and control-based scheduling techniques.

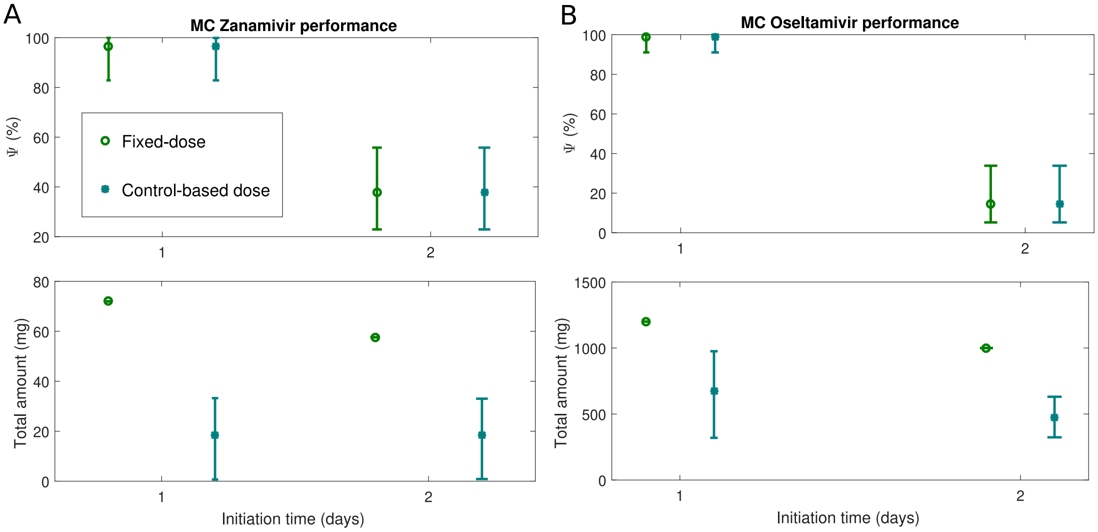

Figure 4.12: Drug performance with a population approach. The mean value of each performance indicator is indicated with an asterisk (control-based) or a circle (fixed-dose) for (A) zanamivir and oseltamivir (B), the error bars are the 95% confidence interval. © 2019 IEEE.

Table 4.1: Zanamivir performance indicators (mean). © 2019 IEEE.

Treatment initiation	**Scheduling technique**	Ψ (%)	**Drug Amount (mg)**
Early	Fixed-dose	96	72
	Control-based		18.4
Delayed	Fixed-dose	38	57.6
	Control-based		18.5

Table 4.2: Oseltamivir performance indicators (mean). © 2019 IEEE.

Treatment initiation	**Scheduling technique**	Ψ (%)	**Drug Amount (mg)**
Early	Fixed-dose	98	1200
	Control-based		673
Delayed	Fixed-dose	14	1000
	Control-based		470

Figure 4.12–B shows MC results of the efficacy index Ψ and drug amount behaviors employing oseltamivir. The early and delayed treatments testing fixed-doses and control-based doses are shown. In a similar manner to the zanamivir case, results report the mean of 1000 simulations per therapy by initiation day and a 95% confidence interval error bars. Moreover, early and delayed treatment results of the total oseltamivir amount for each therapy are reported. The mean efficacy index of the early medication is the same for both, FDA and control-based treatments, that is 98%. Also, the index in delayed treatment is as well equal in both treatments, that is 14%. The mean total drug amount with early treatment is 1200 mg and 673 mg for fixed treatment and control-based doses, respectively. Note that in the MC test, while control-based treatment with oseltamivir reaches the fixed-dose efficacy (98%), there is a drug's quantity reduction of up to 44% (Table 4.2), highlighting the values of the Figure 4.12-B.

4.6 Discussion and schemes for future studies

In this chapter, we explore techniques towards defining optimal feedback control systems in infectious diseases applied to the influenza treatment case as depicted in Figure 2.5. As in a general control system, the infected host with the influenza virus renders the system to be controlled by means of eliminating the viral load, considered as the set point for the control system. We present theoretical results for the stability and optimality of control-based discrete-time impulsive systems. Accounting for mathematical models of influenza dynamics and the PK/PD phases of NIs, treatment scheduling schemes in the form of feedback control are developed which ultimately tailor the dosage in the treatment. Modeling of influenza dynamics is adapted to data from clinical trials with NIs. Concepts for bounded input control are explored with the potential application of overdose prevention. Furthermore, MC surveys highlight the robustness of the proposed treatment scheduling system, and hence it can serve as a development and testing platform for novel treatments, exploring antivirals through PD/PD characteristics as well as host response variability, viral properties, and treatment initiation time, uncovering personalized dosage options.

Regarding future studies, the proposed framework could be used for offline guidance in clinical practice or public health policymakers to determine doses during outbreaks. For real-time applicability, several practical limitations would need to be resolved since measurements are difficult and infrequent [238, 239]. In influenza infection, the most frequently used quantification methods are the titration by plaque assay (plaque-forming units per milliliter of the sample) and the TCID_{50} estimation essay. Both methods are time-consuming, the time needed for visible plaques takes three to five days and the TCID$_{50}$ is finished in two days [36]. This is an important limitation for the implementation of any control framework, which would require the development of time-delay systems observers [240, 241]. A first step to solve these real-world limitations in a practical manner is using learning-based methods such as those on the basis of neural networks. In Chapter 5, we explore recurrent high-order neural networks to estimate the state vector of the unknown influenza and PK/PD model dynamics to develop learning-based neurocontrol strategies for treatment scheduling. We consider that control-based treatment scheduling has implications for other acute infection-like systems, such as COVID-19 but also for long-term treatment, such as HIV treatment for a functional cure. In the case of COVID-19 treatment, control-based strategies could guide optimal dosage when using antivirals or, as recently suggested, immunomodulatory therapies [242, 243, 244].

Chapter 5

Neurocontrol strategies for influenza treatment

In this chapter, lessons learned from impulsive control frameworks in Chapter 4 are taken to develop a neural inverse optimal control – the so-called impulsive neurocontrol. Neurocontrol policies are derived by applying the inverse optimal control into a Recurrent High Order Neural Network (RHONN), trained with the Extended Kalman filter (EKF). The neural network avoids the development of a mathematical model to represent the studied system, serving as a state approximator. For illustration, the proposed neurocontrol is used for personalized treatment with dose tailoring in influenza infection, whose nonlinear model is included and described for completeness. The neurocontrol robustness framework is tested through a virtual clinical trial. *This chapter extends in a didactic manner the partial content of Refs. [37, 239]*[1].

5.1 Introduction

Towards real-world scenarios, a controller based on a system model might not perform as desired due to internal and external disturbances, uncertain parameters, or unmodeled dynamics. An alternative to exhaustive modeling schemes, Recurrent High Order Neural Networks (RHONN) can be used to represent the desired system and present desired characteristics such as the ease of implementation, relatively simple structure, robustness in the presence of disturbances and parameter changes, the capacity to adjust its parameters online, and allows incorporating a priori information about the system structure [38, 39]. Neural networks consist of a number of interconnected processing elements -neurons- and the way in which neurons are interconnected determines their architecture. System identification (Definition 5.1) and control applications usually account for feed-forward and recurrent networks architectures, whose general structure is depicted in Figure 5.2. In the recurrent neural networks,

---

[1] Partial reprint from Ref [37], Gustavo Hernandez-Mejia, Alma Y. Alanis, and Esteban A. Hernandez-Vargas, Neural inverse optimal control for discrete-time impulsive systems, Volume 314, Pages 101-108, Neurocomputing, Copyright (2018), with permission from Elsevier.
Partial reprint from Ref [239], Gustavo Hernandez-Mejia, Esteban A. Hernandez-Vargas, Alma Y. Alanis, and Nancy Arana-Daniel, Recurrent High Order Neural Networks Identification for Infectious Diseases, In 2018 International Joint Conference on Neural Networks (IJCNN) (pp. 1-7). © 2018 IEEE.

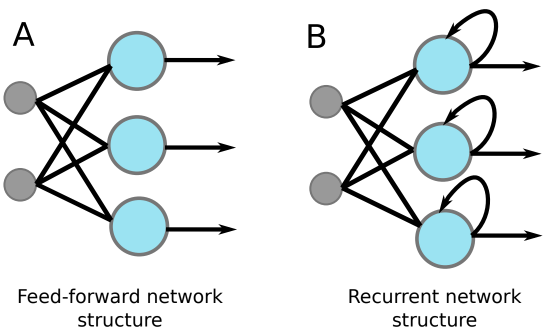

Figure 5.1: Feed-forward and recurrent neural networks architectures. A) In feed-forward neural networks, neurons are organized into layers where signals flow from the input to the output via unidirectional connections. B) For recurrent neural networks (RNN) the outputs of the neuron are feedback to the same neuron or neurons in the preceding layers where signals flow in forward and backward directions. RNN features a high level of interconnection and sigmoid activation functions as the form of the equation (5.5).

the outputs of a neuron are feedback to the same neuron or neurons in the preceding layers where signals flow in forward and backward directions, forming units of internal memory that allow them to be more precise in predicting what is coming in the near future.[14]. Thus, recurrent architectures allow a deeper understanding of time series dynamics applied to system identification while being suitable for control of nonlinear systems applications [41, 42].

Definition 5.1. *System identification. This refers to a methodology for building mathematical models of dynamic systems using measurements of the input and output signals of the system, selecting a model structure, and applying estimation methods for the adjustable parameters in the candidate model structure [245].*

Definition 5.2. *Kalman filtering (KF). In statistics and control theory, Kalman filtering (linear quadratic estimation), is an algorithm that uses a series of measurements observed over time and statistical noise to estimate unknown variables by estimating a joint probability distribution over the variables for each timeframe. The extended Kalman filter (EKF) is the nonlinear version of the KF by linearizing about an estimate of the current mean and covariance [46, 44].*

When using a RHONN as an identification model and adjusting its parameters according to some adaptive law, the response of the RHONN to an input signal should approximate the response of the real system to the same input [43]. However, the main motivation for using RHONN in system identification is that the model described by the RHONN has a physical meaning, that is, for the identification of dynamic systems, the state of each neuron represents a state variable of the system to be identified, which translates in a strong reduction in the number of neurons in the network [246, 14]. It is therefore that the use of RHONNs for modeling schemes with nonlinear dynamics has rapidly increased in recent years [42, 247, 135]. Owing to these features, system identification using RHONNs can be therefore used for control-based schemes that govern, in this case, treatment tailoring, as shown in Figure 5.2. In this approach, the RHONN neural model is trained under learning error minimization to represent the infectious disease and PK/PD models. The control-based dosage system computes the dose according to the neural model, the so-called neurocontroller, which provides the dosage to both, the disease model and the neural model.

Regarding training algorithms, new schemes based on the extended Kalman filter (EKF) (Definition 5.2) have been rising due to different properties. Some of these features are

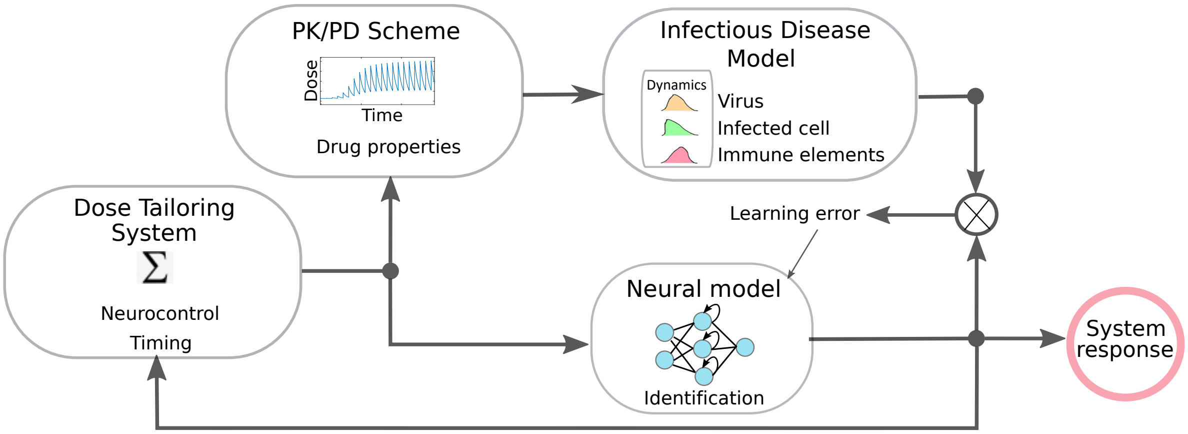

Figure 5.2: Neurocontrol treatment tailoring system. A recurrent neural model is in charge of identifying the dynamics of disease and drug models, on the basis of learning error feedback through a training algorithm (EKF). The neurocontrol tailoring system indicates the dosage for both, the infectious and drug models, and the neural identifier, the last serves as a support for the system response.

important to improve technical issues related to local minima, slow learning rate, high sensitivity to initial conditions, among others [44, 248]. The training problem using EKF theory can be described as finding the minimum mean-squared error estimate of the state -the RHONN weights- using the observed data and the previous estimate. Therefore, the EKF is computationally more efficient than computing the estimate directly from the entire past observed data at each step of the filtering process [46, 44]. RHONN schemes present many convenient features for modeling and control of nonlinear systems [43, 249]. For instance, these networks trained with the EKF, allow reducing the epoch size and the number of required neurons [44, 45]. Discrete-time RHONNs present more interactions among the neurons, the network design is flexible and allows the incorporation of previous information about the system structure into the RHONN model [250, 14]. In addition, the discrete-time neural networks are better fitted for real-time implementations [251]. The RHONN enables identifying the dynamics of the plant to be controlled. Once the weights of the network are adapted, the RHONN model dynamics are similar to the real system dynamics, even in presence of disturbances. As a result, a controller based on the RHONN model can increase its robustness [14].

In this chapter, a neural inverse optimal impulsive control framework is developed for discrete-time systems. The controlled system is identified by the RHONN, which is then used in the control design process. The scheme herein presented is applied to the problem of influenza virus infection treatment. The control policies are based on the discrete-time RHONN to forecast drug amounts for within-host influenza virus infection. The robustness of the impulsive neurocontroler is explored through Monte Carlo simulations, reaching the treatment efficacy of the current FDA (WHO approved) policies with drug saving.

5.2 Neural identification

5.2.1 Recurrent high order neural networks - RHONNs

In this subsection, the identification problem is studied for a general nonlinear system [37, 239]. Consider the following discrete-time system

$$x(k+1) = F(x(k), u(k)), \tag{5.1}$$

where $x\,(k) \in \Re^n$ is the state vector of the system. $u\,(k) \in \Re^m$ is the control input. $F : \Re^n \times \Re^m \to \Re^n$ is a nonlinear function and $k \in \aleph$ is the sampling step. Also, in a recurrent second-order neural network, for instance, the input to the neuron is not only a linear combination of the components (ξ_i), but also of their product ($\xi_i\xi_k$), therefore, it is possible to include higher-order interactions represented by triplets ($\xi_i\xi_k\xi_l$), quadruplets, and so on. This is the forming structure of interconnections in the RHONN. To identify the discrete-time nonlinear system (5.1), assuming a full access to the influenza system states, we use the following series-parallel structure discrete-time RHONN [43, 38]

$$\chi_i(k+1) = \omega_i^T z_i(x(k), u(k)), \tag{5.2}$$

where $i = 1, \ldots, n$. n is the state dimension. $\chi_i(k)$ is the state of the i-th neuron and ω_i is the respective on-line adapted weight vector. $z_i(x(k), u(k))$ is given by

$$z_i(x(k), u(k)) = \begin{pmatrix} z_{i_1} \\ z_{i_2} \\ \vdots \\ z_{i_{L_i}} \end{pmatrix} = \begin{pmatrix} \prod\limits_{j \in I_1} \xi_{i_j}^{d_{i_j}(1)} \\ \prod\limits_{j \in I_2} \xi_{i_j}^{d_{i_j}(2)} \\ \vdots \\ \prod\limits_{j \in I_{L_i}} \xi_{i_j}^{d_{i_j}(L_i)} \end{pmatrix}, \tag{5.3}$$

$$\xi_i = \begin{pmatrix} \xi_{i_1} \\ \vdots \\ \xi_{i_n} \\ \xi_{i_{n+1}} \\ \vdots \\ \xi_{i_{n+m}} \end{pmatrix} = \begin{pmatrix} \varphi(x_1) \\ \vdots \\ \varphi(x_n) \\ u_1 \\ \vdots \\ u_m \end{pmatrix}, \tag{5.4}$$

$$\varphi\,(v) = \frac{1}{1+e^{-av}}, \ a > 0. \tag{5.5}$$

L_i is the respective number of high order connections. m is the number of external inputs. $\{I_1, I_2, ..., I_{L_i}\}$ is a collection of non-ordered subsets of $\{1, ..., n+m\}$, with $d_{ij}(k)$ being a nonnegative integer. $u = \{u_1, u_2, ...u_m\}^T$ in (5.4) is the input vector to the neural network

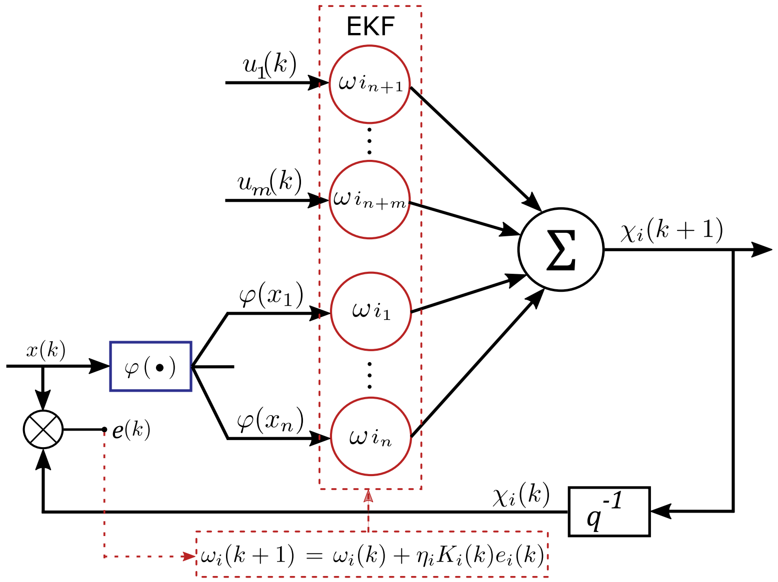

Figure 5.3: RHONN structure diagram. The RHONN given in (5.2) is rendered using the state of the system $x(k)$ and input $u(k)$. The activation function $\varphi(v)$ in (5.5) is represented by the blue-contour box as part of the components of $z_i(x(k), u(k))$ in (5.3) - (5.4), depicted thorugh the flow path of the arrows. Also, the training scheme adapting the weights ω_i using the EKF through (5.6) is highlighted in the RHONN structure with the dashed contours for better visualization. The identification error $e(k)$ follows the difference of the RHONN and system states given in (5.9). Of note, for the neurocontrol scheme, the RHONN states $\chi_i(k)$ are used for computing the control signal.

with $\varphi(\cdot)$ defined by (5.5) where α can be a real value variable [44, 43, 38]. An scheme of the RHONN including the weights adaptation rule is depicted in Figure 5.3. To identify the general discrete-time nonlinear system (5.1) using the RHONN (5.2), consider that $\in_{zi}$ is a bounded approximation error, which can be reduced by increasing the number of the adjustable weights [43].

Assumption 1. There exist an ideal weight vector $\omega_i{}^*$ such that $\|\in_{zi}\|$ can be minimized on a compact set $\Omega_{z_i} \subset \Re^{L_i}$. The ideal weight vector $\omega_i{}^*$ is an artificial quantity for the analysis approach. It is assumed that this vector exists and is constant but unknown [43].

5.2.2 Network training with the extended Kalman filter

The training of a neural network is a process in which the neural network learns a specific task, this training can be online or off-line [252, 40]. The EKF-based training algorithm estimates the neural network weights which become the state of the network. The error between the measured output of the dynamical system and the output of the neural network is considered as additive white noise [250, 40]. The training of RHONN (5.2) is performed online by the EKF-based algorithm, as follows [44]:

$$\omega_i(k+1) = \omega_i(k) + \eta_i K_i(k) e_i(k), \tag{5.6}$$

$$K_i(k) = \rho_i(k) H_i(k) M_i(k), \tag{5.7}$$

$$\rho_i(k+1) = \rho_i(k) - K_i(k) H_i^T(k) \rho_i(k) + Q_i(k) \tag{5.8}$$

where

$$\begin{aligned} M_i(k) &= [\varrho_i(k) + H_i^T(k)\rho_i(k)H_i(k)]^{-1}, \\ e_i(k) &= x_i(k) - \chi_i(k), && (5.9) \\ H_{ij} &= \left[\frac{\partial \chi_i(k)}{\partial \omega_{ij}(k)}\right]^T, && (5.10) \end{aligned}$$

$i = 1, ..., n$ and $j = 1, ..., L_i$. $e_i(k) \in \Re$ is the respective identification error. $\rho_i(k) \in \Re^{L_i \times L_i}$ is the prediction error associated covariance matrix at the step k. $\omega_i \in \Re^{L_i}$ is the weight vector considered as state of the network. $\chi_i(k)$ is the i-th neural network state. $x_i(k)$ is the i-th plant state, n is the number of states. $K_i \in \Re^{L_i}$ is the Kalman gain vector. $Q_i \in \Re^{L_i \times L_i}$ is the state noise associated covariance matrix. $\varrho_i \in \Re$ is the measurement noise associated covariance. $H_i \in \Re^{L_i}$ is a vector, in which each entry H_{ij} is the derivative of one of the neural network states $\chi_i(k)$, with respect to one neural network weight ω_{ij} defined in (5.10). A common practice is that ρ_i and Q_i are initialized as diagonal matrices, with entries $\rho_i(0)$ and $Q_i(0)$, respectively [44]. It is important to remark that for the EKF, $H_i(k)$, $\rho_i(k)$ and $K_i(k)$ are bounded [253]. The stability of a RHONN trained with the EKF to identify a discrete-time nonlinear system has been previously studied [38].

5.3 Inverse optimal impulsive neurocontrol

In this section, inverse optimal neurocontrol policies are presented for a discrete-time impulsive system. Following theoretical concepts from Chapter 4, in a similar manner to system (4.38) - (4.39), and the general definitions of the impulsive fashion of (4.20) - (4.21) in Section 4.4, consider the general discrete-time impulsive dynamical system of the form [37]

$$\begin{aligned} x(k+1) &= f(x(k)),\ x_0 = x(0),\ k \neq \tau_j, && (5.11) \\ \Delta x(\tau_j) &= f(x(\tau_j)) + g(x(\tau_j))u(\tau_j),\ k = \tau_j. && (5.12) \end{aligned}$$

The discrete-time impulsive controlled system (5.11) - (5.12) is identified employing the discrete-time RHONN (5.2). Note that the on-line identification process is independent of the control action and it is performed in every k-th time step. Figure 5.4 shows a diagram of the proposed neurocontrol scheme. Note that the RHONN identification is performed for all k-th time steps, while the impulsive neurocontrol input $u(\tau_k)$ takes action only at $k = \tau_k$. The control law is based on the RHONN states $\chi_i(k)$, later shown in (5.21). The control action guides both the dynamical system and the RHONN.

For the discrete-time RHONN (5.2), considering the impulsive action, the following corollary is defined:

Corollary 5.1. *The discrete-time impulsive neurocontrol has the form*

$$\begin{aligned} \chi_i(k+1) &= \omega_i^T z_i(x(k)),\ k \neq \tau_k, && (5.13) \\ \Delta \chi_i(\tau_k) &= \omega_i^T z_i(x(\tau_k), u(\tau_k)),\ k = \tau_k, && (5.14) \\ \chi_i(k+1) &= \chi_i(\tau_k^+),\ k = \tau_k, && (5.15) \end{aligned}$$

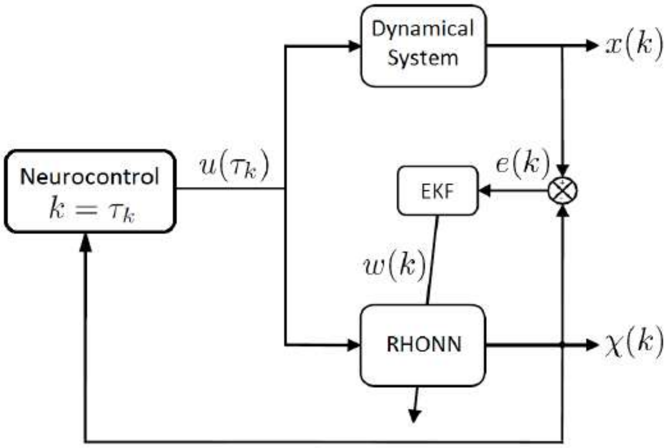

Figure 5.4: Neurocontrol structure diagram. The unknown signal to the RHONN is employed in terms of the system state $x(k)$. Using the EKF, the RHONN identifies states $\chi_i(k)$ as depicted in Figure 5.3. The impulsive neurocontrol modifies both the dynamical system and the RHONN at $k = \tau_k$.

where $k \in \aleph$ *and* $\tau_k \in S$ *are the impulsive control instants, which impulsively modify at least one of the RHONN states in (5.14) over each* τ_k*. The initial conditions for the following time step* $k+1$*, given by* $\chi_i(\tau_k^+)$*, are modified as indicated in (5.15), similarly to Figure 4.6, this time with RHONN state.*

The neurocontrol works with the RHONN identified state $\chi_i(\tau_k)$. The control action is applied to both, the system (5.11) - (5.12) and the RHONN (5.13) - (5.14). Thus, for the control design, using the form of the system (5.11) - (5.12) and the identified state $\chi_i(\tau_k)$, it results as follows

$$\Delta\chi_i(\tau_k) \;=\; f(\chi_i(\tau_k)) + g(\chi_i(\tau_k))u(\tau_k), \quad k = \tau_k. \tag{5.16}$$

For the equation (5.16), based on the inverse optimal control theory [230, 231] and the procedures for Theorem 4.4 and its proof in Apendix B.2, it is desired to determine an impulsive control law $u(\tau_k) = \overline{u}(\chi_i(\tau_k))$ that minimizes the cost functional of the form

$$W(\chi_i(\tau_k)) \;=\; \sum_{n=\tau_k}^{\infty} (l(\chi_i(n)) + u(n)^T R u(n)), \tag{5.17}$$

where $W : \Re^n \to \Re^+$ is a performance measure [194], $l : \Re^n \to \Re^+$ is a positive semidefinite function weighting the performance of the state vector $\chi_i(\tau_k)$, and $R : \Re^n \to P^m$ is a real symmetric and positive definite matrix weighting the control force [194]. For symplicity, the identified state after the impulsive modification is represented as $\chi_i(\tau_k^+)$, then, the equation (5.17) can be expressed as

$$\begin{aligned} W(\chi_i(\tau_k)) \;&=\; l(\chi_i(\tau_k)) + u(\tau_k)^T R u(\tau_k) + \sum_{n=\tau_{k+1}}^{\infty} (l(\chi_i(n)) + u(n)^T R u(n)), \\ &=\; l(\chi_i(\tau_k)) + u(\tau_k)^T R u(\tau_k) + W(\chi_i(\tau_k^+)), \end{aligned} \tag{5.18}$$

which from the optimality principle of Bellman [254, 229], for the infinite horizon optimization case, the value function $W^*(\chi_i(\tau_k))$ becomes invariant in time, considering $l(\chi_i(\tau_k)) := -\overline{W}$, with

$$\overline{W} \;:=\; u(\tau_k)^{*T}Ru(\tau_k)^* + W(\chi_i(\tau_k^+)) - W(\chi_i(\tau_k)) \;\leqslant\; 0. \tag{5.19}$$

Next, a function can be proposed based on $W(\chi_i(\tau_k))$ such that (5.19) is guaranteed. In this way, consider a quadratic CLF such as $W(\chi_i(\tau_k))$ takes the following form

$$W(\chi_i(\tau_k)) \;=\; \frac{1}{2}\chi_i(\tau_k)^T P\chi_i(\tau_k), \;\; P = P^T > 0. \tag{5.20}$$

$W(\chi_i(\tau_k))$ is then applied to the control law. The process to obtain the control law in this case corresponds to the development in Theorem 4.4 and its proof in Apendix B.2. In this sense, the control law $u(\chi_i(\tau_k))$ has the following form

$$\begin{aligned} u(\chi_i(\tau_k)) &= -\frac{1}{2}(R + P_\alpha(\chi_i(\tau_k)))^{-1}P_\beta(\chi_i(\tau_k)), \\ P_\alpha(\chi_i(\tau_k)) &= \frac{1}{2}g^T(\chi_i(\tau_k))Pg(\chi_i(\tau_k)), \\ P_\beta(\chi_i(\tau_k)) &= g^T Pf(\chi_i(\tau_k)). \end{aligned} \tag{5.21}$$

The equation (5.21) is the inverse optimal impulsive neurocontrol law. The neurocontrol law (5.21) establishes the input to the dynamical system (5.11) - (5.12) and the RHONN (5.13) - (5.14) at the instant τ_k. For every other k-th step, the RHONN identification performs without control action, as a free system.

5.4 Neurocontrol application

The proposed neurocontrol scheme in Section 5.3 is applied to the scheduled treatment in IAV infection. Notes on the mathematical models for IAV infection at the host level with the immune response as well as the integration of the neural identifier and the neurocontrol are developed.

5.4.1 Within-host influenza model

In Chapter 4, we use the target-cell model by Baccam *et al.* [10] to develop control-based strategies regarding viral load and the infection of epithelial cells. Although the target-cell model can represent the dynamics of IAV infection without considering the host immune response, the control of the last is key to further explore viral clearance and to better understand the factors shaping the IAV infection course [255, 256]. Besides, previous works using this model raised parameter identifiability issues and the parameter values should be used with caution since parameters can not be estimated in a unique way from the respective experimental data [10, 47, 48].

Regarding immunity, the adaptive response directed by cytotoxic CD8+ T cells and Abs has been investigated in different works, highlighting that CD8+ T cells play an important role in the clearance of the viral infection [255, 257, 258, 181]. The models explore different aspects, such as quantifying the relations between viral replication and adaptive immunity, showing that CD8+ T cells in the lung are as effective as neutralizing Abs for virus clearance when present at the time of challenge [181]. In this direction, due to the identifiability limitations to estimating the parameters in the target-cell model only with viral load data, along with data scarcity, Boianelli *et al.* [49] proposed a minimalistic model able to fit IAV and CD8+ T cells dynamics, which is used in this chapter. The model consists of the virus (V) and the CD8+ T cells (E) dynamics at a host level, depicted in Figure 4.1-B (chapter 4), where the drug dynamics (D) covering two drug PK/PD phases are integrated (not shown in the Figure 4.1-B).

The IAV model is formed with the following differential equations:

$$\begin{aligned}
\dot{E}(t) &= S_E + rE(t)\left(\frac{V(t)}{V(t)+k_e}\right) - c_e E(t), && (5.22)\\
\dot{V}(t) &= p\left(1-\eta\right)V(t)\left(1-\frac{V(t)}{k_v}\right) - c_v V(t)E(t), && (5.23)\\
\dot{D}(t) &= -\delta_D D(t),\ \tau_k \leq t < \tau_{k+1}, && (5.24)
\end{aligned}$$

where $\eta = \frac{D(t)}{D(t)+EC_{50}}$. EC_{50} is the drug concentration level which provides the 50% of drug efficacy. k_v is the maximum carrying capacity of the virus, p is the virus replication rate and the virus is cleared with a rate $c_v E$. The CD8+ T cells constant replenishment rate is $S_E = c_e E(0)$, where c_e is the half-life of CD8+ T cells. $E(0)$ is the initial number of CD8+ T cells and k_e is the half saturation constant of E cells proliferation [49].

Drug intake is given with $\tau_k \leq t < \tau_{k+1}$ indicating the time intervals between drug intakes. This indicates that the first drug intake of the treatment is given by $D(\tau_1) = D(t_0)$. Model parameter values are as follows [49]: r (0.33 days^{-1}), k_e (2.7×10^3 PFU/mL), c_e (2.0×10^{-2} days^{-1}), S_E (2.0×10^4 days^{-1}cells), p (4.4 days^{-1}), k_v (10^6 PFU/mL), c_v (1.24×10^{-6} days^{-1}cells^{-1}). PK/PD parameter values are EC_{50} (42.30 mg) and δ_D (3.26 days^{-1}) [259]. The initial state values are $E(0) = 10^6$ cells, $V(0) = 25$ PFU/mL and $D(0) = 0$ mg.

5.4.2 RHONN for influenza system identification

The system identification is developed considering the IAV model structure in (5.22)-(5.24), as a result, the following discrete-time RHONN is used:

$$\begin{aligned}
\chi_E(k+1) &= \omega_{11}(k)\varphi(x_E(k)) + \omega_{12}(k)\varphi(x_V(k)), && (5.25)\\
\chi_V(k+1) &= \omega_{21}(k)\varphi(x_E(k)) + \omega_{22}(k)\varphi(x_V(k))\varphi(x_D(k)), && (5.26)\\
\chi_D(k+1) &= \omega_{31}(k)\varphi(x_D(k)) + u(k), && (5.27)
\end{aligned}$$

where $\varphi(x)$ has the form of (5.5). Neural weights ω_{ij} are adapted on-line with the EKF-based algorithm in (5.6)-(5.8). In addition, RHONN input $u(k)$ is the drug. As the neural network structure is on discrete-time, variables $x_E(k)$, $x_V(k)$, and $x_D(k)$ stand for the sampled states from the IAV model. The proposed RHONN represents the IAV model, that is, the CD8+ T cells (E) in (5.22) are represented by $\chi_E(k)$ in (5.25), the virus (V) in (5.23) is related to $\chi_V(k)$ in equation (5.26), and the drug (D) in (5.24) is characterized by $\chi_D(k)$ in expression (5.27).

5.4.3 Neurocontrol for influenza treatment

The neural network proposed in the previous subsection is now used for the neurocontrol approach. The impulsively controlled system performs as stated in corollary 5.1, where the equation (5.13) is represented by the neural model (5.25) - (5.27). The control action in (5.14) performs with the neorocontrol law $u(\chi_i(\tau_k)) = \alpha(\chi_i(\tau_k))$ defined in (5.21). The complete expressions are as follow

$$\begin{aligned}
\chi_E(k+1) &= \omega_{11}(k)\varphi(x_E(k)) + \omega_{12}(k)\varphi(x_V(k)),\ k \neq \tau_k, && (5.28)\\
\chi_V(k+1) &= \omega_{21}(k)\varphi(x_E(k)) + \omega_{22}(k)\varphi(x_V(k))\varphi(x_D(k)),\ k \neq \tau_k, && (5.29)\\
\chi_D(k+1) &= \omega_{31}(k)\varphi(x_D(k)),\ k \neq \tau_k, && (5.30)\\
\chi_D(k+1) &= \omega_{31}(k)\varphi(x_D(k)) + u(\chi_i(\tau_k)),\ k = \tau_k, && (5.31)
\end{aligned}$$

where the input to the RHONN is expressed by (5.31) and the unforced part of the system is with equations (5.28) - (5.30). This scheme works as the structure depicted in Figure 5.4.

The neurocontrol law considers the drug state $\chi_D(\tau_k)$ as the only variable to be modified, based on this fact, that is $g = [0, 0, 1]$. As a result, P_α and $P_\beta(\chi_i(\tau_k))$ in (5.21) have the following form

$$\begin{aligned}
P_\alpha &= \frac{1}{2}[0,0,1]^T P[0,0,1],\\
P_\beta(\chi_i(\tau_k)) &= [0,0,1]^T P[\chi_E(\tau_k), \chi_V(\tau_k), \chi_D(\tau_k)],
\end{aligned}$$

with P with the following values

$$P = \begin{bmatrix} 1.0000 & 0.0100 & -0.00003 \\ 0.0100 & 1.0000 & -0.008 \\ -0.00003 & -0.008 & 1.0000 \end{bmatrix}. \qquad (5.32)$$

The EKF associated covariance matrices are initialized as diagonals. The nonzero elements are: $Q_E = Q_V = Q_D = 1 \times 10^6$, $\varrho_E = \varrho_V = \varrho_D = 1 \times 10^4$, $\rho_E = \rho_V = \rho_D = 10$, respectively. The sampling rate of the IAV system for the RHONN identification is $T=$ 0.01 days. Finally, for performance indicators, the virological efficacy index Ψ [227] is used, defined by 4.77 in Section 4.5.

Simulation results show the advantages of neurocontrol over FDA (WHO approved) treatment. For comparison purposes, the FDA treatment is considered, which consists of 75 mg of oseltamivir twice per day [237]. Two initiation days of treatment are tested at day 2 and day 3 after infection. The treatment is active until day 8 after infection. For the neurocontroller, only the first drug intake is fixed to 75 mg, the rest of the doses are calculated by the controller. The mathematical model and RHONN dynamics as well as the identification errors for each case are presented, showing the performance on each scenario. Figure 5.5–A shows the dynamics of the within-host influenza infection and the RHONN dynamics with medication, initiating medication at day 2. Note that the neurocontrol doses are equivalent to those presented by the FDA. This may be attributed to the high viral load at day 2. On the other hand, after day 6, it is notable that the neurocontrol doses are reduced with respect to those by the FDA. In this case, the efficacy indices, FDA ($\Psi =$

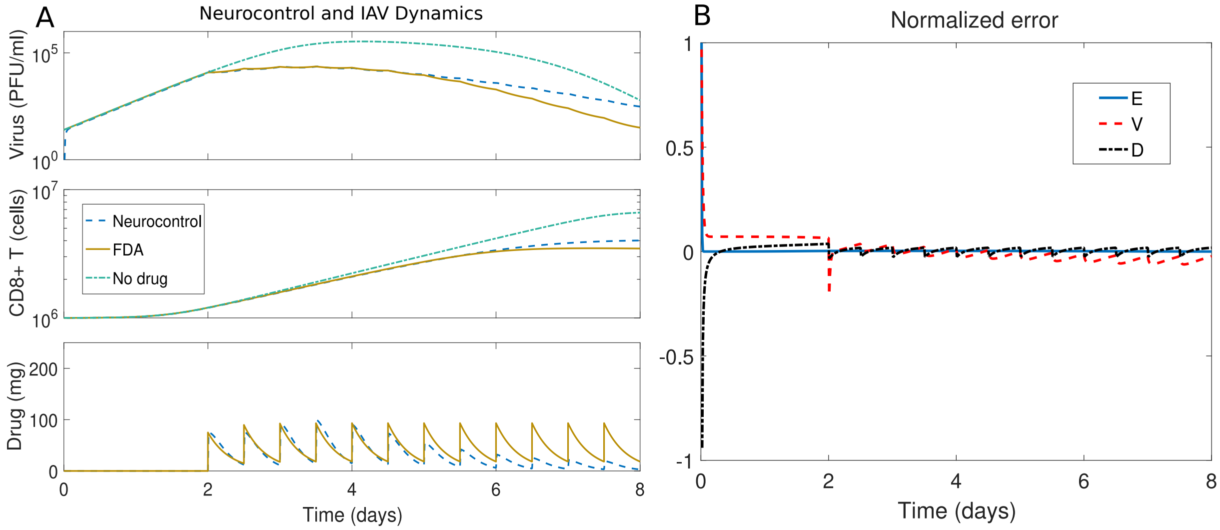

Figure 5.5: IAV dynamics with neurocontrol and FDA doses and identification errors. A) The virus, the immune CD8+ T cells, and drug dynamics. The treatment initiates on day 2. The system without drug input is also plotted. B) Identification errors.

93%) and neurocontrol ($\Psi = 92.37\%$), are slightly different. However, the total amount of drug is different, FDA (900 mg) and neurocontrol (677 mg). In this instance, the proposed neurocontrol performs as the FDA treatment in terms of efficacy, while reducing more than 220 mg of the drug. Due to the differences in scales and in magnitude of each state variable, a normalized error ($\frac{x_i(k)-\chi_i(k)}{x_i(k)}$) is presented in Figure 5.5–B. Note that error fluctuations are more notable in states V and D, which are attributed to the impulsive action of the drug. This behavior is consistent in all drug intake times at τ_k (twice per day) in both the FDA treatment and the neurocontrol.

The treatment initiating at day 3 is depicted in Figure 5.6–A. In this case, the efficacy values (Ψ) are 76% and 70% for neurocontrol and FDA, respectively. The total amount of drug is 827 mg for the neurocontrol and 750 mg for the FDA. Note that neurocontrol can reach higher drug efficacy compared to the FDA recommendations. Also, note that the first treatment doses, those on day 3 and day 4, are higher than FDA doses. In contrast, from day 6 to day 8, neurocontrol doses are fewer than those by the FDA medication. The identification errors for the treatment initiating at day 3 are shown in Figure 5.6–B. The normalized errors are established as in Figure 5.5–B. Note that especially for the D state, the error fluctuation is more notable in correspondence to the drug intake. However, the errors are within the bounds of ± 0.4, which can be considered negligible taking into consideration the magnitude of the variables.

5.4.4 Neurocontrol robustness and virtual clinical trial

In this subsection, results of the proposed neurocontrol performance are shown under a population approach, this framework allows testing the robustness of the neurocontrol. Monte Carlo (MC) simulations are used for treatment initiating at day 1, day 2, and day 3. The neurocontrol comparison is compared to the FDA curative treatment. A set of parameters

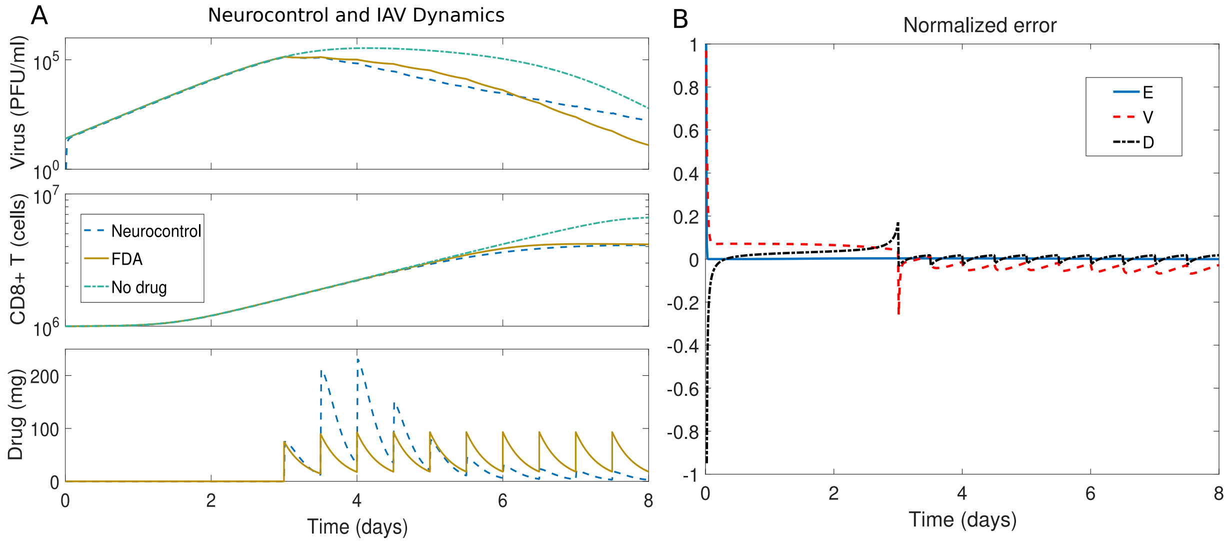

Figure 5.6: IAV dynamics with neurocontrol and FDA doses and identification errors. A) The virus, the immune CD8+ T cells, and drug dynamics. The treatment initiates on day 3. The system without drug input is also plotted. B) Identification errors.

represented by $MC_N = \{E(0), V(0), EC_{50}, \delta_D, p, k_v, c_v, S_E, k_e, c_e\}$ are defined. The values in MC_N were varied with a uniform random distribution within the interval of ±20%. This variation range is assumed as a tolerable biological range. The study considers 1000 simulations per day. Note that the neurocontrol is based on the RHONN states, this may randomly produce high estimation values, affecting the neurocontrol output. Thus, as a preventive measure to avoid an overdose input, a 100 mg dose bound for the neurocontroller is used.

The MC simulation results are depicted in Figure 5.7. The drug efficacy index (Ψ) for each initiation day of treatment and the total amount of the drug are depicted. The mean of 1000 simulations and a 95% confidence interval error bar are depicting the performance of each technique. For the three initiation days, the means of treatment efficacies are slightly different in both, FDA and neurocontrol. On the other hand, the total drug amount means have notable differences. At initiation day 1, the mean efficacy indices are FDA ($\Psi = 96\%$) and neurocontrol ($\Psi = 92\%$), while the mean of total drug amount is FDA (1050 mg) and neurocontrol (642 mg). Note that the difference of drug averages is 408 mg, with the neurocontrol employing less drug than the FDA therapy. In addition, the FDA treatment is only 4% higher than neurocontrol therapy, which is not a highlighting difference. Moreover, the neurocontrol drug confidence interval values are still below the FDA mean, showing that for initiation day 1, the neurocontrol approach reduced the drug input for the overall population scheme.

For the treatment initiating at day 2, the mean efficacy values are FDA ($\Psi = 90\%$) and neurocontrol ($\Psi = 92\%$). The total drug average is 900 mg (FDA) and 606 mg (neurocontrol). Consistently with the scenario of day 1, the neurocontrol drug mean is less than the FDA mean, in this case, with a difference of 294 mg. The neurocontrol can reach a modest higher efficacy than the FDA therapy. For the third scenario, initiating treatment at day 3, the average efficacy is $\Psi = 72\%$ (FDA) and $\Psi = 77\%$ (neurocontrol). The drug means are 750 mg (FDA) and 596 mg (neurocontrol). The average drug difference is 154

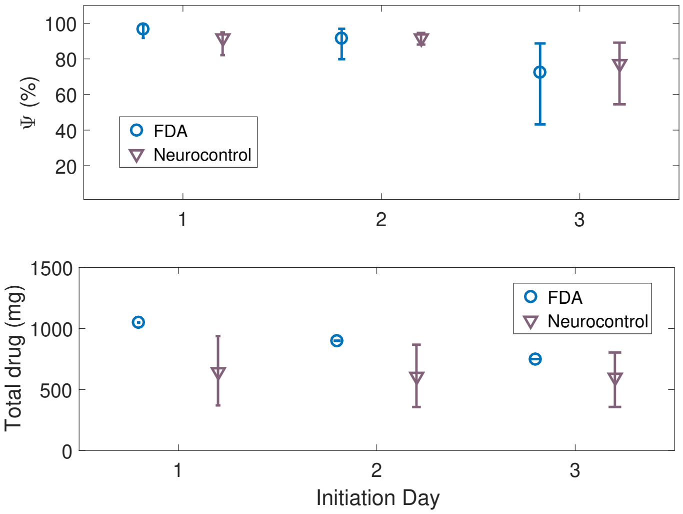

Figure 5.7: Neurocontrol and FDA efficacy indicator (Ψ) and total drug amount. For each initiation day, the mean of the efficacy index and total drug are depicted. The error bars are the 95% confidence interval.

mg. Also, the neurocontrol efficacy is 5% higher than FDA's. Note that in this scenario, the confidence interval of drug efficacy is larger than the first two scenarios. This effect is present in both, the FDA and neurocontrol treatments. However, the neurocontrol efficacy variability (the confidence interval range) is smaller than the variability of the FDA medication. The MC testing allows highlighting the differences between the treatments. For the three initiation days, the mean of neurocontrol doses is smaller than the fixed doses of FDA therapy. Importantly, the efficacy index of FDA treatment is reached by the neurocontrol scheme in all the tested cases. Moreover, the variability of the efficacy is smaller with the neurocontrol, compared to the FDA treatment in the three cases. The neurocontrol shows a robust behavior for the ±20% of parameter variation range and the 1000 simulations per day for the three treatment initiation scenarios tested.

5.5 Discussion and schemes for future studies

In this chapter, an RHONN is trained with the EFK algorithm implemented in an online configuration. The resulting impulsive neurocontrol is employed to calculate the control input for both, the identified dynamical system and the RHONN. Simulations illustrate the effectiveness of the proposed impulsive neurocontrol as applied to a viral infection disease for personalized treatment. Of note, the proposed learning-based methods attempt to guide the first steps towards clinical limitations, such as data scarcity and time-delays in quantification methods [36]. In this direction, further studies are to be integrated for the development of learning-based observers, whose main advantages cover robustness to uncertainties and external disturbances, among others [238, 37]. For the case of viral infection, the authors in Ref. [238] propose a discrete-time recurrent high-order neural Luenberger-like observer for non-linear systems. This observer is based on RHONNs, which can estimate the state vector of the unknown model dynamics with potential extensions to neurocontrol strategies for treatment tailoring. Also, accounting for recent neurocontrol schemes, this has been suggested to be applied in complex networks for controling epidemic models [260]. Lastly, system identification has been explored using high-order sliding mode algorithms that may be subject to internal and external disturbances. In this approach, the neural network weights are trained by means of the unscented Kalman filter and high-order sliding mode observer [261]. The last may finally constitute a possible scheme for combining the impulsive action in treatment.

Finally, regarding the access to disease variables measurements, recent studies explore minimally invasive tools, as methods for monitoring immunological markers in the lungs of the host may be invasive and expensive, and even some of them are not feasible to perform. Using machine learning algorithms, it has been shown that minimally invasively acquired haematological parameters can be used to infer lung viral burden together with other key players such as leukocytes, and cytokines following influenza virus infection in mice [50]. The last may add to the general framework of neurocontrol strategies estimating disease progress with minimally invasive tools. Initially, such a machine learning system could provide a minimum state estimation that inputs the neurocontrol system to perform the treatment.

Chapter 6

Conclusions and final remarks

Motivated by the worldwide public health problem caused by influenza infections, the scientific understanding of host-level mechanisms, and the development of better treatment, Chapters 1 and 2 open diverse backgrounds on the epidemic aspects and nature of the influenza virus, the immune response players, and the particular importance of Abs cross-reaction response to influenza virus. Also, a general view of the current antiviral treatment schemes is introduced, where using the currently recommended drugs, we propose that the incorporation of disciplines such as system biology with data-fitted mathematical models, control theory, learning-based methods, and pharmacological characterization of drugs can lead to optimization of influenza treatment.

The immune response to influenza virus can develop high Abs cross-reaction when having sequential infections, this motivates us to explore modeling schemes that allow better representation the Abs breadth to a diversity of antigens as well as the level of magnitude to such antigens. The main motivation bases on results that highlight the phenomena of Abs cross-reaction between and within influenza groups observed experimental influenza infections in mice and natural infection in humans by Nachbagauer *et al.* [5]. For such a background, in Chapter 3, we integrate diverse modeling schemes previously focused on influenza and HIV infections regarding the antigenic differences, the virus (antigen) representation using the variable and conserved areas of antigen, and the antibody-antigen affinity, where the last is explored to be flexible between sequential infections. This hypothesized scheme highlights that affinity rearrangements between sequential infections may become a condition for affinity and diversity development due to focusing on a certain area of the antigen. The last may follow studies suggesting that a target switch allows initial strain-specific responses to generate cross-reactive descendants for allowing adaptation to new antigen encounters [23].

Clear limitations can be identified in the model. First, the binary representation of the binding site for antigen and Abs may have reduced flexibility to represent different features related to the immunodominance of influenza HA domains such as specific characteristics of the antigenic sites of HA-head and stalk. Further characterization of antigens may be required to give both, the flexibility of antigenic-sites representation and the possibility of Abs response modeling diversification to cover, for instance, Abs to HA-head antigenic sites, HA-stalk and NA. Related schemes have been explored integrating antigenic maps for influenza HA-sites [157], however, broad responses could be tested for different influenza strains of group 1 or 2 of HAs. Second, in a similar direction, the modeling schemes may have antigen-adaptability limitations, for instance, to represent different types of viruses. Since the strings of characters generically represent an antigen, specific modifications should be formulated to portray, for instance, the SARS-CoV-2 proteins for which Abs responses are directed. In the case of influenza, the model features the effects of key mutations which stand in the middle of the antigen string, however, specific characterization of strings to render key amino acid is to be integrated. This may be of particular importance regarding how flexible a string could be since it has been suggested that single amino acid substitutions near the receptor binding site are sufficient to escape from Abs targeting a certain pandemic strain but not from Abs elicited in response to seasonal viruses [262]. Lastly, the model may update to follow the input of observations of the Abs response to different animal models such as guinea pigs, mice, and humans to account for species-specific Abs dynamics [5].

Regarding the incorporation of antigenic and immune response data into the model, a possible line could be also based on previous schemes. Antigenic distance is a well-defined and widely used technique for mapping the differences among antigens, initially on the basis of immunological data and ultimately via sequence-based differences in the antigen [22, 152]. The hypothetical representation of antigens using strings of symbols, which is desired to provide a rather specific input of structural observations from a biological perspective, is a scheme that should be further developed. The metrics that stand for antigen properties characterization may, if possible, mirror key structures that experiments inform as an outcome of broad Abs responses. Finally, we expect that future extensions of the model serve to stepwise construct a solid platform for exploring processes whose antigenic and immune players continue to shed light for understanding Abs cross-reaction to complex antigens, and ultimately inform the design of universal vaccines.

The path towards personalized treatment in infectious diseases is still to be paved, however, pivotal points are explored in Chapter 4 incorporating theoretical bases of control-based treatment scheduling for dose tailoring. A key player relays in the modeling approaches of within-host influenza infection dynamics and the integration of the pharmacologic behavior of the drug to be used. Therefore, we use as a first approach the well-known target-cell limited model to tailor dose regarding the viral load, cell dynamics, and the PK/PD phases of NIs. Accounting for these schemes, classical and novel theoretical bases concerning control-based stability, optimality, and impulsive action can be applied in the form of closed-loop system control. We explore two schemes, first, the input-output approach using the passivity concept of discrete-time systems. Second, we examine the system based on CLF stability, the last accounting for bounded input requirements. In addition, the bounded input approach is extended for positive input schemes. The proposed dose tailoring control-based treatment is challenged with the current fixed-dose FDA recommendations using NIs for individual and population surveys. The results highlight that control-based treatment reaches the efficacy of fixed-dose medication, however, the drug quantity is considerably reduced.

Nevertheless, important limitations remain to be solved. First, online accessibility to viral load measures remains a technology-based problem that ends up being a practical limitation for applicability. In this sense, the solution points to sensing devices that incorporate intelligent manners to measure and estimate biological data. In this direction, we give the first steps towards system identification in Chapter 5, where neurocontrol strategies guide dose tailoring. Second, regarding theoretical bases, the proposed controllers rely on the existence of the positive-definite matrix P_Q, which demands an iterative process to be found and, therefore, may become a limitation for control adaptability. More studies need to be conducted for recursive methods to set this matrix, for instance, going from a discrete-time version of the speed-gradient algorithm to approximation error-based methods, and event-triggered control using dynamic programming [263, 264, 265], adapted to the impulsive scheme. Finally, the impulsive control instants are fixed in the current fashion, which may limit the flexibility for cases with non-equidistant dose timing. In this sense, we need to explore the study of control instants for dose tailoring in cases where the medicament is not given at fixed periods of time. Data scarcity remains a big challenge to validate strategies. Herein, we hypothesize virtual clinical trials using MC methods, however, data from many individuals' treatment is still to be unified. On the other hand, the application of furthermost theoretical frameworks remains to be explored, for instance, the impulsive strategy may incorporate model predictive controllers and positive-systems controllers to test and compare with the proposed one.

Towards solving clinical and practical limitations for applicability such as infrequent and time-consuming measurements, and the fact that a model-based controller might not perform as desired due to internal and external disturbances, or unmodeled dynamics, a very important problem that remains open is the design of identifiers and observers for infectious diseases. In this path, in Chapter 5 we introduce a learning-based system identification framework based on recurrent high order neural networks (RHONN). The RHONN renders the desired system and features ease of implementation and structure, robustness in the presence of disturbances and parameter changes, and allows incorporating a priori information about the system structure. Accounting for the RHONN, the control-based strategies from Chapter 4 are adapted to compute the treatment dose, which is applied to the unknown influenza model. Coupled together, the RHONN and controllers form the proposed impulsive neurocontrol treatment strategies, tested under MC simulations. The development of this type of machinery can lead to another type of controller, the so-called data-driven control. In the last, the process model identification and the controller design are based on real-world data collection. In this sense, the improvement and application of novel approaches of neural networks, optimization algorithms, and other machine learning-based techniques can potentially add solutions for real-world application.

We would like to set some final remarks on control-based and neurocontrol methods. The treatment scheduling has implications for the dose tailoring not only for influenza but for other branches of infectious diseases such as HIV and COVID-19 [266]. Regarding HIV treatment, the combined antiretroviral treatment (cART) may lead to a sterilizing or functional cure, where optimized treatment tailoring can guide dosage to compensate for late treatment initiation or adapt dosage for early treatment when the functional cure is reached [127, 136]. In the case of COVID-19, diverse strategies can be followed from the control-based viewpoint. First, testing treatment optimization of already existing drugs for other diseases as prospects for COVID-19 treatment [267], such as antivirals like Plitidepsin [268], Remdesivir [269], Baloxavir Marboxil and Favipiravir [270], Molnupiravir [271], as well as anti-inflammatory treatments [272, 273], and the combination of them for diverse infection levels and in distinct animal models [274]. On the other hand, in times of pandemic, as already experiencing with COVID-19 vaccine access, antiviral treatment optimization can pave the way of drug availability and accessibility to greater populations through individual treatment tailoring. The saved drug can be better distributed to extend treatment coverage in the population, an approach that in principle can be tested in the form of virtual clinical trials incorporating desired effects such as age-dependent response to infection [275], and comorbidities like cerebrovascular diseases and diabetes [276].

Appendix A

Cross-reaction model supplements

The uncertain level along with the mean is depicted for the set of simulations from the principal test. Figure A.1 depicts the mean of the simulations and a 90% confidence interval between the maximum and minimum values for each antigen Abs dynamics. These plots better reflect, and support, the condition of the affinity threshold between consecutive infections in the following manners, 1) the first infection can be broad in response, however, the magnitude level may greatly vary for those antigens differents from the antigen of infection. For the last one, the magnitude of Abs response is most certain in all cases. 2) After the threshold change, the Abs response becomes remains broad and the magnitude is higher in all antigens, besides, the variability of responses is minor compared to the first infection.

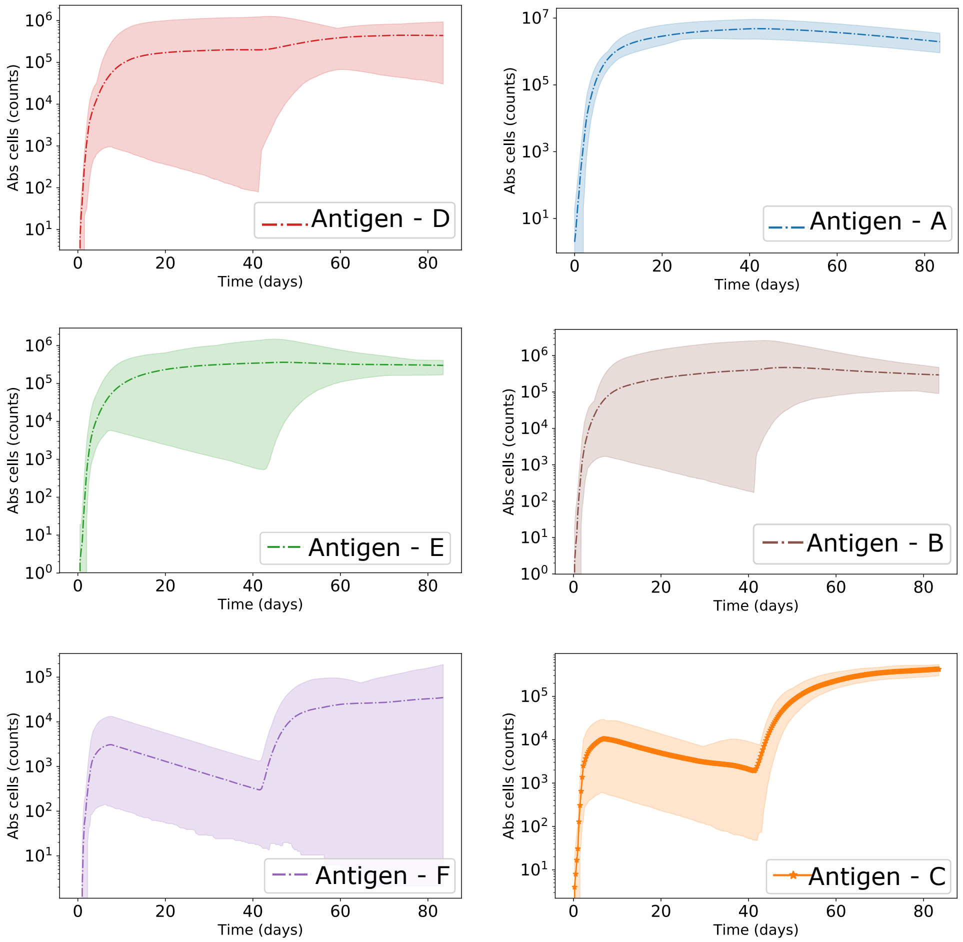

Figure A.1: Mean and 90% confidence interval of Abs responses for the antigens from the principal test.

Appendix B

Proofs of Theorems and Corollaries

B.1 Proof of Theorem 4.2

Regarding the open loop system (4.22) bounded at $k \neq \tau_j$, the corresponding proof for the closed loop system at $k = \tau_j$ is set for conditions of passivity, optimality, and stability.
(i) Passivity: The system (4.23) with input (4.27) and output (4.29) at $k = \tau_j$ must be formulated as feedback passive such that the inequality (4.26) is satisfied, with $v(\tau_j)$ as new input and output $\overline{y}(\tau_j)$ as defined in (4.29). Thus, based on (4.25) and (4.33) it follows

$$\begin{aligned}
&\tfrac{1}{2}\Big[\Big(f(x(\tau_j)) + g(x(\tau_j))\alpha(x(\tau_j))\Big)^T P_Q\Big(f(x(\tau_j)) + g(x(\tau_j))\alpha(x(\tau_j))\Big) - \ x(\tau_j)^T P_Q x(\tau_j)\Big] \\
&+\tfrac{1}{2}\Big[2\Big(f(x(\tau_j)) + g(x(\tau_j))\alpha(x(\tau_j))\Big)^T P_Q g(x(\tau_j))v(\tau_j) + \ v(\tau_j)^T g^T(x(\tau_j))P_Q g(x(\tau_j))v(\tau_j)\Big] \\
&\hfill \leq h_2,
\end{aligned}$$

where $h_2 = \overline{h}^T(\tau_j)v(\tau_j) + v^T(\tau_j)\Gamma^T(x(\tau_j))v(\tau_j)$ with $\alpha(x(\tau_j))$ defined in (4.30). It follows,

$$\begin{aligned}
\Big[\Big(f(x(\tau_j)) + g(x(\tau_j))\alpha(\tau_j)\Big)^T P_Q\Big(f(x(\tau_j)) + g(x(\tau_j))\alpha(\tau_j)\Big)& \\
-x(\tau_j)^T P_Q x(\tau_j)\Big] &\leq 0,
\end{aligned}$$

and $2\big(f(x(\tau_j)) + g(x(\tau_j))\alpha(x(\tau_j))\big)^T P_Q g(x(\tau_j))\ v(\tau_j) = 2\overline{h}^T(x(\tau_j))v(\tau_j)$, then

$$\begin{aligned}
\overline{h}(\tau_j) &= g^T(x(\tau_j))P_Q\big(f(x(\tau_j)) + g(x(\tau_j))\alpha(x(\tau_j))\big), \\
&= g^T(x(\tau_j))P_Q\overline{f}(x(\tau_j)), \qquad \text{(B.1)}
\end{aligned}$$

having

$$v(\tau_j)^T g^T(x(\tau_j))P_Q g(x(\tau_j))v(\tau_j) = 2v^T(\tau_j)\Gamma^T(x(\tau_j))v(\tau_j),$$

from which $\Gamma(x(\tau_j))$ has the form

$$\Gamma(x(\tau_j) = \frac{1}{2}g^T(x(\tau_j))P_Q g(x(\tau_j)). \qquad \text{(B.2)}$$

Next, from expressions (B.1)-(B.2) consider that if the matrix P_Q exists such that satisfies (B.1), then the system (4.23) with (4.27) and (4.29) satisfies inequality (B.1). Hence, it is feedback passive with the DTCLF $Q(x(\tau_j))$ as a storage function and $\overline{h}(\tau_j)$ and $\Gamma(x(\tau_j)$ defined by (B.1) and (B.2), respectively.

(ii) Optimality: This is related to determining a control law $u(\tau_j)$ for the system (4.23) such that an associated cost functional is minimized [229]. Thus, for the system (4.23), let us consider the following cost functional

$$\Im \;=\; \sum_{\tau_j=0}^{\infty} L_{\Im}\big(x(\tau_j), u(x(\tau_j))\big) \tag{B.3}$$

where $L_{\Im}(x(\tau_j), u(x(\tau_j))) = l(x(\tau_j)) + u^T(x(\tau_j))u(x(\tau_j))$ with $l(x(\tau_j))$ a non-negative function [229]. Given a positive definite function $Q : \Re^n \to \Re$, the discrete-time Hamiltonian at $k = \tau_j$ is written as follows

$$\mathcal{H}(x(\tau_j), u(\tau_j)) \;=\; L_{\Im}(x(\tau_j), u(x(\tau_j))) + Q(x(k+1)) - Q(x(\tau_j)).$$

Note that instead of solving exactly for $Q(x(\tau_j))$, the inverse optimality approach is considered [277]. Thus, the control law (4.30) is considered inverse optimal minimizing (4.35) since this control law results from the Hamiltonian (B.4). Calculating $\dfrac{\partial \mathcal{H}(x(\tau_j), u(\tau_j))}{\partial u(\tau_j)} = 0$ one have

$$\begin{aligned}
0 \;&=\; \underset{\alpha(x(\tau_j))}{min}\,\{L_{\Im}(x(\tau_j), \alpha(x(\tau_j))) + Q(x(k+1)) - Q(x(\tau_j))\}\\
&=\; \underset{\alpha(x(\tau_j))}{min}\,\{l(x(\tau_j)) - y^T(\tau_j)\alpha(x(\tau_j)) + Q(x(k+1)) - Q(x(\tau_j))\}\\
&=\; -h^T(x(\tau_j)) - \alpha^T(x(\tau_j))\Big(\Gamma(x(\tau_j)) + \Gamma^T(x(\tau_j))\Big)\\
&\quad\; +\Big(f^T(x(\tau_j)) - y^T(x(\tau_j))g^T(x(\tau_j))\Big)P_Q g(x(\tau_j))\\
&=\; -h^T(x(\tau_j)) - \alpha^T(x(\tau_j))\Big(\Gamma(x(\tau_j)) + \Gamma^T(x(\tau_j))\Big) + f^T(x(\tau_j))P_Q g(x(\tau_j)\\
&\quad\; -y^T(x(\tau_j))g^T(x(\tau_j))P_Q g(x(\tau_j).
\end{aligned} \tag{B.4}$$

Taking $h^T(x(\tau_j)) = f^T(x(\tau_j))P_Q g(x(\tau_j)$, one have

$$\begin{aligned}
0 \;&=\; -\alpha^T(x(\tau_j))\Gamma(x(\tau_j)) - h^T(x(\tau_j))\Gamma(x(\tau_j))\\
&\quad\; -\alpha^T(x(\tau_j))\Gamma^T(x(\tau_j))\Gamma(x(\tau_j)),
\end{aligned} \tag{B.5}$$

then, letting the first and third terms of (B.5) on its right side of the expression, it follows

$$\alpha^T(x(\tau_j))\Big(\Gamma(x(\tau_j)) + \Gamma^T(x(\tau_j))\Gamma(x(\tau_j))\Big) = -h^T(x(\tau_j))\Gamma(x(\tau_j)),$$

equivalently

$$\Big(\Gamma(x(\tau_j)) + \Gamma^T(x(\tau_j))\Gamma(x(\tau_j))\Big)\alpha(x(\tau_j)) = -\Gamma(x(\tau_j))h(x(\tau_j)). \tag{B.6}$$

From (B.2), it is known that $\Gamma(x(\tau_j))$ is a symmetric matrix, and from (B.6) it follows

$$\begin{aligned}
\alpha(x(\tau_j)) &= -\Big[\Big(\Gamma(x(\tau_j)) + \Gamma^T(x(\tau_j))\Gamma(x(\tau_j))\Big)^{-1}\Gamma(x(\tau_j))h(x(\tau_j))\Big], \\
&= -\Big[\Big(\Gamma(x(\tau_j)) + \Gamma(x(\tau_j))\Gamma(x(\tau_j))\Big)^{-1}\Gamma(x(\tau_j))h(x(\tau_j))\Big], \\
&= -\Big[\Big(\Gamma(x(\tau_j))\big(I_m + \Gamma(x(\tau_j))\big)\Big)^{-1}\Gamma(x(\tau_j))h(x(\tau_j))\Big], \\
&= -\Big[\Big(I_m + \Gamma(x(\tau_j))\Big)^{-1}\Gamma(x(\tau_j))^{-1}\Gamma(x(\tau_j))h(x(\tau_j))\Big],
\end{aligned}$$

which becomes

$$\alpha(x(\tau_j)) = -\big(I_m + \Gamma(x(\tau_j))\big)^{-1}h(x(\tau_j)),$$

as defined in (4.30). Next, to calculate the optimal value function ($\Im^*$) for the cost functional (4.35), solving (B.4) for $L_\Im(x(\tau_j), \alpha(x(\tau_j)))$ performing the sum over $[0, N]$, with $N \in S$, it follows

$$\sum_{\tau_j=0}^{N} L_\Im\big(x(\tau_j), \alpha(x(\tau_j))\big) \;=\; -Q(x(N)) + Q(x(0)) + \sum_{\tau_j=0}^{N} \mathcal{H}\big(x(\tau_j), \alpha(x(\tau_j))\big).$$

A necessary condition that the feedback optimal control $\overline{u}(\tau_j)$ must satisfy is $\mathcal{H}\big(x(\tau_j), \overline{u}(x(\tau_j))\big) = 0$ [194]. Thus, for every $k = \tau_j$ one have that $\mathcal{H}\big(x(\tau_j), \alpha(x(\tau_j))\big) = 0$ for the proposed $\alpha(x(\tau_j))$. Let $N \to \infty$ and consequently $Q(x(N)) \to 0$ for every $x(0)$ at $k = \tau_j$, then $\Im^* = Q(x(0))$, known as the optimal value function. As a result, $u(\tau_j) = \alpha(x(\tau_j))$ is an inverse optimal impulsive control law minimizing (4.35) with the performance index $L_\Im\big(x(\tau_j), \alpha(x(\tau_j))\big)$. Note that the control law $\alpha(x(\tau_j))$ is the one employed in the control action. The value of $v(x(\tau_j))$ in (4.27) is only employed for the passive system formulation.

Stability (iii): The closed loop impulsive system (4.23) with input (4.27), it is considered to establish asymptotic stability by the output feedback

$$v(\tau_j) = -\overline{y}(\tau_j) = -\big(I_m + \Gamma(x(\tau_j))\big)^{-1}\overline{h}(x(\tau_j)), \tag{B.7}$$

considering the change $\Delta Q(x(\tau_j))$ as defined in [212], at the impulsive instant $k = \tau_j$, it follows

$$\begin{aligned}
\Delta Q(x(\tau_j)) \;:=\; & \Big[\tfrac{1}{2}\Big(\overline{f}(x(\tau_j)) + g(x(\tau_j))v(\tau_j)\Big)^T P_Q\Big(\overline{f}(x(\tau_j)) + g(x(\tau_j))v(\tau_j)\Big)\Big] \\
& -\tfrac{1}{2}x(\tau_j)^T P_Q x(\tau_j) \\
=\; & \tfrac{1}{2}\Big(\overline{f}^T(x(\tau_j))P_Q\overline{f}(x(\tau_j)) - x(\tau_j)^T P_Q x(\tau_j)\Big) + \overline{f}^T(x(\tau_j))P_Q g(x(\tau_j)v(\tau_j) \\
& +\tfrac{1}{2}v^T(\tau_j)g^T(x(\tau_j))P_Q g(x(\tau_j))v(\tau_j) \\
=\; & \tfrac{1}{2}\Big(\overline{f}^T(x(\tau_j))P_Q\overline{f}(x(\tau_j)) - x(\tau_j)^T P_Q x(\tau_j)\Big) \\
& -\overline{h}^T(x(\tau_j))\big(I_m + \Gamma(x(\tau_j))\big)^{-1}\overline{h}(x(\tau_j)) \\
& +\Big[\overline{h}^T(x(\tau_j))\big(I_m + \Gamma(x(\tau_j))\big)^{-1}\tfrac{1}{2}g^T(x(\tau_j))P_Q g(x(\tau_j)) \\
& \quad \big(I_m + \Gamma(x(\tau_j))\big)^{-1}\overline{h}(x(\tau_j))\Big].
\end{aligned} \tag{B.8}$$

Taking $\Gamma(x(\tau_j)) = (I_m + \Gamma(x(\tau_j))) - I_m$, from (B.8), it follows

$$\begin{aligned}
\Delta Q(x(\tau_j)) \;&=\; \tfrac{1}{2}\Big(\overline{f}^T(x(\tau_j))P_Q\overline{f}(x(\tau_j)) - x(\tau_j)^T P_Q x(\tau_j)\Big) \\
&\quad -\overline{h}^T(x(\tau_j))\big(I_m+\Gamma(x(\tau_j))\big)^{-1}\overline{h}(x(\tau_j)) \\
&\quad +\Big[\overline{h}^T(x(\tau_j))\big(I_m+\Gamma(x(\tau_j))\big)^{-1}(I_m+\Gamma(x(\tau_j))) - I_m \\
&\qquad \big(I_m+\Gamma(x(\tau_j))\big)^{-1}\overline{h}(x(\tau_j))\Big], \\
&=\; \tfrac{1}{2}\Big(\overline{f}^T(x(\tau_j))P_Q\overline{f}(x(\tau_j)) - x(\tau_j)^T P_Q x(\tau_j)\Big) \\
&\quad -\Big[\overline{h}^T(x(\tau_j))\big(I_m+\Gamma(x(\tau_j))\big)^{-2}\overline{h}(x(\tau_j))\Big].
\end{aligned}$$

As set in (B.7) $v(\tau_j) = -\big(I_m + \Gamma(x(\tau_j))\big)^{-1}\overline{h}(x(\tau_j))$, therefore, under condition (B.1) the expression (B.9) becomes

$$\Delta Q(x(\tau_j)) \;=\; \tfrac{1}{2}\Big(\overline{f}^T(x(\tau_j))P_Q\overline{f}(x(\tau_j)) - x(\tau_j)^T P_Q x(\tau_j)\Big) - \|v(\tau_j)\|^2 < 0.$$

Considering the function $Q(x(\tau_j))$ radially unbounded, the solution $x(\tau_j) = 0$ of the closed loop system (4.39), with input (4.27) and output feedback (4.29), present global asymptotic stability.
The proof is complete. ∎

B.1.1 Proof of Corollary 4.1

From control law (4.30), with $h(x(\tau_j))$ and $\Gamma(x(\tau_j))$ as in (4.31) and (4.32), respectively, the left side of equation (4.34) is reduced to

$$\begin{aligned}
&\Big(f(x(\tau_j)) + g(x(\tau_j))\alpha(x(\tau_j))\Big)^T P_Q\Big(f(x(\tau_j)) + g(x(\tau_j))\alpha(x(\tau_j))\Big) - x(\tau_j)^T P_Q x(\tau_j) \\
=\;& f^T(x(\tau_j))P_Q f(x(\tau_j)) + 2\Big(f^T(x(\tau_j))P_Q g(x(\tau_j))\alpha(x(\tau_j))\Big) - x(\tau_j)^T P_Q x(\tau_j) \\
& +\alpha^T(x(\tau_j))g^T(x(\tau_j))P_Q g(x(\tau_j))\alpha(x(\tau_j)) \\
=\;& f^T(x(\tau_j))P_Q f(x(\tau_j)) - x(\tau_j)^T P_Q x(\tau_j) - 2h^T(x(\tau_j))\big(I_m+\Gamma(x(\tau_j))\big)^{-1}h(x(\tau_j)) \\
& +\Big[h^T(x(\tau_j))\big(I_m+\Gamma(x(\tau_j))\big)^{-1}g^T(x(\tau_j))P_Q g(x(\tau_j))\big(I_m+\Gamma(x(\tau_j))\big)^{-1}h(x(\tau_j))\Big]
\end{aligned} \tag{B.9}$$

Expressing $g^T(x(\tau_j))P_Q g(x(\tau_j)) = 2\big(I_m + \Gamma(x(\tau_j))\big) - 2I_m$, from (B.9) it follows

$$\begin{aligned}
& f^T(x(\tau_j))P_Q f(x(\tau_j)) - x(\tau_j)^T P_Q x(\tau_j) - 2h^T(x(\tau_j))\big(I_m+\Gamma(x(\tau_j))\big)^{-1}h(x(\tau_j)) \\
& +\Big[h^T(x(\tau_j))\big(I_m+\Gamma(x(\tau_j))\big)^{-1}\Big(2\big(I_m+\Gamma(x(\tau_j))\big) - 2I_m\Big)\big(I_m+\Gamma(x(\tau_j))\big)^{-1}h(x(\tau_j))\Big] \\
=\;& f^T(x(\tau_j))P_Q f(x(\tau_j)) - x(\tau_j)^T P_Q x(\tau_j) - 2f^T(x(\tau_j))P_Q g(x(\tau_j)\Big[\big(I_m+\Gamma(x(\tau_j))\big)^{-2} \\
& \quad g^T(x(\tau_j))P_Q f(x(\tau_j))\Big].
\end{aligned} \tag{B.10}$$

From condition (4.36), it is considered that (4.34) is satisfied with matrix $P_Q = P_Q^T > 0$, such that (B.10) becomes

$$\begin{aligned}
& f^T(x(\tau_j))P_Q f(x(\tau_j)) - x(\tau_j)^T P_Q x(\tau_j) - 2f^T(x(\tau_j))P_Q B\Big[\big(I_m + \tfrac{1}{2}B^T P_Q B\big)^{-2} \\
& \quad B^T P_Q f(x(\tau_j))\Big] \\
= \; & f^T(x(\tau_j))\Big[P_Q - 2P_Q B\big(I_m + \tfrac{1}{2}B^T P_Q B\big)^{-2} B^T P_Q\Big] f(x(\tau_j)) - x(\tau_j)^T P_Q x(\tau_j) \\
= \; & \big[f(x(\tau_j)) \quad x(\tau_j)\big]^T \begin{bmatrix} P_Q - 2P_Q B(I_m + \frac{1}{2}B^T P_Q B)^{-2} B^T P_Q & 0 \\ 0 & -P_Q \end{bmatrix} \\
& \begin{bmatrix} f(x(\tau_j)) \\ x(\tau_j) \end{bmatrix} < 0 \qquad \text{(B.11)}
\end{aligned}$$

The proof is complete. ■

B.2 Proof of Theorem 4.4

For simplicity, the proof expresses $x(\tau_j)$ as x_τ and functions such as $f(x(\tau_j))$ are notated as $f(x_\tau)$. The corresponding proof for the system (4.38)-(4.39) at $k = \tau_j$ is set for conditions of optimality and stability. The structure of the inverse optimal control law is a direct result of concepts from optimal control, which follows Bellman's optimality principle [229], as next described. For the concept of infinite horizon optimization, the value function $V(x(\tau_j))^*$ becomes time-invariant and satisfies the discrete-time Bellman equation [127, 229, 278, 11], which is known to be solved backwards in time.

$$V(x(\tau_j))^* = \min_{u(\tau_j)}\{l(x(\tau_j)) + u(\tau_j)^T R u(\tau_j) + V(x(\tau_j^+))^*\}. \qquad \text{(B.12)}$$

Next, we set some conditions regarding the optimal control framework that must be satisfied, therefore, we first define the discrete-time Hamiltonian $\mathcal{H}(x(\tau_j), u(\tau_j))$ as follows [277]

$$\mathcal{H}(x(\tau_j), u(\tau_j)) = l(x(\tau_j)) + u(\tau_j)^T R u(\tau_j) + V(x(\tau_j^+))^* - V(x(\tau_j))^*. \qquad \text{(B.13)}$$

A necessary condition that the feedback optimal control law $\overline{u}(\tau_j)$ must satisfy, is the following [194]

$$\mathcal{H}(x(\tau_j), \overline{u}(\tau_j)) = 0. \qquad \text{(B.14)}$$

then $\overline{u}(\tau_j)$ is computed by the gradient of the right-hand side of (B.13), respect to $u(\tau_j)$ [198], using the impulsive change form on $V(x_\tau^+)^* = V\big(x_\tau + f(x_\tau) + g(x_\tau)u(\tau_j)\big)$,

$$\begin{aligned}
0 &= 2Ru(\tau_j) + \frac{\partial V(x_\tau^+)^*}{\partial(u(\tau_j))} && \text{(B.15)} \\
0 &= 2Ru(\tau_j) + g(x_\tau)^T \frac{\partial V(x_\tau^+)^*}{\partial(x_\tau)}. && \text{(B.16)}
\end{aligned}$$

Using (B.16), solving for the inverse form $u(\tau_j)^*$ with the proposed form of the CLF on $V(x_\tau^+)^*$, it follows

$$\begin{aligned}
u(\tau_j)^* &= -\frac{1}{2}R^{-1}g(x_\tau)^T\frac{\partial V(x_\tau^+)^*}{\partial(x_\tau)}, \\
&= -\frac{1}{2}R^{-1}g(x_\tau)^T\frac{\partial\Big(\frac{1}{2}\big(x_\tau+f(x_\tau)+g(x_\tau)u(\tau_j)^*\big)^T P_Q\big(x_\tau+f(x_\tau)+g(x_\tau)u(\tau_j)^*\big)\Big)}{\partial\big(x_\tau+f(x_\tau)+g(x_\tau)u(\tau_j)^*\big)}, \\
&= -\frac{1}{2}R^{-1}g(x_\tau)^T P_Q\big(x_\tau+f(x_\tau)\big)-\frac{1}{2}R^{-1}g(x_\tau)^T P_Q g(x_\tau)u(\tau_j)^*. \qquad \text{(B.17)}
\end{aligned}$$

From (B.17), it follows

$$u(\tau_j)^*+\frac{1}{2}R^{-1}g(x_\tau)^T P_Q g(x_\tau)u(\tau_j)^* = -\frac{1}{2}R^{-1}g(x_\tau)^T P_Q\big(x_\tau+f(x_\tau)\big), \qquad \text{(B.18)}$$

next, (B.18) is multiplied by R,

$$\big(R+\frac{1}{2}g(x_\tau)^T P_Q g(x_\tau)\big)u(\tau_j)^* = -\frac{1}{2}g(x_\tau)^T P_Q\big(x_\tau+f(x_\tau)\big). \qquad \text{(B.19)}$$

Finally, from (B.19), the inverse optimal impulsive control law $u(\tau_j)^*$ can be expressed as

$$\begin{aligned}
u(\tau_j) &= -\frac{1}{2}\big(R+P_1(x_\tau)\big)^{-1}P_2(x_\tau), \qquad \text{(B.20)} \\
P_1(x_\tau) &= \frac{1}{2}g(x_\tau)^T P_Q g(x_\tau), \\
P_2(x_\tau) &= g(x_\tau)^T P_Q\big(x_\tau+f(x_\tau)\big).
\end{aligned}$$

This is how the structure of the control law is designed, the development shown corresponds to the general case of control law (4.45), however, the same approach can be applied to the nonnegative strategy (4.58). For the global stability of the equilibrium point $x(\tau_j)=0$ in the system (4.38)-(4.39), with (4.45) as input, the cost functional (4.35) is achieved satisfying $l(x_\tau) := -\overline{V}$, where

$$\overline{V} \;:=\; V\big(x_\tau+f(x_\tau)+g(x_\tau)\alpha(x_\tau)\big)-V(x_\tau)+u^{*T}(x_\tau)Ru^*(x_\tau)\le 0. \qquad \text{(B.21)}$$

Considering $\alpha(x_\tau) := u^*(x_\tau)$ in (4.53), $\overline{V}$ results in

$$\begin{aligned}
\overline{V} &= V\big(x_\tau+f(x_\tau)+g(x_\tau)\alpha(x_\tau)\big)-V(x_\tau)+\alpha^T(x_\tau)R\alpha(x_\tau), \\
&= \frac{1}{2}\Big[\big(x_\tau+f(x_\tau)\big)^T P_Q\big(x_\tau+f(x_\tau)\big)+2\big(x_\tau+f(x_\tau)\big)^T P_Q g(x_\tau)\alpha(x_\tau) \\
&\qquad +\alpha^T(x_\tau)g^T(x_\tau)P_Q g(x_\tau)\alpha(x_\tau)-x_\tau^T P_Q x_\tau\Big]+\alpha^T(x_\tau)R\alpha(x_\tau), \\
&= V_f(x_\tau)-\frac{1}{2}P_1^T(x_\tau)\big(R+P_2(x_\tau)\big)^{-1}P_1(x_\tau)+\frac{1}{4}P_1^T(x_\tau)\big(R+P_2(x_\tau)\big)^{-1}P_1(x_\tau), \\
&= V_f(x_\tau)-\frac{1}{4}P_1^T(x_\tau)\big(R+P_2(x_\tau)\big)^{-1}P_1(x_\tau). \qquad \text{(B.22)}
\end{aligned}$$

Selecting P_Q such that $\overline{V} < 0$, the stability of $x(\tau_j) = 0$ is guaranteed. The concept of negativity amount is considered for the closed-loop function $\overline{V}$ [236, 11], using the form of (B.22), the negativity amount can be bounded using the auxiliary matrix $Q \in P^n$ as follows

$$\begin{aligned} \overline{V} &= V_f(x_\tau) - \frac{1}{4}P_1^T(x_\tau)\big(R + P_2(x_\tau)\big)^{-1}P_1(x_\tau), \\ &\leq -x_\tau^T Q x_\tau, \\ &\leq -\lambda_{min}(Q)\left\|x_\tau\right\|^2, \\ &= -\zeta_Q \left\|x_\tau\right\|^2, \ \zeta_Q = \lambda_{min}(Q), \ \zeta_Q > 0, \end{aligned} \tag{B.23}$$

where ζ_Q is the minimum eigenvalue of matrix Q, denoted by $\lambda_{min}(Q)$. Therefore, using (B.23), condition (4.49) is satisfied with $\zeta_Q = \beta_Q$. Moreover, taking (B.22)-(B.23)

$$\begin{aligned} \overline{V} &= V\big(x_\tau + f(x_\tau) + g(x_\tau)\alpha(x_\tau)\big) - V(x_\tau) + \alpha^T(x_\tau)R\alpha(x_\tau) \leq -\zeta_Q \left\|x_\tau\right\|^2, \\ \Delta V(x_\tau) &= V\big(x_\tau + f(x_\tau) + g(x_\tau)\alpha(x_\tau)\big) - V(x_\tau) \\ &\leq -\zeta_Q \left\|x_\tau\right\|^2. \end{aligned}$$

Furthermore, as $V(x_\tau)$ is a radially unbounded function, then the solution $x(\tau_j) = 0$ of the closed-loop system (4.38)-(4.39) with (4.45) as input is globally exponentially stable according to Theorem 4.3.

Regarding optimality, considering the function $-l(x_\tau)$ to be the right-hand side of (B.23), if follows

$$\begin{aligned} l(x(\tau_j) &= -\overline{V}\,\big|_{u^*(\tau_j)=\alpha(x_\tau)} \\ &= -V_f(x_\tau) + \frac{1}{4}P_1^T(x_\tau)\big(R + P_2(x_\tau)\big)^{-1}P_1(x_\tau). \end{aligned} \tag{B.24}$$

Thus, to set the optimal value for the cost functional (4.35), one use $l(x_\tau)$ of (B.24) in the cost functional (4.35), giving

$$\begin{aligned} V(x_\tau) &= \sum_{\tau=0}^{\infty}\big(l(x_\tau) + u^T(\tau)Ru(\tau)\big) \\ &= \sum_{\tau=0}^{\infty}\big(-\overline{V} + u^T(\tau)Ru(\tau)\big) \\ &= -\sum_{\tau=0}^{\infty}\Big[V_f(x_\tau) - \frac{1}{4}P_1^T(x_\tau)\big(R + P_2(x_\tau)\big)^{-1}P_1(x_\tau)\Big] + \sum_{\tau=0}^{\infty}u^T(\tau)Ru(\tau) \end{aligned} \tag{B.25}$$

Using $P_1(x_\tau)$ and $P_2(x_\tau)$ as defined in (4.31) and (4.32), respectively, $P_1^T(x_\tau) = \big(x_\tau + f(x_\tau)\big)^T P_Q g(x_\tau)$, and considering the identity matrix $I_m = \big(R + P_2(x_\tau)\big)\big(R + P_2(x_\tau)\big)^{-1}$, from (B.25) it follows

$$\begin{aligned} V(x_\tau) \;=\; & -\sum_{\tau=0}^{\infty}\Big[V_f(x_\tau) - \frac{1}{2}P_1^T(x_\tau)\big(R+P_2(x_\tau)\big)^{-1}P_1(x_\tau) \\ & \qquad + \frac{1}{4}P_1^T(x_\tau)\big(R+P_2(x_\tau)\big)^{-1}P_2(x_\tau)\big(R+P_2(x_\tau)\big)^{-1}P_1(x_\tau) \\ & \qquad + \frac{1}{4}P_1^T(x_\tau)\big(R+P_2(x_\tau)\big)^{-1}R\big(R+P_2(x_\tau)\big)^{-1}P_1(x_\tau)\Big] \\ & + \sum_{\tau=0}^{\infty}u^T(\tau)Ru(\tau). \end{aligned} \tag{B.26}$$

Considering the form of the control law $\alpha(x_\tau) = -\frac{1}{2}\big(R+P_2(x_\tau)\big)^{-1}P_1(x_\tau)$, then (B.26) becomes

$$\begin{aligned} V(x_\tau) \;=\; & -\sum_{\tau=0}^{\infty}\Big[V_f(x_\tau) + P_1^T(x_\tau)\alpha(x_\tau) + \alpha^T(x_\tau)P_2(x_\tau)\alpha_(x_\tau)\Big] \\ & + \sum_{\tau=0}^{\infty}\Big[u^T(\tau)Ru(\tau) - \alpha^T(x_\tau)R\alpha(x_\tau)\Big], \\ =\; & -\sum_{\tau=0}^{\infty}\Big[V\big(x_\tau + f(x_\tau) + g(x_\tau)\alpha(x_\tau)\big) - V(x_\tau)\Big] \\ & + \sum_{\tau=0}^{\infty}\Big[u^T(\tau)Ru(\tau) - \alpha^T(x_\tau)R\alpha(x_\tau)\Big]. \end{aligned} \tag{B.27}$$

With $V_\Delta(x_\tau) = V\big(x_\tau + f(x_\tau) + g(x_\tau)\alpha(x_\tau)\big) - V(x_\tau)$, for the optimal value function $V^*\big(x_\tau, u(\cdot)\big)$, (B.27) becomes

$$V(x_\tau) \;=\; -\sum_{\tau=0}^{\infty}V_\Delta(x_\tau) + \sum_{\tau=0}^{\infty}\Big[u^T(\tau)Ru(\tau) - \alpha^T(x_\tau)R\alpha(x_\tau)\Big]. \tag{B.28}$$

Treating $N \to \infty$ and considering the last two consecutive impulsive instants, that is N and $N-1$, (B.28) becomes

$$V(x_\tau) = -V_\Delta(x_N) + V_\Delta(x_{N-1}) - \sum_{\tau=0}^{N-1}V_\Delta(x_\tau) + \sum_{\tau=0}^{N}\Big[u^T(\tau)Ru(\tau) - \alpha^T(x_\tau)R\alpha(x_\tau)\Big], \tag{B.29}$$

for the next two consecutive instants, it follows

$$\begin{aligned} V(x_\tau) \;=\; & -V_\Delta(x_N) + V_\Delta(x_{N-1}) - V_\Delta(x_{N-1}) + V_\Delta(x_{N-2}) - \sum_{\tau=0}^{N-2}V_\Delta(x_\tau) \\ & + \sum_{\tau=0}^{N}\Big[u^T(\tau)Ru(\tau) - \alpha^T(x_\tau)R\alpha(x_\tau)\Big]. \end{aligned} \tag{B.30}$$

From (B.30) one can note that the terms of the sum of $-V_\Delta(\cdot)$ between consecutive impulsive instants are eliminated, therefore, it follows

$$V(x_\tau) \;=\; -V_\Delta(x_N) + V_\Delta(x_0) + \sum_{\tau=0}^{N}\Big[u^T(\tau)Ru(\tau) - \alpha^T(x_\tau)R\alpha(x_\tau)\Big], \tag{B.31}$$

considering $N \to \infty$ and $V_\Delta(x_N) \to 0$ for all $x(0)$, (B.31) is written as follows

$$V(x_\tau) \;=\; V_\Delta(x_0 + \sum_{\tau=0}^{N}\Big[u^T(\tau)Ru(\tau) - \alpha^T(x_\tau)R\alpha(x_\tau)\Big]. \tag{B.32}$$

Thus, the minimum value of (B.32) is reached with $u(\tau) = \alpha(x_\tau)$. Besides, considering the form of $V_\Delta(x_0)$ with $f_d(x_\tau, \alpha(x_\tau)) = f(x_\tau) + g(x_\tau)\alpha(x_\tau)$ and from equation (4.41) in Theorem 4.3, $V\big(x_0 + f_d(x_0, \alpha(x_0))\big) \leq V(x_0)$, it follows that the optimal value function of (4.35) is $V^*\big(x_\tau\big) = V(x_0)$ for all x_0.

The constraining value of $u_{max}(\tau_j)$ is incorporated in terms of R in (4.45) as follows

$$\begin{aligned} 2u_{max}(\tau_j) &= -\big(R + P_2(x_\tau)\big)^{-1}P_1(x_\tau), \\ 2\big(R + P_2(x_\tau)\big)u_{max}(\tau_j) &= -P_1(x_\tau), \\ 2Ru_{max}(\tau_j) &= -\big(P_1(x_\tau) + 2P_2(x_\tau)u_{max}(\tau_j)\big). \end{aligned} \tag{B.33}$$

For a given u_{max}, The value of R in (B.33) is given by

$$R \;=\; -\frac{1}{2}\left[\frac{P_1(x_\tau) + 2P_2(x_\tau)u_{max}}{u_{max}}\right]. \tag{B.34}$$

The proof is complete. ■

B.2.1 Proof of Corollary 4.2

Consider the function $l(x_\tau) := -\overline{V}$ in (B.21), $V_f(x_\tau)$ with (4.50)-(4.51) and the input structure (4.58) with $\alpha_p(x_\tau) := u_p^*(x_\tau)$, using the evenness property $\big(|-z| = |z|\big)$ of the absolute value and the development in (B.22), it follows

$$\begin{aligned} \overline{V} &= V\big(x_\tau + f(x_\tau) + g(x_\tau)\alpha_p(x_\tau)\big) - V(x_\tau) + \alpha_p^T(x_\tau)R_p\alpha_p(x_\tau), \\ &= V_f(x_\tau) + \frac{1}{2}P_1^T(x_\tau)\big(R_p + P_2(x_\tau)\big)^{-1}P_1(x_\tau) + \frac{1}{4}P_1^T(x_\tau)\big(R_p + P_2(x_\tau)\big)^{-1}P_1(x_\tau), \\ &= V_f(x_\tau) + \frac{3}{4}P_1^T(x_\tau)\big(R_p + P_2(x_\tau)\big)^{-1}P_1(x_\tau) \end{aligned} \tag{B.35}$$

where $P_1(x_\tau)$ and $P_2(x_\tau)$ remain as defined in (4.31) and (4.32), respectively. Besides, the negativity amount properties with the auxiliary matrix $Q \in P^n$ of (B.23), with $-\zeta_Q \left\|x_\tau\right\|^2$, $\zeta_Q = \lambda_{min}(Q)$, $\zeta_Q > 0$, directly apply to (B.35).

Regarding optimality, the function (B.24) becomes

$$\begin{aligned} l(x(\tau_j) &= -\overline{V}\,\big|_{u_p^*(\tau_j)=\alpha_p(x_\tau)} \qquad \text{(B.36)} \\ &= -\Big[V_f(x_\tau) + \frac{3}{4}P_1^T(x_\tau)\big(R_p + P_2(x_\tau)\big)^{-1}P_1(x_\tau)\Big], \end{aligned}$$

therefore, the optimal value function $V^*\big(x_\tau, u_p(\cdot)\big)$ is now expressed as

$$V(x_\tau) \;=\; -\sum_{\tau=0}^{\infty} V_\Delta(x_\tau) + \sum_{\tau=0}^{\infty}\Big[u_p^T(\tau)R_p u_p(\tau) - \alpha_p^T(x_\tau)R_p\alpha_p(x_\tau)\Big], \tag{B.37}$$

with $V_\Delta(x_\tau) = V\big(x_\tau + f(x_\tau) + g(x_\tau)\alpha_p(x_\tau)\big) - V(x_\tau)$, which validity holds following a similar development of that in (B.25)-(B.27). Moreover, the existence of the optimal value function $V^*\big(x_\tau\big) = V(x_0)$ for all x_0 is ensured with $f_d(x_\tau, \alpha_p(x_\tau)) = f(x_\tau) + g(x_\tau)\alpha_p(x_\tau)$ and $V\big(x_0 + f_d(x_0, \alpha_p(x_0))\big) \leq V(x_0)$ from Theorem 4.3. Finally, for a given bounded positive input u_{pmax}, the value of R_p in (4.58) is given by

$$R_p \;=\; \left|-\frac{1}{2}\left[\frac{P_1(x_\tau) + 2P_2(x_\tau)u_{pmax}}{u_{pmax}}\right]\right|. \tag{B.38}$$

The proof is complete. ■

Bibliography

[1] WHO, “World Health Organization. Influenza (Seasonal) fact sheet 2018.,” *Online-https://www.who.int/news-room/fact-sheets/detail/influenza-(seasonal). Accessed-February 2020.*, 2018.

[2] F. Krammer, G. J. Smith, R. A. Fouchier, M. Peiris, K. Kedzierska, P. C. Doherty, P. Palese, M. L. Shaw, J. Treanor, R. G. Webster, *et al.*, “Influenza (primer),” *Nature Reviews: Disease Primers*, 2018.

[3] J. Wrammert, K. Smith, J. Miller, W. A. Langley, K. Kokko, C. Larsen, N.-Y. Zheng, I. Mays, L. Garman, C. Helms, *et al.*, “Rapid cloning of high-affinity human monoclonal antibodies against influenza virus,” *Nature*, vol. 453, no. 7195, pp. 667–671, 2008.

[4] A. C. Hurt, “Antiviral therapy for the next influenza pandemic,” *Tropical medicine and infectious disease*, vol. 4, no. 2, p. 67, 2019.

[5] R. Nachbagauer, A. Choi, A. Hirsh, I. Margine, S. Iida, A. Barrera, M. Ferres, R. A. Albrecht, A. García-Sastre, N. M. Bouvier, *et al.*, “Defining the antibody cross-reactome directed against the influenza virus surface glycoproteins,” *Nature immunology*, vol. 18, no. 4, p. 464, 2017.

[6] D. J. Smith, S. Forrest, D. H. Ackley, and A. S. Perelson, “Variable efficacy of repeated annual influenza vaccination,” *Proceedings of the National Academy of Sciences*, vol. 96, no. 24, pp. 14001–14006, 1999.

[7] S. Luo and A. S. Perelson, “Competitive exclusion by autologous antibodies can prevent broad HIV-1 antibodies from arising,” *Proceedings of the National Academy of Sciences*, vol. 112, no. 37, pp. 11654–11659, 2015.

[8] S. Wang, J. Mata-Fink, B. Kriegsman, M. Hanson, D. J. Irvine, H. N. Eisen, D. R. Burton, K. D. Wittrup, M. Kardar, and A. K. Chakraborty, “Manipulating the selection forces during affinity maturation to generate cross-reactive HIV antibodies,” *Cell*, vol. 160, no. 4, pp. 785–797, 2015.

[9] Y. Yu, D. Rüppel, W. Weber, and H. Derendorf, “PK/PD approaches,” *Drug Discovery and Evaluation: Methods in Clinical Pharmacology*, pp. 1–23, 2019.

[10] P. Baccam, C. Beauchemin, C. A. Macken, F. G. Hayden, and A. S. Perelson, "Kinetics of influenza A virus infection in humans," *Journal of virology*, vol. 80, no. 15, pp. 7590–7599, 2006.

[11] E. N. Sanchez and F. Ornelas-Tellez, *Discrete-time inverse optimal control for nonlinear systems.* CRC Press, 2017.

[12] T. Yang, *Impulsive control theory*, vol. 272. Springer Science & Business Media, 2001.

[13] W. M. Haddad, V. Chellaboina, and S. G. Nersesov, *Impulsive and Hybrid Dynamical Systems: Stability, Dissipativity, and Control.* Princeton University Press, 2006.

[14] A. Y. Alanis, E. N. Sanchez, A. G. Loukianov, and E. A. Hernandez, "Discrete-time recurrent high order neural networks for nonlinear identification," *Journal of the Franklin Institute, Elsevier,*, vol. 347, no. 7, pp. 1253–1265, 2010.

[15] H. N. Eisen, "Affinity enhancement of antibodies: how low-affinity antibodies produced early in immune responses are followed by high-affinity antibodies later and in memory B-cell responses," *Cancer immunology research*, vol. 2, no. 5, pp. 381–392, 2014.

[16] G. D. Victora and P. C. Wilson, "Germinal center selection and the antibody response to influenza," *Cell*, vol. 163, no. 3, pp. 545–548, 2015.

[17] G. D. Victora and M. C. Nussenzweig, "Germinal centers," *Annual review of immunology*, vol. 30, pp. 429–457, 2012.

[18] N. S. De Silva and U. Klein, "Dynamics of B cells in germinal centres," *Nature reviews immunology*, vol. 15, no. 3, p. 137, 2015.

[19] T. W. LeBien and T. F. Tedder, "B lymphocytes: how they develop and function," *Blood*, vol. 112, no. 5, pp. 1570–1580, 2008.

[20] A. S. Perelson and G. F. Oster, "Theoretical studies of clonal selection: minimal antibody repertoire size and reliability of self-non-self discrimination," *Journal of theoretical biology*, vol. 81, no. 4, pp. 645–670, 1979.

[21] A. Lapedes, R. Farber, *et al.*, "The geometry of shape space: application to influenza," *Journal of theoretical biology*, vol. 212, no. 1, pp. 57–70, 2001.

[22] D. J. Smith, A. S. Lapedes, J. C. de Jong, T. M. Bestebroer, G. F. Rimmelzwaan, A. D. Osterhaus, and R. A. Fouchier, "Mapping the antigenic and genetic evolution of influenza virus," *Science*, vol. 305, no. 5682, pp. 371–376, 2004.

[23] J. Sheng and S. Wang, "Coevolutionary transitions emerging from flexible molecular recognition and eco-evolutionary feedback," *Iscience*, vol. 24, no. 8, p. 102861, 2021.

[24] F. Klein, R. Diskin, J. F. Scheid, C. Gaebler, H. Mouquet, I. S. Georgiev, M. Pancera, T. Zhou, R.-B. Incesu, B. Z. Fu, *et al.*, "Somatic mutations of the immunoglobulin framework are generally required for broad and potent HIV-1 neutralization," *Cell*, vol. 153, no. 1, pp. 126–138, 2013.

[25] S. Lucia, M. Schliemann-Bullinger, R. Findeisen, and E. Bullinger, “A set-based optimal control approach for pharmacokinetic/pharmacodynamic drug dosage design,” *IFAC-PapersOnLine*, vol. 49, no. 7, pp. 797–802, 2016.

[26] E. W. Larson, J. W. Dominik, A. H. Rowberg, and G. A. Higbee, “Influenza virus population dynamics in the respiratory tract of experimentally infected mice.,” *Infection and immunity*, vol. 13, no. 2, pp. 438–447, 1976.

[27] S. Lukens, G. Clermont, and D. Swigon, “Sensitivity of human immune response to influenza a virus infection and its dependence on virus and host phenotypes,” *Journal of Critical Care*, vol. 1, no. 28, pp. e7–e8, 2013.

[28] I. Price, E. D. Mochan-Keef, D. Swigon, G. B. Ermentrout, S. Lukens, F. R. Toapanta, T. M. Ross, and G. Clermont, “The inflammatory response to influenza a virus (h1n1): An experimental and mathematical study,” *Journal of theoretical biology*, vol. 374, pp. 83–93, 2015.

[29] V. I. Zarnitsyna, A. Handel, S. R. McMaster, S. L. Hayward, J. E. Kohlmeier, and R. Antia, “Mathematical model reveals the role of memory cd8 t cell populations in recall responses to influenza,” *Frontiers in immunology*, vol. 7, p. 165, 2016.

[30] A. W. Yan, P. Cao, J. M. Heffernan, J. McVernon, K. M. Quinn, N. L. La Gruta, K. L. Laurie, and J. M. McCaw, “Modelling cross-reactivity and memory in the cellular adaptive immune response to influenza infection in the host,” *Journal of Theoretical Biology*, vol. 413, pp. 34–49, 2017.

[31] A. M. Smith, “Host-pathogen kinetics during influenza infection and coinfection: insights from predictive modeling,” *Immunological reviews*, vol. 285, no. 1, pp. 97–112, 2018.

[32] E. Lafont, S. Urien, J.-E. Salem, N. Heming, and C. Faisy, “Modeling for critically ill patients: an introduction for beginners,” *Journal of critical care*, vol. 30, no. 6, pp. 1287–1294, 2015.

[33] T. Tängdén, V. R. Martín, T. Felton, E. I. Nielsen, S. Marchand, R. J. Brüggemann, J. Bulitta, M. Bassetti, U. Theuretzbacher, B. Tsuji, *et al.*, “The role of infection models and pk/pd modelling for optimising care of critically ill patients with severe infections,” *Intensive care medicine*, vol. 43, no. 7, pp. 1021–1032, 2017.

[34] P. H. Van der Graaf and N. Benson, “Systems pharmacology: bridging systems biology and pharmacokinetics-pharmacodynamics (PK-PD) in drug discovery and development,” *Pharmaceutical research*, vol. 28, no. 7, pp. 1460–1464, 2011.

[35] P. S. Rivadeneira, M. Caicedo, A. Ferramosca, and A. H. González, “Impulsive zone model predictive control (iZMPC) for therapeutic treatments: application to HIV dynamics,” in *2017 IEEE 56th Annual Conference on Decision and Control (CDC)*, pp. 4094–4099, IEEE, 2017.

[36] J. Hollỳ, M. Fogelová, L. Jakubcová, K. Tomčíková, M. Vozárová, E. Varečková, and F. Kostolanskỳ, "Comparison of infectious influenza A virus quantification methods employing immuno-staining," *Journal of virological methods*, vol. 247, pp. 107–113, 2017.

[37] G. Hernandez-Mejia, A. Y. Alanis, and E. A. Hernandez-Vargas, "Neural inverse optimal control for discrete-time impulsive systems," *Neurocomputing*, vol. 314, pp. 101–108, 2018.

[38] E. N. Sanchez, A. Y. Alanís, and A. G. Loukianov, *Discrete-time high order neural control: trained with Kalman filtering*, vol. 112. Springer Science & Business Media, 2008.

[39] M. A. Nielsen, *Neural networks and deep learning*, vol. 25.

[40] S. S. Haykin, *Neural networks and learning machines*, vol. 3. Pearson Upper Saddle River,, 2009.

[41] A. S. Poznyak, E. N. Sanchez, and W. Yu, *Differential neural networks for robust nonlinear control: identification, state estimation and trajectory tracking*. World Scientific, 2001.

[42] A. M. Schaefer and H.-G. Zimmermann, "Recurrent neural networks are universal approximators," *International journal of neural systems, World Scientific.*, vol. 17, no. 01, pp. 253–263, 2007.

[43] G. A. Rovithakis and M. A. Christodoulou, *Adaptive control with recurrent high-order neural networks: theory and industrial applications*. Springer Science & Business Media, 2012.

[44] S. S. Haykin *et al.*, *Kalman filtering and neural networks*. Wiley Online Library, 2001.

[45] A. Y. Alanis and E. N. Sanchez, *Discrete-Time Neural Observers: Analysis and Applications*. Academic Press, 2017.

[46] R. E. Kalman, "A New Approach to Linear Filtering and Prediction Problems," *Journal of Basic Engineering*, vol. 82, pp. 35–45, 03 1960.

[47] A. Handel, I. M. Longini Jr, and R. Antia, "Neuraminidase inhibitor resistance in influenza: assessing the danger of its generation and spread," *PLoS Computational Biology*, vol. 3, no. 12, p. e240, 2007.

[48] S. M. Petrie, T. Guarnaccia, K. L. Laurie, A. C. Hurt, J. McVernon, and J. M. McCaw, "Reducing uncertainty in within-host parameter estimates of influenza infection by measuring both infectious and total viral load," *PLoS One*, vol. 8, no. 5, p. e64098, 2013.

[49] A. Boianelli, V. K. Nguyen, T. Ebensen, K. Schulze, E. Wilk, N. Sharma, S. Stegemann-Koniszewski, D. Bruder, F. R. Toapanta, C. A. Guzmán, *et al.*, "Modeling influenza virus infection: A roadmap for influenza research," *Viruses*, vol. 7, no. 10, pp. 5274–5304, 2015.

[50] S. S. Jhutty, J. D. Boehme, A. Jeron, J. Volckmar, K. Schultz, J. Schreiber, K. Schughart, K. Zhou, J. Steinheimer, H. Stöcker, S. Stegemann-Koniszewski, D. Bruder, and E. A. Hernandez-Vargas, "Predicting influenza a virus infection in the lung from hematological data with machine learning," *mSystems*, vol. 0, no. 0, pp. e00459–22.

[51] Y. Guan, D. Vijaykrishna, J. Bahl, H. Zhu, J. Wang, and G. J. Smith, "The emergence of pandemic influenza viruses," *Protein & cell*, vol. 1, no. 1, pp. 9–13, 2010.

[52] P. Palese, "Influenza: old and new threats," *Nature medicine*, vol. 10, no. 12, pp. S82–S87, 2004.

[53] G. J. Smith, D. Vijaykrishna, J. Bahl, S. J. Lycett, M. Worobey, O. G. Pybus, S. K. Ma, C. L. Cheung, J. Raghwani, S. Bhatt, *et al.*, "Origins and evolutionary genomics of the 2009 swine-origin H1N1 influenza A epidemic," *Nature*, vol. 459, no. 7250, pp. 1122–1125, 2009.

[54] W. Smith, C. H. Andrewes, P. P. Laidlaw, *et al.*, "A virus obtained from influenza patients.," *Lancet*, pp. 66–8, 1933.

[55] D. Hobson, R. Curry, A. Beare, and A. Ward-Gardner, "The role of serum haemagglutination-inhibiting antibody in protection against challenge infection with influenza A2 and B viruses," *Epidemiology & Infection*, vol. 70, no. 4, pp. 767–777, 1972.

[56] J. Sui, W. C. Hwang, S. Perez, G. Wei, D. Aird, L.-m. Chen, E. Santelli, B. Stec, G. Cadwell, M. Ali, *et al.*, "Structural and functional bases for broad-spectrum neutralization of avian and human influenza A viruses," *Nature structural & molecular biology*, vol. 16, no. 3, p. 265, 2009.

[57] F. Krammer, "The human antibody response to influenza A virus infection and vaccination," *Nature Reviews Immunology*, p. 1, 2019.

[58] S. G. Muthuri, S. Venkatesan, P. R. Myles, J. Leonardi-Bee, T. S. Al Khuwaitir, A. Al Mamun, A. P. Anovadiya, E. Azziz-Baumgartner, C. Báez, M. Bassetti, *et al.*, "Effectiveness of neuraminidase inhibitors in reducing mortality in patients admitted to hospital with influenza A H1N1pdm09 virus infection: a meta-analysis of individual participant data," *The lancet Respiratory medicine*, vol. 2, no. 5, pp. 395–404, 2014.

[59] J. Dobson, R. J. Whitley, S. Pocock, and A. S. Monto, "Oseltamivir treatment for influenza in adults: a meta-analysis of randomised controlled trials," *The Lancet*, vol. 385, no. 9979, pp. 1729–1737, 2015.

[60] C. Parra-Rojas, V. K. Nguyen, G. Hernandez-Mejia, E. A. Hernandez-Vargas, *et al.*, "Neuraminidase inhibitors in influenza treatment and prevention–is it time to call it a day?," *Viruses*, vol. 10, no. 9, p. 454, 2018.

[61] B. La Roche Ltd, Switzerland, "Tamiflu (oseltamivir phosphate) capsules and oral suspension," *https://www.accessdata.fda.gov/drugsatfda-docs/nda/2000/21-246-Tamiflu-Prntlbl.pdf.*, 2019-Online.

[62] A. H. González, P. S. Rivadeneira, A. Ferramosca, N. Magdelaine, and C. H. Moog, "Impulsive zone MPC for type I diabetic patients based on a long-term model," *IFAC-PapersOnLine*, vol. 50, no. 1, pp. 14729–14734, 2017.

[63] E. A. Hernandez-Vargas, "Modeling kick-kill strategies toward HIV cure," *Frontiers in immunology*, vol. 8, p. 995, 2017.

[64] G. Hernandez-Mejia, A. Y. Alanis, and E. A. Hernandez-Vargas, "Inverse optimal impulsive control based treatment of influenza infection," *IFAC-PapersOnLine*, vol. 50, no. 1, pp. 12185–12190, 2017.

[65] G. Hernandez-Mejia, A. Y. Alanis, M. Hernandez-Gonzalez, R. Findeisen, and E. A. Hernandez-Vargas, "Passivity-based inverse optimal impulsive control for influenza treatment in the host," *IEEE Transactions on Control Systems Technology*, 2019.

[66] G. Hernandez-Mejia, "Control-based drug tailoring schemes towards personalized influenza treatment," in *Feedback Control for Personalized Medicine*, pp. 109–128, Elsevier, 2022.

[67] R. Pfeiffer, "Vorläufige mittheilungen über die erreger der influenza," *DMW-Deutsche Medizinische Wochenschrift*, vol. 18, no. 02, pp. 28–28, 1892.

[68] H. L. Van Epps, "Influenza: exposing the true killer," *The Journal of experimental medicine*, vol. 203, no. 4, p. 803, 2006.

[69] R. E. Shope, "Swine influenza: I. Experimental transmission and pathology," *The Journal of experimental medicine*, vol. 54, no. 3, pp. 349–359, 1931.

[70] P. A. Lewis and R. E. Shope, "Swine influenza: II. A hemophilic bacillus from the respiratory tract of infected swine," *The Journal of experimental medicine*, vol. 54, no. 3, pp. 361–371, 1931.

[71] R. E. Shope, "Swine influenza: III. Filtration experiments and etiology," *The Journal of experimental medicine*, vol. 54, no. 3, pp. 373–385, 1931.

[72] D. Molineux, "Dr. Molineux's Historical account of the late general coughs and colds; with some observations on other Epidemick Distempers," *Philosophical Transactions (1683-1775)*, pp. 105–111, 1694.

[73] C. W. Potter, "A history of influenza," *Journal of applied microbiology*, vol. 91, no. 4, pp. 572–579, 2001.

[74] R. C. Dicker, F. Coronado, D. Koo, and R. G. Parrish, "Principles of epidemiology in public health practice; an introduction to applied epidemiology and biostatistics," 2006.

[75] D. Vijaykrishna, R. Mukerji, and G. J. Smith, "Rna virus reassortment: an evolutionary mechanism for host jumps and immune evasion," *PLoS Pathog*, vol. 11, no. 7, p. e1004902, 2015.

[76] J. K. Taubenberger, J. C. Kash, and D. M. Morens, "The 1918 influenza pandemic: 100 years of questions answered and unanswered," *Science translational medicine*, vol. 11, no. 502, 2019.

[77] P. Palese, T. M. Tumpey, and A. Garcia-Sastre, "What can we learn from reconstructing the extinct 1918 pandemic influenza virus?," *Immunity*, vol. 24, no. 2, pp. 121–124, 2006.

[78] M. C. White and A. C. Lowen, "Implications of segment mismatch for influenza a virus evolution," *The Journal of general virology*, vol. 99, no. 1, p. 3, 2018.

[79] I. Kosik and J. W. Yewdell, "Influenza hemagglutinin and neuraminidase: Yin–yang proteins coevolving to thwart immunity," *Viruses*, vol. 11, no. 4, p. 346, 2019.

[80] C. Ke, C. K. P. Mok, W. Zhu, H. Zhou, J. He, W. Guan, J. Wu, W. Song, D. Wang, J. Liu, *et al.*, "Human infection with highly pathogenic avian influenza A (H7N9) virus, china," *Emerging infectious diseases*, vol. 23, no. 8, p. 1332, 2017.

[81] L. E. Leigh Perkins and D. E. Swayne, "Pathogenicity of a Hong Kong–origin H5N1 highly pathogenic avian influenza virus for emus, geese, ducks, and pigeons," *Avian diseases*, vol. 46, no. 1, pp. 53–63, 2002.

[82] R. W. Compans and M. B. Oldstone, *Influenza Pathogenesis and Control-Volume I*. Springer, 2014.

[83] T. H. Oguin, S. Sharma, A. D. Stuart, S. Duan, S. A. Scott, C. K. Jones, J. S. Daniels, C. W. Lindsley, P. G. Thomas, and H. A. Brown, "Phospholipase d facilitates efficient entry of influenza virus, allowing escape from innate immune inhibition," *Journal of Biological Chemistry*, vol. 289, no. 37, pp. 25405–25417, 2014.

[84] D. O. White and I. M. Cheyne, "Early events in the eclipse phase of influenza and parainfluenza virus infection," *Virology*, vol. 29, no. 1, pp. 49–59, 1966.

[85] J. Kreijtz, R. Fouchier, and G. Rimmelzwaan, "Immune responses to influenza virus infection," *Virus research*, vol. 162, no. 1-2, pp. 19–30, 2011.

[86] S.-i. Tamura and T. Kurata, "Defense mechanisms against influenza virus infection in the respiratory tract mucosa," *Jpn J Infect Dis*, vol. 57, no. 6, pp. 236–47, 2004.

[87] I. K. Pang and A. Iwasaki, "Inflammasomes as mediators of immunity against influenza virus," *Trends in immunology*, vol. 32, no. 1, pp. 34–41, 2011.

[88] F. Heil, H. Hemmi, H. Hochrein, F. Ampenberger, C. Kirschning, S. Akira, G. Lipford, H. Wagner, and S. Bauer, “Species-specific recognition of single-stranded rna via toll-like receptor 7 and 8,” *Science*, vol. 303, no. 5663, pp. 1526–1529, 2004.

[89] H. M. Kim, Y.-W. Lee, K.-J. Lee, H. S. Kim, S. W. Cho, N. Van Rooijen, Y. Guan, and S. H. Seo, “Alveolar macrophages are indispensable for controlling influenza viruses in lungs of pigs,” *Journal of virology*, vol. 82, no. 9, pp. 4265–4274, 2008.

[90] C. H. GeurtsvanKessel, I. M. Bergen, F. Muskens, L. Boon, H. C. Hoogsteden, A. D. Osterhaus, G. F. Rimmelzwaan, and B. N. Lambrecht, “Both conventional and interferon killer dendritic cells have antigen-presenting capacity during influenza virus infection,” *PloS one*, vol. 4, no. 9, p. e7187, 2009.

[91] J. Surls, C. Nazarov-Stoica, M. Kehl, S. Casares, and T.-D. Brumeanu, “Differential effect of cd4+ foxp3+ t-regulatory cells on the b and t helper cell responses to influenza virus vaccination,” *Vaccine*, vol. 28, no. 45, pp. 7319–7330, 2010.

[92] R. Bodewes, M. M. Geelhoed-Mieras, J. Wrammert, R. Ahmed, P. C. Wilson, R. A. Fouchier, A. D. Osterhaus, and G. F. Rimmelzwaan, “In vitro assessment of the immunological significance of a human monoclonal antibody directed to the influenza a virus nucleoprotein,” *Clinical and Vaccine Immunology*, vol. 20, no. 8, pp. 1333–1337, 2013.

[93] A. G. Schmidt, M. D. Therkelsen, S. Stewart, T. B. Kepler, H.-X. Liao, M. A. Moody, B. F. Haynes, and S. C. Harrison, “Viral receptor-binding site antibodies with diverse germline origins,” *Cell*, vol. 161, no. 5, pp. 1026–1034, 2015.

[94] D. Angeletti, J. S. Gibbs, M. Angel, I. Kosik, H. D. Hickman, G. M. Frank, S. R. Das, A. K. Wheatley, M. Prabhakaran, D. J. Leggat, *et al.*, “Defining B cell immunodominance to viruses,” *Nature immunology*, vol. 18, no. 4, p. 456, 2017.

[95] S. F. Andrews, Y. Huang, K. Kaur, L. I. Popova, I. Y. Ho, N. T. Pauli, C. J. H. Dunand, W. M. Taylor, S. Lim, M. Huang, *et al.*, “Immune history profoundly affects broadly protective B cell responses to influenza,” *Science translational medicine*, vol. 7, no. 316, pp. 316ra192–316ra192, 2015.

[96] M. Kuraoka, A. G. Schmidt, T. Nojima, F. Feng, A. Watanabe, D. Kitamura, S. C. Harrison, T. B. Kepler, and G. Kelsoe, “Complex antigens drive permissive clonal selection in germinal centers,” *Immunity*, vol. 44, no. 3, pp. 542–552, 2016.

[97] L. Pappas, M. Foglierini, L. Piccoli, N. L. Kallewaard, F. Turrini, C. Silacci, B. Fernandez-Rodriguez, G. Agatic, I. Giacchetto-Sasselli, G. Pellicciotta, *et al.*, “Rapid development of broadly influenza neutralizing antibodies through redundant mutations,” *Nature*, vol. 516, no. 7531, pp. 418–422, 2014.

[98] H. O. Padilla-Quirarte, D. V. L. Guerrero, M. L. Gutierrez-Xicotencatl, and F. R. Esquivel-Guadarrama, “Protective antibodies against influenza proteins,” *Frontiers in immunology*, vol. 10, p. 1677, 2019.

[99] A. S. Monto, R. E. Malosh, J. G. Petrie, and E. T. Martin, "The doctrine of original antigenic sin: separating good from evil," *The Journal of infectious diseases*, vol. 215, no. 12, pp. 1782–1788, 2017.

[100] C. Henry, A.-K. E. Palm, F. Krammer, and P. C. Wilson, "From original antigenic sin to the universal influenza virus vaccine," *Trends in immunology*, vol. 39, no. 1, pp. 70–79, 2018.

[101] Y. Li, J. L. Myers, D. L. Bostick, C. B. Sullivan, J. Madara, S. L. Linderman, Q. Liu, D. M. Carter, J. Wrammert, S. Esposito, *et al.*, "Immune history shapes specificity of pandemic H1N1 influenza antibody responses," *Journal of Experimental Medicine*, vol. 210, no. 8, pp. 1493–1500, 2013.

[102] N. S. Heaton, D. Sachs, C.-J. Chen, R. Hai, and P. Palese, "Genome-wide mutagenesis of influenza virus reveals unique plasticity of the hemagglutinin and NS1 proteins," *Proceedings of the National Academy of Sciences*, vol. 110, no. 50, pp. 20248–20253, 2013.

[103] C. S. Anderson, S. Ortega, F. A. Chaves, A. M. Clark, H. Yang, D. J. Topham, and M. L. DeDiego, "Natural and directed antigenic drift of the H1 influenza virus hemagglutinin stalk domain," *Scientific reports*, vol. 7, no. 1, p. 14614, 2017.

[104] E. Kirkpatrick, X. Qiu, P. C. Wilson, J. Bahl, and F. Krammer, "The influenza virus hemagglutinin head evolves faster than the stalk domain," *Scientific reports*, vol. 8, no. 1, p. 10432, 2018.

[105] D. C. Ekiert, R. H. Friesen, G. Bhabha, T. Kwaks, M. Jongeneelen, W. Yu, C. Ophorst, F. Cox, H. J. Korse, B. Brandenburg, *et al.*, "A highly conserved neutralizing epitope on group 2 influenza A viruses," *Science*, vol. 333, no. 6044, pp. 843–850, 2011.

[106] M. Throsby, E. van den Brink, M. Jongeneelen, L. L. Poon, P. Alard, L. Cornelissen, A. Bakker, F. Cox, E. van Deventer, Y. Guan, *et al.*, "Heterosubtypic neutralizing monoclonal antibodies cross-protective against H5N1 and H1N1 recovered from human IgM+ memory B cells," *PloS one*, vol. 3, no. 12, 2008.

[107] K. R. McCarthy, A. Watanabe, M. Kuraoka, K. T. Do, C. E. McGee, G. D. Sempowski, T. B. Kepler, A. G. Schmidt, G. Kelsoe, and S. C. Harrison, "Memory B cells that cross-react with group 1 and group 2 influenza A viruses are abundant in adult human repertoires," *Immunity*, vol. 48, no. 1, pp. 174–184, 2018.

[108] P. A. Robert, A. L. Marschall, and M. Meyer-Hermann, "Induction of broadly neutralizing antibodies in germinal centre simulations," *Current opinion in biotechnology*, vol. 51, pp. 137–145, 2018.

[109] S. Chaudhury, J. Reifman, and A. Wallqvist, "Simulation of B cell affinity maturation explains enhanced antibody cross-reactivity induced by the polyvalent malaria vaccine AMA1," *The Journal of Immunology*, vol. 193, no. 5, pp. 2073–2086, 2014.

[110] S. Khailaie, P. A. Robert, A. Toker, J. Huehn, and M. Meyer-Hermann, “A signal integration model of thymic selection and natural regulatory T cell commitment,” *The Journal of Immunology*, p. 1400889, 2014.

[111] G. Hernandez-Mejia and E. A. Hernandez-Vargas, “Uncovering antibody cross-reaction dynamics in influenza A infections,” *Bioinformatics*, vol. btaa691, 2020.

[112] M. McCallum, A. De Marco, F. A. Lempp, M. A. Tortorici, D. Pinto, A. C. Walls, M. Beltramello, A. Chen, Z. Liu, F. Zatta, *et al.*, “N-terminal domain antigenic mapping reveals a site of vulnerability for SARS-CoV-2,” *Cell*, 2021.

[113] S. Duwe, “Influenza viruses–antiviral therapy and resistance,” *GMS infectious diseases*, vol. 5, 2017.

[114] J. L. McKimm-Breschkin, “Influenza neuraminidase inhibitors: antiviral action and mechanisms of resistance,” *Influenza and other respiratory viruses*, vol. 7, pp. 25–36, 2013.

[115] G. N. Okoli, H. E. Otete, C. R. Beck, and J. S. Nguyen-Van-Tam, “Use of neuraminidase inhibitors for rapid containment of influenza: a systematic review and meta-analysis of individual and household transmission studies,” *PloS one*, vol. 9, no. 12, 2014.

[116] K. McClellan and C. M. Perry, “Oseltamivir,” *Drugs*, vol. 61, no. 2, pp. 263–283, 2001.

[117] M. Okomo-Adhiambo, A. M. Fry, S. Su, H. T. Nguyen, A. A. Elal, E. Negron, J. Hand, R. J. Garten, J. Barnes, X. Xiyan, *et al.*, “Oseltamivir-resistant influenza A (H1N1) pdm09 viruses, United States, 2013–14,” *Emerging infectious diseases*, vol. 21, no. 1, p. 136, 2015.

[118] F. G. Hayden, N. Sugaya, N. Hirotsu, N. Lee, M. D. de Jong, A. C. Hurt, T. Ishida, H. Sekino, K. Yamada, S. Portsmouth, *et al.*, “Baloxavir marboxil for uncomplicated influenza in adults and adolescents,” *New England Journal of Medicine*, vol. 379, no. 10, pp. 913–923, 2018.

[119] Y. Furuta, T. Komeno, and T. Nakamura, “Favipiravir (t-705), a broad spectrum inhibitor of viral rna polymerase,” *Proceedings of the Japan Academy, Series B*, vol. 93, no. 7, pp. 449–463, 2017.

[120] F. G. Hayden and N. Shindo, “Influenza virus polymerase inhibitors in clinical development,” *Current opinion in infectious diseases*, vol. 32, no. 2, p. 176, 2019.

[121] E. Takashita, C. Kawakami, R. Ogawa, H. Morita, S. Fujisaki, M. Shirakura, H. Miura, K. Nakamura, N. Kishida, T. Kuwahara, *et al.*, “Influenza A (H3N2) virus exhibiting reduced susceptibility to baloxavir due to a polymerase acidic subunit I38T substitution detected from a hospitalised child without prior baloxavir treatment, Japan, January 2019,” *Eurosurveillance*, vol. 24, no. 12, 2019.

[122] P. Koszalka, D. Tilmanis, and A. C. Hurt, "Influenza antivirals currently in late-phase clinical trial," *Influenza and other respiratory viruses*, vol. 11, no. 3, pp. 240–246, 2017.

[123] J. H. Beigel, P. Tebas, M.-C. Elie-Turenne, E. Bajwa, T. E. Bell, C. B. Cairns, S. Shoham, J. G. Deville, E. Feucht, J. Feinberg, *et al.*, "Immune plasma for the treatment of severe influenza: an open-label, multicentre, phase 2 randomised study," *The Lancet Respiratory Medicine*, vol. 5, no. 6, pp. 500–511, 2017.

[124] N. Principi, B. Camilloni, A. Alunno, I. Polinori, A. Argentiero, and S. Esposito, "Drugs for influenza treatment: is there significant news?," *Frontiers in medicine*, vol. 6, p. 109, 2019.

[125] I. Tavassoly, J. Goldfarb, and R. Iyengar, "Systems biology primer: the basic methods and approaches," *Essays in biochemistry*, vol. 62, no. 4, pp. 487–500, 2018.

[126] E. A. Hernandez-Vargas, *Modeling and Control of Infectious Diseases in the Host: With MATLAB and R.* Academic Press, 2019.

[127] G. Hernandez-Mejia and E. A. Hernandez-Vargas, "PK/PD-based impulsive control to tailor therapies in infectious diseases," *IFAC-PapersOnLine*, vol. 53, no. 2, pp. 16055–16060, 2020.

[128] N. Giordano, F. Mairet, J.-L. Gouzé, J. Geiselmann, and H. de Jong, "Dynamical allocation of cellular resources as an optimal control problem: novel insights into microbial growth strategies," *PLoS computational biology*, vol. 12, no. 3, p. e1004802, 2016.

[129] X. Jin, C.-S. Kim, G. A. Dumont, J. M. Ansermino, and J.-O. Hahn, "A semi-adaptive control approach to closed-loop medication infusion," *International Journal of Adaptive Control and Signal Processing*, vol. 31, no. 2, pp. 240–254, 2017.

[130] J. H. Abel, A. Chakrabarty, E. B. Klerman, and F. J. Doyle III, "Pharmaceutical-based entrainment of circadian phase via nonlinear model predictive control," *Automatica*, vol. 100, pp. 336–348, 2019.

[131] A. Y. Alanis, Y. Y. Rios, J. García-Rodríguez, E. N. Sanchez, E. Ruiz-Velázquez, and A. P. Garcia, "Neuro-fuzzy inverse optimal control incorporating a multistep predictor as applied to t1dm patients," in *Control Applications for Biomedical Engineering Systems*, pp. 1–24, Elsevier, 2020.

[132] P. S. Rivadeneira, C. H. Moog, G.-B. Stan, C. Brunet, F. Raffi, V. Ferré, V. Costanza, M. J. Mhawej, F. Biafore, D. A. Ouattara, *et al.*, "Mathematical modeling of HIV dynamics after antiretroviral therapy initiation: A review," *BioResearch open access*, vol. 3, no. 5, pp. 233–241, 2014.

[133] E. A. Hernandez-Vargas, P. Colaneri, and R. H. Middleton, "Switching strategies to mitigate HIV mutation," *IEEE Transactions on Control Systems Technology*, vol. 22, no. 4, pp. 1623–1628, 2014.

[134] A. M. Schäfer and H.-G. Zimmermann, “Recurrent neural networks are universal approximators,” *International journal of neural systems*, vol. 17, no. 04, pp. 253–263, 2007.

[135] G. Puscasu, B. Codres, A. Stancu, and G. Murariu, “Nonlinear system identification based on internal recurrent neural networks,” *International Journal of Neural Systems, World Scientific.*, vol. 19, no. 02, pp. 115–125, 2009.

[136] G. Hernandez-Mejia, X. Du, A. Y. Alanis, and E. A. Hernandez-Vargas, “Bounded input impulsive control for scheduling therapies,” *Journal of Process Control*, vol. 102, pp. 34–43, 2021.

[137] D. M. Carter, C. E. Bloom, E. J. Nascimento, E. T. Marques, J. K. Craigo, J. L. Cherry, D. J. Lipman, and T. M. Ross, “Sequential seasonal h1n1 influenza virus infections protect ferrets against novel 2009 h1n1 influenza virus,” *Journal of virology*, vol. 87, no. 3, pp. 1400–1410, 2013.

[138] I. Margine, R. Hai, R. A. Albrecht, G. Obermoser, A. C. Harrod, J. Banchereau, K. Palucka, A. García-Sastre, P. Palese, J. J. Treanor, *et al.*, “H3N2 influenza virus infection induces broadly reactive hemagglutinin stalk antibodies in humans and mice,” *Journal of virology*, pp. JVI–03509, 2013.

[139] S. F. Andrews, M. G. Joyce, M. J. Chambers, R. A. Gillespie, M. Kanekiyo, K. Leung, E. S. Yang, Y. Tsybovsky, A. K. Wheatley, M. C. Crank, *et al.*, “Preferential induction of cross-group influenza a hemagglutinin stem–specific memory b cells after h7n9 immunization in humans,” *Science immunology*, vol. 2, no. 13, p. eaan2676, 2017.

[140] W. Dong, Y. Bhide, F. Sicca, T. Meijerhof, K. Guilfoyle, O. G. Engelhardt, L. Boon, C. A. De Haan, G. Carnell, N. Temperton, *et al.*, “Cross-protective immune responses induced by sequential influenza virus infection and by sequential vaccination with inactivated influenza vaccines,” *Frontiers in immunology*, p. 2312, 2018.

[141] G. S. Tan, P. S. Lee, R. M. Hoffman, B. Mazel-Sanchez, F. Krammer, P. E. Leon, A. B. Ward, I. A. Wilson, and P. Palese, “Characterization of a broadly neutralizing monoclonal antibody that targets the fusion domain of group 2 influenza A virus hemagglutinin,” *Journal of virology*, vol. 88, no. 23, pp. 13580–13592, 2014.

[142] C. Chiu, A. H. Ellebedy, J. Wrammert, and R. Ahmed, “B-cell responses to influenza infection and vaccination,” in *Influenza Pathogenesis and Control-Volume II*, pp. 381–398, Springer, 2014.

[143] G. A. Kirchenbaum, D. M. Carter, and T. M. Ross, “Sequential infection in ferrets with antigenically distinct seasonal H1N1 influenza viruses boosts hemagglutinin stalk-specific antibodies,” *Journal of virology*, vol. 90, no. 2, pp. 1116–1128, 2016.

[144] L. Buchauer and H. Wardemann, “Calculating germinal centre reactions,” *Current Opinion in Systems Biology*, vol. 18, pp. 1–8, 2019.

[145] D. J. Smith, S. Forrest, R. R. Hightower, and A. S. Perelson, "Deriving shape space parameters from immunological data," *Journal of theoretical biology*, vol. 189, no. 2, pp. 141–150, 1997.

[146] W. Dubitzky, O. Wolkenhauer, H. Yokota, and K.-H. Cho, *Encyclopedia of systems biology.* Springer Publishing Company, Incorporated, 2013.

[147] S. Wang, "Optimal sequential immunization can focus antibody responses against diversity loss and distraction," *PLoS computational biology*, vol. 13, no. 1, p. e1005336, 2017.

[148] J. M. Fonville, S. Wilks, S. L. James, A. Fox, M. Ventresca, M. Aban, L. Xue, T. Jones, N. Le, Q. Pham, *et al.*, "Antibody landscapes after influenza virus infection or vaccination," *Science*, vol. 346, no. 6212, pp. 996–1000, 2014.

[149] J. B. Kruskal, "Multidimensional scaling by optimizing goodness of fit to a nonmetric hypothesis," *Psychometrika*, vol. 29, no. 1, pp. 1–27, 1964.

[150] J. B. Kruskal, "Nonmetric multidimensional scaling: a numerical method," *Psychometrika*, vol. 29, no. 2, pp. 115–129, 1964.

[151] B. T. Grenfell, O. G. Pybus, J. R. Gog, J. L. Wood, J. M. Daly, J. A. Mumford, and E. C. Holmes, "Unifying the epidemiological and evolutionary dynamics of pathogens," *science*, vol. 303, no. 5656, pp. 327–332, 2004.

[152] C. S. Anderson, P. R. McCall, H. A. Stern, H. Yang, and D. J. Topham, "Antigenic cartography of H1N1 influenza viruses using sequence-based antigenic distance calculation," *BMC bioinformatics*, vol. 19, no. 1, p. 51, 2018.

[153] J. D. Farmer, N. H. Packard, and A. S. Perelson, "The immune system, adaptation, and machine learning," *Physica D: Nonlinear Phenomena*, vol. 22, no. 1-3, pp. 187–204, 1986.

[154] A. S. Perelson, R. Hightower, and S. Forrest, "Evolution and somatic learning in V-region genes," *Research in Immunology*, vol. 147, no. 4, pp. 202–207, 1996.

[155] P. E. Seiden and F. Celada, "A model for simulating cognate recognition and response in the immune system," *Journal of theoretical biology*, vol. 158, no. 3, pp. 329–357, 1992.

[156] A. Bookstein, V. A. Kulyukin, and T. Raita, "Generalized hamming distance," *Information Retrieval*, vol. 5, no. 4, pp. 353–375, 2002.

[157] C. S. Anderson, M. Y. Sangster, H. Yang, T. J. Mariani, S. Chaudhury, and D. J. Topham, "Implementing sequence-based antigenic distance calculation into immunological shape space model," *BMC bioinformatics*, vol. 21, no. 1, pp. 1–13, 2020.

[158] P. L. Moore, N. Ranchobe, B. E. Lambson, E. S. Gray, E. Cave, M.-R. Abrahams, G. Bandawe, K. Mlisana, S. S. Abdool Karim, C. Williamson, *et al.*, "Limited neutralizing antibody specificities drive neutralization escape in early HIV-1 subtype c infection," *PLoS pathogens*, vol. 5, no. 9, p. e1000598, 2009.

[159] Y.-H. Ding, B. M. Baker, D. N. Garboczi, W. E. Biddison, and D. C. Wiley, "Four a6-tcr/peptide/hla-a2 structures that generate very different t cell signals are nearly identical," *Immunity*, vol. 11, no. 1, pp. 45–56, 1999.

[160] O. Bannard and J. G. Cyster, "Germinal centers: programmed for affinity maturation and antibody diversification," *Current opinion in immunology*, vol. 45, pp. 21–30, 2017.

[161] K. Murphy and C. Weaver, *Janeway's immunobiology.* Garland Science, 2016.

[162] A. K. Mishra and R. A. Mariuzza, "Insights into the structural basis of antibody affinity maturation from next-generation sequencing," *Frontiers in immunology*, vol. 9, p. 117, 2018.

[163] L. Mesin, J. Ersching, and G. D. Victora, "Germinal center b cell dynamics," *Immunity*, vol. 45, no. 3, pp. 471–482, 2016.

[164] Y. Cao, D. T. Gillespie, and L. R. Petzold, "Efficient step size selection for the tau-leaping simulation method," *The Journal of chemical physics*, vol. 124, no. 4, p. 044109, 2006.

[165] G. Hernandez-Mejia, "Discrete decay and half-life - a computational tool.," *Online: https://github.com/GustavoHdezM/Discrete-decay-and-Half-life.*, 2019.

[166] M. Meyer-Hermann, E. Mohr, N. Pelletier, Y. Zhang, G. D. Victora, and K.-M. Toellner, "A theory of germinal center B cell selection, division, and exit," *Cell reports*, vol. 2, no. 1, pp. 162–174, 2012.

[167] D. T. Gillespie, "Approximate accelerated stochastic simulation of chemically reacting systems," *The Journal of chemical physics*, vol. 115, no. 4, pp. 1716–1733, 2001.

[168] P. Vieira and K. Rajewsky, "The half-lives of serum immunoglobulins in adult mice," *European journal of immunology*, vol. 18, no. 2, pp. 313–316, 1988.

[169] D. Lingwood, P. M. McTamney, H. M. Yassine, J. R. Whittle, X. Guo, J. C. Boyington, C.-J. Wei, and G. J. Nabel, "Structural and genetic basis for development of broadly neutralizing influenza antibodies," *Nature*, vol. 489, no. 7417, pp. 566–570, 2012.

[170] M. D. Pauly, M. C. Procario, and A. S. Lauring, "A novel twelve class fluctuation test reveals higher than expected mutation rates for influenza A viruses," *Elife*, vol. 6, p. e26437, 2017.

[171] M. Bonsignori, T. Zhou, Z. Sheng, L. Chen, F. Gao, M. áGordon Joyce, G. Ozorowski, G.-Y. Chuang, C. Schramm, K. Wiehe, *et al.*, "Maturation pathway from germline to broad hiv-1 neutralizer of a CD4-mimic antibody," *Cell*, vol. 165, no. 2, pp. 449–463, 2016.

[172] T. Zhou, R. Lynch, L. Chen, P. Acharya, X. Wu, N. Doria-Rose, M. áGordon Joyce, D. Lingwood, C. Soto, R. Bailer, *et al.*, "Structural repertoire of HIV-1-neutralizing antibodies targeting the CD4 supersite in 14 donors," *Cell*, vol. 161, no. 6, pp. 1280–1292, 2015.

[173] M. Tikhonov, S. Kachru, and D. S. Fisher, "A model for the interplay between plastic tradeoffs and evolution in changing environments," *Proceedings of the National Academy of Sciences*, vol. 117, no. 16, pp. 8934–8940, 2020.

[174] K. G. Sprenger, J. E. Louveau, P. M. Murugan, and A. K. Chakraborty, "Optimizing immunization protocols to elicit broadly neutralizing antibodies," *Proceedings of the National Academy of Sciences*, vol. 117, no. 33, pp. 20077–20087, 2020.

[175] B. P. Holder and C. A. Beauchemin, "Exploring the effect of biological delays in kinetic models of influenza within a host or cell culture," *BMC Public Health*, vol. 11, no. 1, pp. 1–15, 2011.

[176] S. J. Smither, C. Lear-Rooney, J. Biggins, J. Pettitt, M. S. Lever, and G. G. Olinger Jr, "Comparison of the plaque assay and 50% tissue culture infectious dose assay as methods for measuring filovirus infectivity," *Journal of virological methods*, vol. 193, no. 2, pp. 565–571, 2013.

[177] C. Lei, J. Yang, J. Hu, and X. Sun, "On the calculation of TCID50 for quantitation of virus infectivity," *Virologica Sinica*, vol. 36, no. 1, pp. 141–144, 2021.

[178] S. H. Doak and Z. M. Zaïr, "Real-time reverse-transcription polymerase chain reaction: technical considerations for gene expression analysis," in *Genetic Toxicology*, pp. 251–270, Springer, 2012.

[179] P. Cao, A. W. Yan, J. M. Heffernan, S. Petrie, R. G. Moss, L. A. Carolan, T. A. Guarnaccia, A. Kelso, I. G. Barr, J. McVernon, *et al.*, "Innate immunity and the inter-exposure interval determine the dynamics of secondary influenza virus infection and explain observed viral hierarchies," *PLoS Comput Biol*, vol. 11, no. 8, p. e1004334, 2015.

[180] L. Canini and F. Carrat, "Population modeling of influenza a/h1n1 virus kinetics and symptom dynamics," *Journal of virology*, vol. 85, no. 6, pp. 2764–2770, 2011.

[181] H. Y. Lee, D. J. Topham, S. Y. Park, J. Hollenbaugh, J. Treanor, T. R. Mosmann, X. Jin, B. M. Ward, H. Miao, J. Holden-Wiltse, *et al.*, "Simulation and prediction of the adaptive immune response to influenza a virus infection," *Journal of virology*, vol. 83, no. 14, pp. 7151–7165, 2009.

[182] A. Tridane and Y. Kuang, "Modeling the interaction of cytotoxic t lymphocytes and influenza virus infected epithelial cells," *Mathematical Biosciences & Engineering*, vol. 7, no. 1, p. 171, 2010.

[183] C. Pommerenke, E. Wilk, B. Srivastava, A. Schulze, N. Novoselova, R. Geffers, and K. Schughart, "Global transcriptome analysis in influenza-infected mouse lungs reveals the kinetics of innate and adaptive host immune responses," *PloS one*, vol. 7, no. 7, p. e41169, 2012.

[184] E. J. Grant, S. M. Quiñones-Parra, E. B. Clemens, and K. Kedzierska, "Human influenza viruses and cd8+ t cell responses," *Current opinion in virology*, vol. 16, pp. 132–142, 2016.

[185] A. Handel, N. L. La Gruta, and P. G. Thomas, "Simulation modelling for immunologists," *Nature Reviews Immunology*, vol. 20, no. 3, pp. 186–195, 2020.

[186] J. Gabrielsson and D. Weiner, *Pharmacokinetic and pharmacodynamic data analysis: concepts and applications.* CRC Press, 2017.

[187] E. National Academies of Sciences, Medicine, *et al.*, "Virtual clinical trials: challenges and opportunities: proceedings of a workshop," 2019.

[188] H. Lehrach, "Virtual clinical trials, an essential step in increasing the effectiveness of the drug development process," *Public Health Genomics*, vol. 18, no. 6, pp. 366–371, 2015.

[189] C. K. Boughton and R. Hovorka, "New closed-loop insulin systems," *Diabetologia*, vol. 64, pp. 1007–1015, 2021.

[190] M. Metwally, T. O. Cheung, R. Smith, and K. J. Bell, "Insulin pump dosing strategies for meals varying in fat, protein or glycaemic index or grazing-style meals in type 1 diabetes: A systematic review," *Diabetes Research and Clinical Practice*, vol. 172, p. 108516, 2021.

[191] A. B. Daly, C. K. Boughton, M. Nwokolo, S. Hartnell, M. E. Wilinska, A. Cezar, M. L. Evans, and R. Hovorka, "Fully automated closed-loop insulin delivery in adults with type 2 diabetes: an open-label, single-center, randomized crossover trial," *Nature Medicine*, pp. 1–6, 2023.

[192] J. R. Martins and A. Ning, *Engineering design optimization.* Cambridge University Press, 2021.

[193] D. P. De Farias and B. Van Roy, "The linear programming approach to approximate dynamic programming," *Operations research*, vol. 51, no. 6, pp. 850–865, 2003.

[194] D. E. Kirk, *Optimal control theory: an introduction.* Courier Corporation, 2004.

[195] R. Sepulchre, M. Jankovic, and P. V. Kokotovic, *Constructive nonlinear control.* Springer Science & Business Media, 2012.

[196] P. Werbos, "Approximate dynamic programming for realtime control and neural modelling," *Handbook of intelligent control: neural, fuzzy and adaptive approaches*, pp. 493–525, 1992.

[197] F.-Y. Wang, H. Zhang, and D. Liu, "Adaptive dynamic programming: An introduction," *IEEE computational intelligence magazine*, vol. 4, no. 2, pp. 39–47, 2009.

[198] A. Al-Tamimi, F. L. Lewis, and M. Abu-Khalaf, "Discrete-time nonlinear HJB solution using approximate dynamic programming: Convergence proof," *IEEE Transactions on Systems, Man, and Cybernetics,*, vol. 38, no. 4, pp. 943–949, 2008.

[199] F. L. Lewis and D. Liu, *Reinforcement learning and approximate dynamic programming for feedback control*, vol. 17. John Wiley & Sons, 2013.

[200] N. Ab Aza, A. Shahmansoorian, and M. Davoudi, "From inverse optimal control to inverse reinforcement learning: A historical review," *Annual Reviews in Control*, 2020.

[201] D. S. Naidu, "Pontryagin minimum principle," in *Optimal Control Systems*, pp. 249–291, CRC Press, 2018.

[202] R. Bellman, "Dynamic programming," *Science*, vol. 153, no. 3731, pp. 34–37, 1966.

[203] E. D. Sontag, "A lyapunov-like characterization of asymptotic controllability," *SIAM journal on control and optimization*, vol. 21, no. 3, pp. 462–471, 1983.

[204] Y. Yang and J. M. Lee, "Design of a control lyapunov function for stabilizing specified states," *IFAC Proceedings Volumes*, vol. 43, no. 5, pp. 529–534, 2010.

[205] B. D. Anderson and J. B. Moore, *Optimal control: linear quadratic methods.* Courier Corporation, 2007.

[206] R. A. Freeman and P. V. Kokotovic, "Optimal nonlinear controllers for feedback linearizable systems," in *Proceedings of 1995 American Control Conference-ACC'95*, vol. 4, pp. 2722–2726, IEEE, 1995.

[207] R. E. Kalman, "When is a linear control system optimal?," 1964.

[208] F. Ornelas, E. N. Sanchez, and A. G. Loukianov, "Discrete-time inverse optimal control for nonlinear systems trajectory tracking," in *49th IEEE Conference on Decision and Control (CDC)*, pp. 4813–4818, IEEE, 2010.

[209] T. L. Molloy, J. J. Ford, and T. Perez, "Online inverse optimal control on infinite horizons," in *2018 IEEE Conference on Decision and Control (CDC)*, pp. 1663–1668, IEEE, 2018.

[210] T. L. Molloy, J. J. Ford, and T. Perez, "Finite-horizon inverse optimal control for discrete-time nonlinear systems," *Automatica*, vol. 87, pp. 442–446, 2018.

[211] H. K. Khalil and J. W. Grizzle, *Nonlinear systems*, vol. 3. Prentice hall Upper Saddle River, NJ, 2002.

[212] F. Ornelas-Tellez, E. N. Sanchez, and A. G. Loukianov, "Inverse optimal control for discrete-time nonlinear systems via passivation," *Optimal Control Applications and Methods*, vol. 35, no. 1, pp. 110–126, 2014.

[213] M. Krstic, H. Deng, A. Fettweis, J. Massey, M. Thoma, E. Sontag, and B. Dickinson, *Stabilization of nonlinear uncertain systems.* Springer-Verlag, 1998.

[214] J. Casti, "On the general inverse problem of optimal control theory," *Journal of Optimization Theory and Applications*, vol. 32, no. 4, pp. 491–497, 1980.

[215] T. Yang, "Impulsive control," *IEEE Transactions on Automatic Control*, vol. 44, pp. 1081–1083, May 1999.

[216] X. Li, D. W. Ho, and J. Cao, "Finite-time stability and settling-time estimation of nonlinear impulsive systems," *Automatica*, vol. 99, pp. 361–368, 2019.

[217] Y. Wang and J. Lu, "Some recent results of analysis and control for impulsive systems," *Communications in Nonlinear Science and Numerical Simulation*, vol. 80, p. 104862, 2020.

[218] W. Du, S. Y. S. Leung, Y. Tang, and A. V. Vasilakos, "Differential evolution with event-triggered impulsive control," *IEEE transactions on cybernetics*, vol. 47, no. 1, pp. 244–257, 2016.

[219] H. Chang, C. H. Moog, A. Astolfi, and P. S. Rivadeneira, "A control systems analysis of hiv prevention model using impulsive input," *Biomedical Signal Processing and Control*, vol. 13, pp. 123–131, 2014.

[220] F. G. Hayden, J. J. Treanor, R. F. Betts, M. Lobo, J. D. Esinhart, and E. K. Hussey, "Safety and efficacy of the neuraminidase inhibitor GG167 in experimental human influenza," *Jama*, vol. 275, no. 4, pp. 295–299, 1996.

[221] G-Wellcome, "Zanamivir for inhalation, product information. Glaxo wellcome," 1999.

[222] V. S. Georgiev, K. Western, and J. J. McGowan, *National Institute of Allergy and Infectious Diseases, NIH: Volume 1: Frontiers in Research.* Springer Science & Business Media, 2008.

[223] F. G. Hayden, J. J. Treanor, R. S. Fritz, M. Lobo, R. F. Betts, M. Miller, N. Kinnersley, R. G. Mills, P. Ward, and S. E. Straus, "Use of the oral neuraminidase inhibitor oseltamivir in experimental human influenza: randomized controlled trials for prevention and treatment," *Jama*, vol. 282, no. 13, pp. 1240–1246, 1999.

[224] FDA, "Tamiflu (oseltamivir phosphate) capsules and for oral suspension," *Detailed view: safety labeling changes approved by FDA Center for Drug Evaluation and Research*, vol. vol. 2008, 2008.

[225] C. R. Rayner, P. Chanu, R. Gieschke, L. M. Boak, and E. N. Jonsson, "Population pharmacokinetics of oseltamivir when coadministered with probenecid," *The Journal of Clinical Pharmacology*, vol. 48, no. 8, pp. 935–947, 2008.

[226] M. A. Kamal, P. F. Smith, N. Chaiyakunapruk, D. B. Wu, C. Pratoomsoot, K. K. Lee, H. Y. Chong, R. E. Nelson, K. Nieforth, G. Dall, *et al.*, "Interdisciplinary pharmacometrics linking oseltamivir pharmacology, influenza epidemiology and health economics to inform antiviral use in pandemics," *British journal of clinical pharmacology*, vol. 83, no. 7, pp. 1580–1594, 2017.

[227] L. Canini, J. M. Conway, A. S. Perelson, and F. Carrat, "Impact of different oseltamivir regimens on treating influenza A virus infection and resistance emergence: insights from a modelling study," *PLoS Comput Biol*, vol. 10, no. 4, 2014.

[228] Y. Wattanagoon, K. Stepniewska, N. Lindegårdh, S. Pukrittayakamee, U. Silachamroon, W. Piyaphanee, T. Singtoroj, W. Hanpithakpong, G. Davies, J. Tarning, *et al.*, "Pharmacokinetics of high-dose oseltamivir in healthy volunteers," *Antimicrobial agents and chemotherapy*, vol. 53, no. 3, pp. 945–952, 2009.

[229] F. L. Lewis, D. Vrabie, and V. L. Syrmos, *Optimal control*. John Wiley & Sons, 2012.

[230] W. M. Haddad, J. Fausz, V. Chellaboina, and C. Abdallah, "Optimal discrete-time control for nonlinear cascade systems," in *Proceedings of the American Control Conference.*, vol. 3, pp. 2175–2176, IEEE, 1997.

[231] E. N. Sanchez and F. Ornelas-Tellez, *Discrete-time inverse optimal control for nonlinear systems*. CRC Press, 2013.

[232] R. Ortega, J. A. L. Perez, P. J. Nicklasson, and H. J. Sira-Ramirez, *Passivity-based control of Euler-Lagrange systems: mechanical, electrical and electromechanical applications*. Springer Science & Business Media, 2013.

[233] J. P. LaSalle, *The stability and control of discrete processes*, vol. 62. Springer Science & Business Media, 2012.

[234] G. L. Amicucci, S. Monaco, and D. Normand-Cyrot, "Control lyapunov stabilization of affine discrete-time systems," in *Proceedings of the 36th IEEE Conference on Decision and Control*, vol. 1, pp. 923–924, IEEE, 1997.

[235] B. Brogliato, R. Lozano, B. Maschke, and O. Egeland, "Dissipative systems analysis and control," *Theory and Applications*, vol. 2, 2007.

[236] R. A. Freeman and J. A. Primbs, "Control lyapunov functions: New ideas from an old source," in *Proceedings of 35th IEEE Conference on Decision and Control*, vol. 4, pp. 3926–3931, IEEE, 1996.

[237] WHO, "Guidelines for pharmacological management of pandemic influenza A(H1N1) 2009 and other influenza viruses," *World Health Organization*, vol. vol. 20090820, 2009.

[238] A. Y. Alanis, M. Hernandez-Gonzalez, and E. A. Hernandez-Vargas, "Observers for biological systems," *Applied Soft Computing*, vol. 24, pp. 1175–1182, 2014.

[239] G. Hernandez-Mejia, E. A. Hernandez-Vargas, A. Y. Alanis, and N. Arana-Daniel, "Recurrent high order neural networks identification for infectious diseases," in *2018 International Joint Conference on Neural Networks (IJCNN)*, pp. 1–7, IEEE, 2018.

[240] R. Zurakowski, "Nonlinear observer output-feedback MPC treatment scheduling for HIV," *Biomedical engineering online*, vol. 10, no. 1, p. 40, 2011.

[241] P. H. Chang, J. W. Lee, and S. H. Park, "Time delay observer: A robust observer for nonlinear plants," 1997.

[242] W. Wen, C. Chen, J. Tang, C. Wang, M. Zhou, Y. Cheng, X. Zhou, Q. Wu, X. Zhang, Z. Feng, *et al.*, "Efficacy and safety of three new oral antiviral treatment (molnupiravir, fluvoxamine and paxlovid) for COVID-19:- a meta-analysis," *Annals of medicine*, vol. 54, no. 1, pp. 516–523, 2022.

[243] P. Mathur and S. Kottilil, "Immunomodulatory therapies for COVID-19," *Frontiers in Medicine*, vol. 9, p. 921452, 2022.

[244] R. S. Wallis, A. O'Garra, A. Sher, and A. Wack, "Host-directed immunotherapy of viral and bacterial infections: past, present and future," *Nature Reviews Immunology*, pp. 1–13, 2022.

[245] L. Lennart, "System identification: theory for the user," *PTR Prentice Hall, Upper Saddle River, NJ*, vol. 28, 1999.

[246] S. N. Kumpati, P. Kannan, *et al.*, "Identification and control of dynamical systems using neural networks," *IEEE Transactions on neural networks*, vol. 1, no. 1, pp. 4–27, 1990.

[247] V. S. Chakravarthy, N. Gupte, S. Yogesh, and A. Salhotra, "Chaotic synchronization using a network of neural oscillators," *International journal of neural systems, World Scientific.*, vol. 18, no. 02, pp. 157–164, 2008.

[248] W. Yu, "Nonlinear system identification using discrete-time recurrent neural networks with stable learning algorithms," *Information sciences, Elsevier.*, vol. 158, pp. 131–147, 2004.

[249] J. D. Rios, A. Y. Alanis, J. Rivera, and M. Hernandez-Gonzalez, "Real-time discrete neural identifier for a linear induction motor using a dspace DS1104 board," in *The 2013 International Joint Conference on Neural Networks (IJCNN).*, pp. 1–6, IEEE, 2013.

[250] J. D. Rios, A. Y. Alanis, M. Lopez-Franco, C. Lopez-Franco, and N. Arana-Daniel, "Real-time neural identification and inverse optimal control for a tracked robot," *Advances in Mechanical Engineering,*, vol. 9, no. 3, p. 1, 2017.

[251] J. Liang, Z. Wang, and X. Liu, "Global synchronization in an array of discrete-time neural networks with nonlinear coupling and time-varying delays," *International Journal of Neural Systems,*, vol. 19, no. 01, pp. 57–63, 2009.

[252] H. B. Demuth, M. H. Beale, O. De Jess, and M. T. Hagan, *Neural network design.* Martin Hagan, 2014.

[253] Y. Song and J. W. Grizzle, "The extended kalman filter as a local asymptotic observer for nonlinear discrete-time systems," in *American Control Conference*, pp. 3365–3369, IEEE, 1992.

[254] T. Başar and G. J. Olsder, *Dynamic noncooperative game theory.* SIAM, 1998.

[255] H. M. Dobrovolny, M. B. Reddy, M. A. Kamal, C. R. Rayner, and C. A. Beauchemin, "Assessing mathematical models of influenza infections using features of the immune response," *PloS one*, vol. 8, no. 2, p. e57088, 2013.

[256] P. C. Doherty, S. J. Turner, R. G. Webby, and P. G. Thomas, "Influenza and the challenge for immunology," *Nature immunology*, vol. 7, no. 5, pp. 449–455, 2006.

[257] H. Miao, J. A. Hollenbaugh, M. S. Zand, J. Holden-Wiltse, T. R. Mosmann, A. S. Perelson, H. Wu, and D. J. Topham, "Quantifying the early immune response and adaptive immune response kinetics in mice infected with influenza A virus," *Journal of virology*, vol. 84, no. 13, pp. 6687–6698, 2010.

[258] A. Handel and R. Antia, "A simple mathematical model helps to explain the immunodominance of cd8 t cells in influenza a virus infections," *Journal of virology*, vol. 82, no. 16, pp. 7768–7772, 2008.

[259] A. Boianelli, N. Sharma-Chawla, D. Bruder, and E. A. Hernandez-Vargas, "Oseltamivir PK/PD modelling and simulation to evaluate treatment strategies against influenza-pneumococcus coinfection," *Frontiers in Cellular and Infection Microbiology*, vol. 6, p. 60, 2016.

[260] N. F. Ramirez, D. Ríos-Rivera, E. A. Hernandez-Vargas, and A. Y. Alanis, "Inverse optimal impulsive neural control for complex networks applied to epidemic diseases," *Systems*, vol. 10, no. 6, p. 204, 2022.

[261] M. Hernandez-Gonzalez, M. V. Basin, and E. A. Hernández-Vargas, "Discrete-time high-order neural network identifier trained with high-order sliding mode observer and unscented kalman filter," *Neurocomputing*, vol. 424, pp. 172–178, 2021.

[262] B. F. Koel, R. Mögling, S. Chutinimitkul, P. L. Fraaij, D. F. Burke, S. van der Vliet, E. de Wit, T. M. Bestebroer, G. F. Rimmelzwaan, A. D. Osterhaus, *et al.*, "Identification of amino acid substitutions supporting antigenic change of influenza A (H1N1) pdm09 viruses," *Journal of virology*, vol. 89, no. 7, pp. 3763–3775, 2015.

[263] D. Liu and Q. Wei, "Finite-approximation-error-based optimal control approach for discrete-time nonlinear systems," *IEEE Transactions on Cybernetics*, vol. 43, no. 2, pp. 779–789, 2013.

[264] E. M. Navarro-López, “Local feedback passivation of nonlinear discrete-time systems through the speed-gradient algorithm,” *Automatica*, vol. 43, no. 7, pp. 1302–1306, 2007.

[265] Z. Wang, Q. Wei, and D. Liu, “A novel triggering condition of event-triggered control based on heuristic dynamic programming for discrete-time systems,” *Optimal Control Applications and Methods*, vol. 39, no. 4, pp. 1467–1478, 2018.

[266] E. A. Hernandez-Vargas and J. X. Velasco-Hernandez, “In-host mathematical modelling of COVID-19 in humans,” *Annual reviews in control*, 2020.

[267] A. Torneri, P. Libin, J. Vanderlocht, A.-M. Vandamme, J. Neyts, and N. Hens, “A prospect on the use of antiviral drugs to control local outbreaks of COVID-19,” *BMC medicine*, vol. 18, no. 1, pp. 1–9, 2020.

[268] K. M. White, R. Rosales, S. Yildiz, T. Kehrer, L. Miorin, E. Moreno, S. Jangra, M. B. Uccellini, R. Rathnasinghe, L. Coughlan, *et al.*, “Plitidepsin has potent preclinical efficacy against SARS-CoV-2 by targeting the host protein eEF1A,” *Science*, vol. 371, no. 6532, pp. 926–931, 2021.

[269] J. H. Beigel, K. M. Tomashek, L. E. Dodd, A. K. Mehta, B. S. Zingman, A. C. Kalil, E. Hohmann, H. Y. Chu, A. Luetkemeyer, S. Kline, D. Lopez de Castilla, R. W. Finberg, K. Dierberg, V. Tapson, *et al.*, “Remdesivir for the treatment of COVID-19 — final report,” *New England Journal of Medicine*, vol. 383, no. 19, pp. 1813–1826, 2020.

[270] Y. Lou, L. Liu, H. Yao, X. Hu, J. Su, K. Xu, R. Luo, X. Yang, L. He, X. Lu, *et al.*, “Clinical outcomes and plasma concentrations of baloxavir marboxil and favipiravir in COVID-19 patients: an exploratory randomized, controlled trial,” *European Journal of Pharmaceutical Sciences*, vol. 157, p. 105631, 2021.

[271] W. P. Painter, W. Holman, J. A. Bush, F. Almazedi, H. Malik, N. C. Eraut, M. J. Morin, L. J. Szewczyk, and G. R. Painter, “Human safety, tolerability, and pharmacokinetics of molnupiravir, a novel broad-spectrum oral antiviral agent with activity against sars-cov-2,” *Antimicrobial agents and chemotherapy*, vol. 65, no. 5, pp. e02428–20, 2021.

[272] P. Little, “Non-steroidal anti-inflammatory drugs and COVID-19,” 2020.

[273] W. Zhang, Y. Zhao, F. Zhang, Q. Wang, T. Li, Z. Liu, J. Wang, Y. Qin, X. Zhang, X. Yan, *et al.*, “The use of anti-inflammatory drugs in the treatment of people with severe coronavirus disease 2019 (COVID-19): The perspectives of clinical immunologists from china,” *Clinical Immunology*, vol. 214, p. 108393, 2020.

[274] S. S. Lakdawala and V. D. Menachery, “The search for a COVID-19 animal model,” *Science*, vol. 368, no. 6494, pp. 942–943, 2020.

[275] M. V. Blagosklonny, “From causes of aging to death from COVID-19,” *Aging (Albany NY)*, vol. 12, no. 11, p. 10004, 2020.

[276] L. Fang, G. Karakiulakis, and M. Roth, “Are patients with hypertension and diabetes mellitus at increased risk for COVID-19 infection?,” *The Lancet. Respiratory Medicine*, vol. 8, no. 4, p. e21, 2020.

[277] W. M. Haddad, V.-S. Chellaboina, J. L. Fausz, and C. Abdallah, “Optimal discrete-time control for non-linear cascade systems,” *Journal of The Franklin Institute*, vol. 335, no. 5, pp. 827–839, 1998.

[278] T. Ohsawa, A. M. Bloch, and M. Leok, “Discrete Hamilton-Jacobi theory and discrete optimal control,” in *The 49th IEEE Conference on Decision and Control (CDC),*, pp. 5438–5443, IEEE, 2010.